Heidelberg University

High Resolution Magnetic Micro-calorimeters: Thermodynamics, Cooling Requirements, and Noise

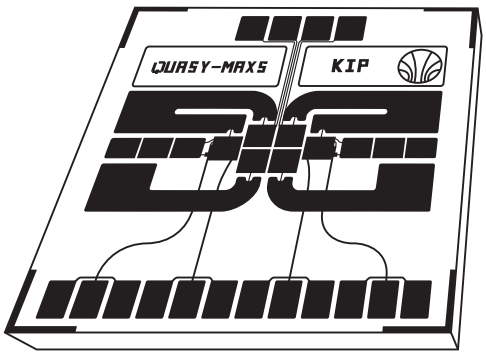

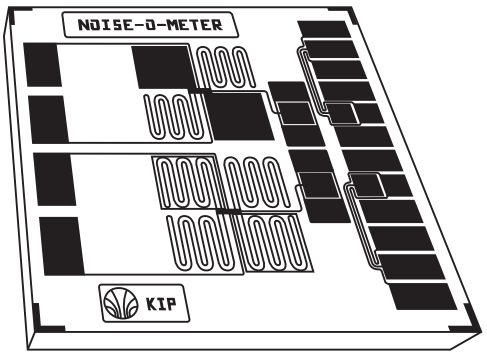

Matthew Herbst

Dissertation

2023

Dissertation

submitted to the

Combined Faculty of Mathematics, Engineering and Natural Sciences

of Heidelberg University, Germany

for the degree of

Doctor of Natural Sciences

Put forward by

Matthew Alexander Herbst

born in Heidelberg, Germany

Oral examination: 18 July 2023

High Resolution Magnetic Micro-calorimeters: Thermodynamics, Cooling Requirements, and Noise

Referees: Prof. Dr. Christian Enss
Prof. Dr. Maurits Haverkort

Magnetic micro-calorimeters (MMCs) are cryogenic particle detectors well suited for high-precision X-ray spectroscopy. They measure the temperature rise caused by an X-ray impact via the change in magnetization of a paramagnetic temperature sensor. Until now, MMCs have been designed to operate at around 20 mK, requiring sophisticated cooling, which limits their application. In this work, we show that magnetic micro-calorimetry is possible at significantly higher temperatures, by developing two novel MMCs with reduced cooling requirements. The first illustrates a new application for MMCs in the field of particle induced X-ray emission spectroscopy. At an operating temperature of 85 mK, this detector has a FWHM energy resolution of 19 eV at 5.9 keV, outperforming current alternatives. Our second MMC is a proof-of-principle detector, which demonstrates that operating temperatures of up to 300 mK are feasible. With a third, stand-alone device, we analyze noise sources affecting superconducting microstructures, such as MMCs. By comparing results from three different operation modes, we are able to disentangle noise components, in particular magnetic flux noise. High-precision measurements of noise originating from the sensor show a previously unobserved Johnson noise component and unexpected variations in the magnetic flux noise, which we relate to the dynamics of the magnetic moments in the sensor. Overall, our results broaden the application range of MMCs, and illustrate how noise analysis can improve the performance of superconducting devices.

Hochauflösende Magnetische Mikrokalorimeter: Thermodynamik, Kühlung und Rauschen

Magnetische Mikrokalorimeter (MMCs) sind kryogene Teilchendetektoren, die sich für hochauflösende Röntgenspektroskopie eignen. MMCs messen den durch einen Röntgeneinschlag verursachten Temperaturanstieg über die Änderung der Magnetisierung eines paramagnetischen Sensors. Bislang wurden MMCs für einen Betrieb bei etwa 20 mK ausgelegt, was eine aufwendige Kühlung erfordert und ihren Anwendungsbereich einschränkt. Im Rahmen dieser Arbeit wird gezeigt, dass MMCs auch bei deutlich höheren Temperaturen betrieben werden können, indem zwei neuartige MMCs mit geringeren Kühlanforderungen entwickelt wurden. Der erste Detektor etabliert eine für MMCs neue Anwendung auf dem Gebiet der partikel-induzierten Röntgenemissionsspektroskopie. Bei einer Betriebstemperatur von 85 mK wurde eine Energieauflösung von 19 eV bei 5,9 keV beobachtet, was derzeitigen Alternativen übertrifft. Der zweiter MMC ist ein Proof-of-Principle-Detektor, der Betriebstemperaturen von bis zu 300 mK ermöglicht. Mit einem dritten, eigenständigen Gerät wurden Rauschquellen analysiert, die supraleitende Mikrostrukturen wie MMCs beeinflussen. Durch den Vergleich der Ergebnisse von drei verschiedenen Betriebsarten können Rauschkomponenten, insbesondere das magnetische Flussrauschen, identifiziert werden. Hochpräzise Messungen des vom Sensor ausgehenden Rauschens zeigen eine bisher nicht beobachtete Johnson-Rauschkomponente und unerwartete Variationen im magnetisch Flussrauschen, die mit der Dynamik der magnetischen Momente im Sensor in Verbindung gebracht werden können. Insgesamt erweitern die Ergebnisse den Anwendungsbereich von MMCs und veranschaulichen, wie eine Analyse des Rauschens die Qualität von supraleitenden Bauteilen verbessern kann.

Contents

1. Introduction

When Wilhelm Conrad Röntgen discovered a new type of radiation in 1895, he chose the name *X-ray* to indicate something mysterious and unknown. The name may have been poorly chosen, since his *New Kind of Ray* [Rön96] immediately unraveled mysteries and triggered a fountain of knowledge in the form of the scientific revolution around the change of the century. In a span of ten years following Röntgen's first experiments, the world witnessed the discovery of radioactivity [Bec96], the electron [Tho97], mass-energy equivalence [Ein05], and ultimately the birth of quantum mechanics. To this day, X-rays provide scientists with opportunities to explore new physics, due to them being prevalent in a plethora of processes, such as electron capture, photoionization, Compton scattering, or Bremsstrahlung. Indeed, many current experiments rely on the detection and spectroscopy of X-rays, and it follows that X-ray detectors are a central component in fundamental research.

The choice of detector type for each application is an important one. Early on, semiconductor detectors based on silicon or germanium operating at liquid nitrogen temperatures were the prime technology for the digital imaging of X-rays [Aki07, Sar94]. These devices can span a broad range of detectable energies, but typically only reach energy resolutions of around 150 eV at 5.9 keV [Tho01]. An alternative are crystal spectrometers, which employ Bragg diffraction [Bra13] to reach energy resolving powers beyond 10 000 at the same energies [Kub14], and above 10^5 at higher energies. However, these wavelength-dispersive detectors can only perform measurements in a small wavelength range. Combining the best of both worlds are cryogenic micro-calorimeters operated at millikelvin temperatures [Ens05b]. These devices sense the temperature increase from an X-ray absorbed in a piece of matter and are thus not limited to a narrow energy window. At the same time, due to the low thermal noise and low specific heat at such temperatures, energy resolutions in the eV range are possible [Smi12]. First suggested almost a century ago [Sim35], modern systems come in multiple different variants including semiconductor thermistors [McC05a], transition edge sensors [Ull15], and magnetic micro-calorimeters [Fle05].

Of these, our focus lies on the latter: The magnetic micro-calorimeter, also called metallic magnetic calorimeter (MMC), reads out the temperature change from a particle impact via a paramagnetic sensor material, which sits in a weak magnetic field. This sensor material is either gold or silver doped with a small amount of erbium [Ban93], making the alloy strongly paramagnetic. According to Curie's law, a temperature change causes a change in the magnetization, which we then measure to deduce the energy of the impacting particle. MMCs can have an excellent energy

resolution of under 1.6 eV at 5.9 keV [Kem18], a fast response time of under 100 ns [Ran14], and only a small, well-understood, and smooth non-linearity [Gei20]. This makes them a prime candidate for high resolution X-ray spectroscopy.

Being cryogenic micro-calorimeters, MMC have been operated, so far, at temperature of around 20 mK. In order to reach these temperatures, various different cooling techniques are used. The most obvious of these is cooling by expanding gas. Pumping on ^{3}He, for instance, can yield temperatures of around 300 mK [Ens05a]. Also commonly used are so-called pulse tube coolers, which use expanding ^{4}He to reach temperatures of around 2.5 K in commercially available systems and 1.2 K in research prototypes. They are typically implemented as first stages in cryostats for even lower temperatures. As a second stage, one might use a dilution refrigerator, in which the mixing of a ^{3}He-rich and a ^{4}He-rich phase has a cooling effect. Commercial dilution refrigerators reach temperatures below 10 mK and are a typical tool to cool MMCs, since they allow for continuous, low temperatures [Blu22]. They are, however, relatively complex, large, and immobile, due to the requirement of handling the helium gas mixture. The alternative to dilution refrigerators are adiabatic demagnetization refrigerators (ADR), specifically electron spin demagnitizers, in which the cooling occurs via the demagnetization of a paramagnetic material. These cryostats typically do not reach as low temperatures and have a finite cycle time. However, due to the fact that ADRs do not require a ^{3}He/^{4}He mixture, they can be more compact, mobile, and cheaper. There are commercial two-stage ADR, which can keep a temperature of 100 mK for 200 hours and which are mounted on wheels [For23]. For similar temperatures, ADRs can also be designed with quasi-continuous cooling, and are ideally suited for satellites [Duv20].

We find that increasing the operating temperature of an MMC would greatly expand the possible application range. Two natural temperature ranges present themselves: First, an MMC operating near 100 mK would be able to be housed in a wide variety of compact ADRs. Second, an operating temperature of 300 mK would allow us to forgo the second stage entirely, and only rely on pumping ^{3}He. Applications may be found as a compact, permanent X-ray detector in the context of a larger experiment, such as in particle induced X-ray spectroscopy [Joh70, Joh76] or space missions [Ban19]. Alternatively, the MMC might be operated in a mobile cryostat outside of high precision physics experiments. For example, this would allow for the on-site characterization of the isotope ratio of nuclear fuel or for applications regarding aspects of home-land security, such as nuclear non-proliferation. Enabling magnetic micro-calorimetry with reduced cooling requirements is one main goal of this thesis.

A number of challenges appear when considering raising the operating temperature of an MMC by an order of magnitude. This refers to the thermodynamics of the detector. Specifically, the heat capacity C of components scales with $C \propto T$ to $C \propto T^3$, meaning that a particle with energy E impacting our detector produces far less temperature change $\Delta T = E/C$. Also, the thermal conductivity of components increases, requiring the redesign of various thermal links. Most important, however, is that the temperature dependence of the magnetization of the paramagnetic sensor material is significantly lower at higher temperatures, giving us less magnetization change per temperature change. Understanding these aspects, and accurately simulating the thermodynamics of magnetic micro-calorimeters is a second main goal.

One consequence of adapting current MMC technology to higher temperatures is the usage of a sensor material with a significantly higher concentration of erbium. This gives us the chance to revisit a curious phenomenon that was observed in the noise spectra created by the very first micro-structured MMCs in the early 2000s: There seemed to be a largely temperature independent noise component, which decreased reciprocally with the frequency and correlated with the amount of erbium in the device [Fle03, Dan05]. This so-called erbium noise has since been observed in other MMCs [Pie12] but is still not fully understood, with direct measurements not yielding conclusive results [Hof12, Wis13]. In a high temperature MMC, we expect erbium noise to play an important factor. For this reason, the third main goal of this thesis is an investigation of noise sources.

As it often happens with research projects, this final point turned into a slightly different direction. While erbium noise still is the focus, our experiments expanded into a general investigation of noise sources in superconducting microstructures. As we believe our results regarding these measurements merit the additional attention, we split this thesis into two parts, which cover topics referring to magnetic micro-calorimetry and to noise, respectively. We give an overview of the following chapters:

The first part begins with the essentials of operating a metallic magnetic calorimeter in chapter 2. We cover the basic working principle and go into detail regarding the magnetic nature of gold-erbium alloys, which is relevant throughout all following topics. There follows a brief explanation of read-out methods and calculations for estimating the performance of an MMC. We use this knowledge in chapter 3, in which we present a new software package designed to simulate the components of an MMC. This includes the thermodynamic properties of the paramagnetic sensor material, the magnetic field within it, and the response upon a particle hit. Combining these simulations allows us to simulate an entire MMC, calculate its energy resolution, and optimize various components. We are thus able to develop a new MMC for an application at uncommonly high temperatures: The detector Quasy-maXs is designed to operate at 85 mK in a small pulse-tube cryostat with an ADR stage,

where it acts as a detector for particle induced X-ray emission spectroscopy. In chapter 4, we present the new chip, characterization measurements, and discuss the possibility of Quasy-maXs replacing current detection methods in this field. Of a completely different nature is the second new MMC we developed, called Hot-maXs. The aim of this device is to explore the limits of magnetic micro-calorimetry in terms of cooling requirements, by constructing a detector that can detect particles at up to 300 mK. In chapter 5, we explain the necessary design choices and experimental methods, followed by first measurements.

In part two of this thesis, we broaden our horizon to superconducting devices in general. Our focus lies on the noise present in such devices, which requires a short introduction and overview in chapter 6. The core of this part, however, is a new noise measurement device, called the noise-o-meter. As we explain in chapter 7, we are able to disentangle the overall noise and identify individual noise components. With this powerful tool, we analyze a wide variety of noise sources ranging from Johnson noise to noise of the magnetization of interacting magnetic moments, as present in the Au:Er and Ag:Er temperature sensors of MMCs. Towards the end of the chapter, we demonstrate how noise measurements give us an insight into the microscopic nature of materials and how the noise-o-meter's capabilities open the doors to a wide range of future applications. We end with a summary and conclusion.

Part I

Magnetic Micro-calorimetry

2. Basics of Metallic Magnetic Calorimeters

Metallic Magnetic Calorimeters (MMCs) are cryogenic micro-calorimeters, designed to act as particle detectors. First proposed in the early 90s [Ban93], the field of MMCs has since produced a wide variety of experiments [Gas17, Rei20, Sik20, Dev22], and extensive reviews are available in literature [Ens00, Fle05, Fle09a, Kem18]. We focus here, however, only on the most relevant aspects for our applications. Specifically, we discuss the basics of MMCs acting as X-ray detectors, as well as details we require for simulating MMCs and for designing high operating temperature MMCs.

The basic working principle of an MMC is sketched out in figure 2.1. An X-ray photon with energy δE impacts an absorber with heat capacity C_a, heating it up. The precise process of the thermalization of the absorber is dependent on the absorber material, and we discuss details in section 2.1. In close thermal contact lies a sensor material with heat capacity C_s. In our MMCs, this is a strongly paramagnetic Au:Er alloy, whose temperature dependent magnetization $M(T)$ translates the temperature increase upon photon impact into a change in magnetization

$$\delta M \cong \frac{\partial M(T)}{\partial T}\,\delta T \cong \frac{\partial M}{\partial T}\frac{\delta E}{C_\mathrm{a}+C_\mathrm{s}} \quad . \tag{2.1}$$

An in-depth understanding of the thermodynamic and magnetic properties of Au:Er is essential throughout this thesis, and we cover this topic in section 2.2. In close proximity to the sensor is a superconducting pick-up coil, which is connected to the input coil of a current-sensing SQUID (Superconducting QUantum Interference Device), forming a closed superconducting circuit. The pick-up coil allows us to detect any changes in flux $\delta\Phi \propto \delta M$ by the induced screening current $\delta I \propto \delta\Phi$. The

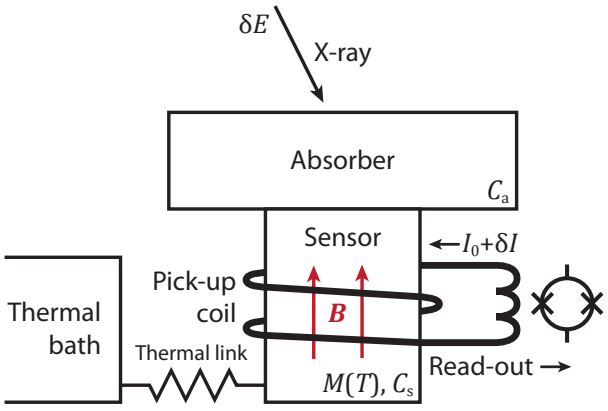

Figure 2.1: Schematic of an MMC. An X-ray photon impacts the absorber, which is thermally well coupled to a paramagnetic temperature sensor. The resulting temperature increase leads to a change in magnetization of the latter, which is read out via a pick-up coil. The MMC then thermalizes with a thermal bath.

precise relation between these quantities, as well as the geometry of the pick-up coil, are the focus of section 2.3. The following section 2.4 covers the process of injecting a persistent current I_0 into the superconducting pick-up circuit. This current provides the magnetic field[1] $\boldsymbol{B}$ within the sensor volume that is necessary to create a finite sensor magnetization. In section 2.5, we then discuss the low temperature current sensor as well as the latter parts of the read-out chain. These translate the current in the pick-up circuit, often called superconducting flux transformer, into a measurable voltage $\delta V \propto \delta I$ at room temperature. In order for the detector to be able to cool back down to its base temperature in a controlled manner, a weak thermal link leads to a thermal bath. This gives us a distinct pulse shape, which we cover in section 2.6. As a result, we can then conclude this chapter by estimating the energy resolution of an MMC in section 2.7.

2.1 Particle Absorber

While for the MMCs discussed here the absorber is to first order a simple cuboid of metal, its design is highly relevant. Important are three properties in particular. First is the thermalization behavior, a process known as energy down-conversions, in which the energy of an incident photon converts into a temperature increase of the absorber. The thermalization may influence the pulse shape and thus the energy resolution of the detector. Second is the heat capacity. As we mention above, the change in temperature δT is inversely proportional to $C_\mathrm{a} + C_\mathrm{s}$, meaning that a low absorber heat capacity increases the measured signal $\delta V \propto \delta T$. Third is the quantum efficiency, that is the percentage of photons that are absorbed, instead of passing through.

In chapters 4 and 5, we present two MMCs with two fundamentally different absorbers: a normal-conducting metallic absorber made of gold, and a superconducting absorber made of lead. In the following, we give an overview of these two absorber types and discuss them regarding the three properties mentioned above.

2.1.1 Normal-conducting Absorber Made of Gold

The process of energy down-conversion in metallic absorbers is well explored in literature [Koz00b, Mar06, Koz12]. In short, when an X-ray is absorbed in the absorber via the photo-effect, a bound electron of an atom is ejected. Within femtoseconds, the photoelectron loses its energy via electron-electron interactions, leading to further ionization and the emission of plasmons. The resulting electron-hole plasma further

[1] In general, we do not differentiate between the flux density B and the magnetic field H, and use B for both quantities. When relevant, we take care to distinguish the two.

thermalizes via electron-electron collisions, until the excitation is low enough for the cross-section of electron-phonon interactions to dominate. In this stage, phonons are rapidly created, forming an expanding phonon bubble. This disperses the energy further, until phonon re-absorption via electron-phonon interactions is on a similar time scale to phonon emission. At this point, energy shifts to the electron system and thermalization across the entire absorber occurs predominantly via thermal diffusion of electronic excitations, until thermal equilibrium is reached.

The time scale of this entire process lies well below 1 µs for a typical gold absorber and is dominated by the electronic thermal conductivity and the specific heat [Fle05]. However, this means that the signal shape may have an impact position dependence [Pie12], which we may mitigate by incorporating a thermal bottleneck between absorber and sensor. Also commonly implemented are so-called *stems* that minimize the contact area of absorber and sensor and thus reduce the loss of athermal phonons [Fle09a]. Overall, the thermalization in gold is a fast process well confined to the absorber. This is a main advantage of the normal-conducting metallic absorber. However, the conduction electrons add significantly to the overall specific heat

$$c_{\mathrm{Au}}(T) = c_{\mathrm{el}}(T) + c_{\mathrm{ph}}(T) = \gamma\, T + N_{\mathrm{A}} k_{\mathrm{B}} \frac{12\pi^4}{5} \left(\frac{T}{\Theta_{\mathrm{D}}}\right)^3 \quad , \tag{2.2}$$

outweighing the phononic contribution c_{ph} by a factor of $\frac{c_{\mathrm{el}}}{c_{\mathrm{ph}}} = 140$ for gold at $T = 100\,\mathrm{mK}$. In the equation above, $N_{\mathrm{A}} = 6.022 \times 10^{23}\,\mathrm{mol}^{-1}$ and $k_{\mathrm{B}} = 1.381 \times 10^{-23}\mathrm{J/K}$ are the Avogadro and Boltzmann constants, and the Debye temperature $\Theta_{\mathrm{D}} = 162\,\mathrm{K}$ and Sommerfeld coefficient $\gamma = 0.729\,\mathrm{mJ\,mol^{-1}K^{-2}}$ are material constants [Ste83, Kit05]. Finally, we should note that of all normal-conducting metals, gold is particularly well suited as an absorber: It is chemically stable, easy to microfabricate, and its large atomic number gives it a high stopping power.

2.1.2 Superconducting Absorber Made of Lead

Up until the creation of the phonon bubble, energy down-conversion in superconductors is identical to the process discussed above for normal-conducting metals. However, as phonon re-absorption takes over, excessive break-up of Cooper pairs sets in and energy shifts to a non-equilibrium distribution of quasiparticles. The following thermalization is not fully understood and subject to extensive research [Rot67, Kap76, Koz00a]. We summarize the most important points here and refer the reader to review papers for a detailed overview [Koz00b, Koz12].

The quasiparticle thermalization process can be divided into two parts: first, the relaxation with time constant τ_{s} of high energy quasiparticles into a constant number of quasiparticles at the energy gap Δ. Second, the recombination of said quasipar-

ticles into Cooper pairs with a time constant τ_0. A model [Kap76] assuming an infinitely large monocrystalline superconductor in thermal equilibrium approximates the former as

$$\frac{\tau_0}{\tau_\mathrm{s}}(\Delta, T) \approx \Gamma\left(\frac{7}{2}\right)\zeta\left(\frac{7}{2}\right)\sqrt{\frac{k_\mathrm{B}T}{2\Delta(T=0)}}\left(\frac{T}{T_\mathrm{c}}\right)^{\frac{7}{2}} \quad . \tag{2.3}$$

For lead, we insert a critical temperature $T_\mathrm{c} = 7.19\,\mathrm{K}$, a characteristic time constant $\tau_0 = 196\,\mathrm{ps}$ [Kap76], and an energy gap of $\Delta(T=0) = 2.15\,k_\mathrm{B}T_\mathrm{c}$ [Ens05a] to find $\tau_\mathrm{s} \approx 340\,\mu\mathrm{s}$ at 100 mK. For the recombination time, however, the model is not suited, since it only considers inelastic phonon processes. This would lead to τ_0 significantly exceeding the age of the universe, making it impossible for Cooper pairs to reform. Indeed, experimental evidence points towards a quasiparticle lifetime in the order of micro- or milliseconds [Gal91, Sta94, Nus00]. Reasons may be trapping sites, such as chemical impurities [Gol93] or Abrikosov vortices [Ull98], or enhanced disorder [Bar09]. Other experiments show a thermalization time approaching that of normal conductors for $T \geq 2 \times 10^{-4}\,\Theta_\mathrm{D}$ [Cos93, Wel08], which is fulfilled above 21 mK for lead with a Debye temperature of $\Theta_\mathrm{D} = 106\,\mathrm{K}$ [Ste83].

Overall, we expect the thermalization time of an absorber made of lead in our experiments to be at least in the order of τ_s, which can approach hundreds of microseconds, but is likely dominated by the quasiparticle lifetime τ_0. This is a clear disadvantage with respect to gold. However, since there is no electronic component to the specific heat in a superconductor well below T_c, c_Pb is significantly lower than c_Au. We refer to subsection 5.1.2 for a direct comparison of heat capacities. Regarding stopping power, lead and gold are similar on a per-atom basis, due to their similar atomic number. However, the particle density of gold is around 70 % higher, so a lead absorber with equivalent stopping power is thicker by that amount.

2.2 Sensor Material Au:Er

In an MMC, the sensor material converts the temperature change caused by a particle impact into a change in magnetization. We use dilute alloys of erbium in gold placed in a weak magnetic field of a few mT. For the detectors in this thesis, the erbium concentration is in the order of 2500 ppm, so that the magnetic moments of the erbium are quasi-free and provide the magnetic properties, while the gold acts as a dilutant to prevent magnetic ordering. The result is a strongly paramagnetic material, which has the desired temperature dependent magnetization. Detailed analyses of Au:Er are available in literature [Fle00, Fle05]. Here, we give a concise summary of the microscopic nature of Au:Er. A discussion of the thermodynamic properties, most notably the specific heat and magnetization, follows in section 3.2.

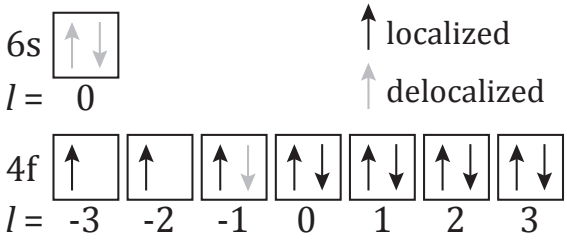

Figure 2.2: Schematic distribution of electrons in the 4f and 6s orbitals of Er^{3+}. Each arrow represents an electron with corresponding spin of $\pm 1/2$ and orbital angular momentum l. Grayed-out electrons are delocalized and contribute to the conduction band.

Non-interacting Magnetic Moments. In its pure form, gold forms a face centered cubic (fcc) lattice with a cubic lattice constant of 4.08 Å [Dav25]. When mixed with small amounts of erbium, a solid solution forms, where the fcc lattice is preserved and erbium replaces individual gold atoms [Rid65]. The erbium loses three electrons to the conduction band, leaving an Er^{3+} ion with an electron configuration of $[Xe]4f^{11}$. Using Hund's rules, we find the electron distribution appearing schematically in figure 2.2 with $L = 6$, $S = 3/2$, $J = L + S = 15/2$, and a Landé g-factor of $g_J = 6/5$ [Abr70]. All unpaired magnetic moments are confined to the 4f orbital, which has a radius of 0.3 Å [Fra76]. The larger 5s and 5p orbitals with a radius of around 1 Å partially shield the 4f electrons from crystal field effects from the surrounding gold and decrease coupling to conduction electrons. This is the main reason why alloys of noble metals and rare earth metals are well suited for MMCs: Sufficiently fast electron-spin relaxation of under 100 ns is still possible [Sjö75, Rot08], while, in particular for Er^{3+}, the de Gennes factor $(g_J - 1)^2 J(J + 1)$ [DG58], which is a measure for the interaction of the ion with the conduction electrons, is fairly small.

At temperatures below 100 K, the crystal field of the lattice splits the $J = 15/2$ ground state into five multiplets, of which in the mK range only the energetically lowest lying one, a Γ_7-doublet, is relevant [Wil69, Hah92]. We can thus approximate Er^{3+} as a two level system with effective spin $\tilde{S} = 1/2$ and an effective $\tilde{g}_J = 6.8$ [Tao71]. The doublet is split by the weak external magnetic field B according to the Zeeman Hamiltonian

$$\mathcal{H}_\mathrm{Z} = -\tilde{g}_J \mu_\mathrm{B} \tilde{S}_z B \quad , \tag{2.4}$$

where $\mu_\mathrm{B} = 9.274 \times 10^{-24}\,\mathrm{J/T}$ is the Bohr magneton.

Interacting Magnetic Moments. At millikelvin temperatures, and erbium concentrations above 10 ppm, interactions between erbium ions are no longer negligible. While we can ignore direct exchange due to the large distance between the erbium ions, we must consider two long-ranged interactions. These are the magnetic dipole-dipole interaction, which is present between any two magnetic dipoles, and the Ruderman–Kittel–Kasuya–Yosida (RKKY) interaction, which is an indirect interaction mediated via conduction electrons [Rud54, Kas56, Yos57]. We describe the former

via the dipole-dipole Hamiltonian

$$\mathcal{H}_{ij}^{\mathrm{dd}} = \Gamma_{\mathrm{dd}} \frac{1}{(2k_{\mathrm{F}}r_{ij})^3} \left[\boldsymbol{S}_i \cdot \boldsymbol{S}_j - 3\left(\boldsymbol{S}_i \cdot \hat{\boldsymbol{r}}_{ij}\right)\left(\boldsymbol{S}_j \cdot \hat{\boldsymbol{r}}_{ij}\right)\right] \quad , \tag{2.5}$$

which quantifies the interaction between two spin $\boldsymbol{S}_i$ and $\boldsymbol{S}_j$ at a distance r_{ij}. We see that the dipole-dipole interaction is dependent on the angle of the normalized distance vector $\hat{\boldsymbol{r}}_{ij}$ with respect to the spins. Here, the Fermi wave vector of gold, $k_{\mathrm{F}} = 1.2 \times 10^{10}\,\mathrm{m}^{-1}$ [Kit05], cancels out when inserting the dipole-dipole prefactor

$$\Gamma_{\mathrm{dd}} = \frac{\mu_0}{4\pi} \left(\tilde{g}\mu_{\mathrm{B}}\right)^2 \left(2k_{\mathrm{F}}\right)^3 \tag{2.6}$$

and we introduce it here only for easier comparison with the RKKY Hamiltonian

$$\mathcal{H}_{ij}^{\mathrm{RKKY}} = \Gamma_{\mathrm{RKKY}} \frac{1}{(2k_{\mathrm{F}}r_{ij})^3} \left(\boldsymbol{S}_i \cdot \boldsymbol{S}_j\right) \left[\cos\left(2k_{\mathrm{F}}r_{ij}\right) - \frac{1}{2k_{\mathrm{F}}r_{ij}} \sin\left(2k_{\mathrm{F}}r_{ij}\right)\right] \quad . \tag{2.7}$$

The term in square brackets describes the oscillating nature of the RKKY interaction, which can be either attractive or repulsive, depending on the distance between the magnetic moments. The RKKY prefactor

$$\Gamma_{\mathrm{RKKY}} = \mathfrak{J}^2 \frac{4V_0^2 m_{\mathrm{e}}^* k_{\mathrm{F}}^4}{\hbar^2 (2\pi)^3} \frac{\tilde{g}^2 (g_J - 1)^2}{g_J^2} \tag{2.8}$$

includes the effective mass m_{e}^* of the conduction electrons in gold, their coupling energy $\mathfrak{J}$ to the localized magnetic moments, and the volume V_0 of the primitive unit cell of the gold lattice. Since both Hamiltonians contain factors of r_{ij}^{-3} providing an envelope for their distance dependence, we consider only their relative strength

$$\alpha = \frac{\Gamma_{\mathrm{RKKY}}}{\Gamma_{\mathrm{dd}}} \quad . \tag{2.9}$$

For Au:Er, this dimensionless quantity is around $\alpha = 5$ [Fle03].

Nuclear Moments In erbium's natural isotopic composition, we find a single isotope with nuclear spin $I \neq 0$, which is ^{167}Er with $I = 7/2$ and a natural abundance of 22.9 %. The resulting hyperfine interaction causes a splitting of $\Delta E_F = 140\,\mathrm{mK} \cdot k_{\mathrm{B}}$ between the $F = 4$ and $F = 3$ multiplets at $B = 0$ [Sjö75]. Additionally, the multiplets split at $B \neq 0$ into a total of $9 + 7 = 16$ states with different z-components m_F. As we discuss in subsection 3.2.4, this has a detrimental effect on the thermodynamic properties.

The 100 % abundant ^{198}Au nuclei also have a nuclear spin, in this case $I = 3/2$. While the nuclear magnetic moment is negligible, the nuclear electric quadrupole moment

of 0.55 barn can cause hyperfine splitting, if the cubic fcc symmetry is broken and a non-cubic electric field gradient is present at the site of the nucleus. This may occur in close vicinity to erbium ions and results in additional energy levels [Her00]. In MMCs, a fast decay with a time constant of $\lesssim 1\,\mathrm{ms}$ has been traced to this effect [Ens00].

We conclude that while Au:Er is to first order an ensemble of spins in a lattice, a closer look reveals a complex magnetic system. Energy levels are not only dependent on the external magnetic field $\boldsymbol{B}$, but also on the relative distances and orientations of randomly distributed magnetic moments, as well as hyperfine effects. These details are important, since according to equation (2.1), we need precise quantitative knowledge of the heat capacity $C_\mathrm{s}(B,T)$ and magnetization $M(B,T)$ of the sensor, as we discuss in the next section. The numerical calculation of these quantities using simulations of the system presented here is the focus of section 3.2.

2.3 Sensor and Pick-up Coil Geometry

After covering how a particle impact leads to temperature increase of the detector and a subsequent magnetization change of the sensor, we now take a look at how we read out said change in magnetization. A number of different detector designs are possible and we once again refer the reader to more extensive literature [Fle05] for alternatives and a broader discussion on this topic. For the MMCs discussed here, however, we exclusively use a gradiometric set-up based on superconducting meander-shaped pick-up coils [Zin04]. This differs from the design in figure 2.1 in a number of aspects, as we explore in the following.

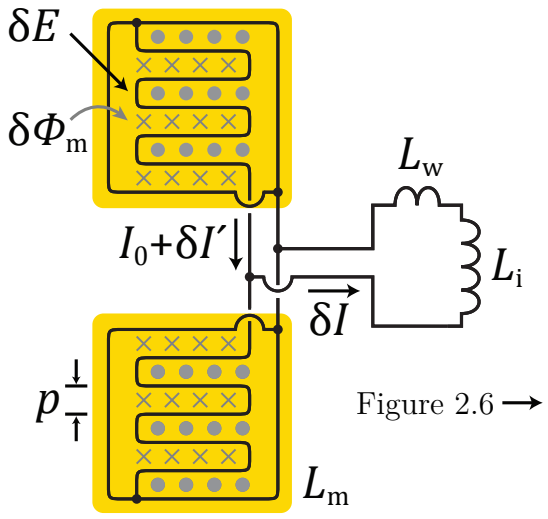

Figure 2.3: Schematic of a gradiometric pair of pick-up coils with inductance L_m covered by sensor material (transparent yellow). A persistent current I_0 creates an inhomogeneous magnetic field (gray). Further read-out occurs via an input coil with inductance L_i, which is inductively coupled to a dc-SQUID. The circuitry for the following steps appears in figure 2.6.

A schematic of the gradiometric sensor read-out appears in figure 2.3. This is a top view in which we omit absorbers for clarity and instead show two patches of paramagnetic sensor and the underlying meander-shaped pick-up coils with inductance L_m. The coils are identical, but mirrored, forming a gradiometer of first order. An input coil with inductance L_i is connected in parallel to both via lines with a stray inductance L_w. The three inductances form a completely superconducting network, where magnetic flux is conserved in each of the three superconducting loops. Via the input coil, the signal is coupled into a SQUID, over which further read-out occurs. We discuss that part in section 2.5 and in particular figure 2.6. For now, we calculate the current δI that flows through the input coil as the result of an energy input δE.

In good approximation, the inductance of a superconducting meander-shaped pick-up coil can be parameterized as

$$L_\mathrm{m} = l\,\mu_0 \frac{A}{p} \quad , \tag{2.10}$$

where $\mu_0 = 1.257 \times 10^{-6}\,\mathrm{H/m}$ is the magnetic permeability [Fle05]. This inductance depends on the covered area A and the pitch p of the meander, where the latter is the center-to-center distance of neighboring lines. Also relevant is the qualitative geometry of the meander, which, for thin-film meanders, can be described by the ratio between conductor width w and pitch. This is condensed in a constant $l(w/p)$ [Fle05]. In this thesis, we work with meander-shaped coils with $A = (120\,\mu\mathrm{m})^2$ to $(500\,\mu\mathrm{m})^2$, $p = 5\,\mu\mathrm{m}$ to $10\,\mu\mathrm{m}$, and $l(w/p) = 0.22$, giving us inductances in the nH range.

The two meander-shaped pick-up coils form a superconducting loop, and a persistent current I_0 in this loop creates a magnetic field within the sensor volume V that is highly inhomogeneous and thus dependent on the location $\boldsymbol{x}$. Finite element simulations of the magnetic field $\boldsymbol{B}(\boldsymbol{x})$ follow in section 3.1. Due to reciprocity, this magnetic field distribution also describes the location dependent coupling

$$G(\boldsymbol{x}/p) = \frac{p}{\mu_0} \frac{|\boldsymbol{B}(\boldsymbol{x})|}{I_0} \tag{2.11}$$

of the magnetic moment of an infinitesimally small volume element of the sensor $\mathrm{d}V$ at position $\boldsymbol{x}$ to the pick-up coil. In the definition above, we artificially introduce the pitch as a characteristic length scale, in order to make G dimensionless and dependent only on the qualitative geometry, that is w/p, and independent of the absolute values of the pitch p or line width w.

When a particle with energy δE impacts the absorber and the temperature increases, the magnetization $M(B(\boldsymbol{x}), T)$ changes by different amounts throughout the sensor.

Each element $\mathrm{d}V$ causes a change in magnetic flux

$$\mathrm{d}(\delta\Phi_\mathrm{m}) = \mu_0 \frac{G(\boldsymbol{x}/p)}{p} \delta M(B(\boldsymbol{x}), T)\,\mathrm{d}V \tag{2.12}$$

in the pick-up coil beneath. When integrating over the sensor volume and inserting equation (2.1), we obtain the overall change in flux

$$\delta\Phi_\mathrm{m} = \frac{\delta E}{C_\mathrm{a} + C_\mathrm{s}} \int_V \mu_0 \frac{G(\boldsymbol{x})}{p} \frac{\partial M(B(\boldsymbol{x}), T)}{\partial T}\,\mathrm{d}V \tag{2.13}$$

in the respective pick-up coil. Due to flux conservation in closed superconducting loops, this induces a screening current $\delta I'$, a portion δI of which flows through the input coil L_i. Using Kirchhoff's rules, we find

$$\delta I = \frac{\delta\Phi_\mathrm{m}}{L_\mathrm{m} + 2\,(L_\mathrm{i} + L_\mathrm{w})} \quad . \tag{2.14}$$

Due to the gradiometric design of the circuitry, particle impacts on the two sensors cause currents δI of opposite polarity. We can thus encode signals from two sensors within one read-out channel, since one sensor produces positive pulses and the other produces negative pulses. Additionally, a perfectly gradiometric detector is not sensitive to global temperature changes or homogeneous stray magnetic fields, as these cause exactly opposite currents to flow through the input coil, canceling out. Even magnetic fields with a gradient across the set-up have only a marginal influence, since the meander shape of the pick-up coils means that $G(\boldsymbol{x})$ is a multipole of high order. It also follows that cross-talk between coils is low, even if they are close. Finally, the planar coils and flat design of the sensor are compatible with micro-fabrication processes, which allow us to construct detectors reliably with thin film techniques.

2.4 Persistent Current Switch

In order to obtain a temperature-dependent magnetization of the sensor material, a magnetic field is necessary. In our MMCs, a persistent current flowing within the pick-up coils supplies this field. In figure 2.4, we have reduced the set-up to a pair of meander-shaped pick-up coils with inductances L_m, the input coil with inductance L_i, and a small superconducting persistent current switch (PCS) with inductance $L_\mathrm{h} \ll 2L_\mathrm{m}$. The process of injecting such a current consists of four steps:

1. Starting at a temperature well below the critical temperature of niobium, we supply a field current $I_\mathrm{f} \approx 100\,\mathrm{mA}$ via the so-called field lines, which flows almost exclusively via the low-inductance PCS.

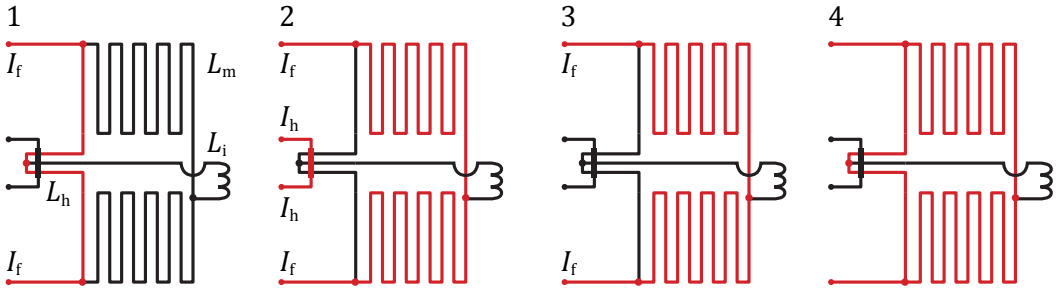

Figure 2.4: Four steps of injecting a persistent current into the two pick-up coils of a gradiometric set-up. Marked in red are lines through which significant current flows.

2. We apply a heater current $I_h \approx 3\,\mathrm{mA}$ through a $\sim 7\,\Omega$ switch heater, which breaks superconductivity of both the underlying niobium, which includes a section leading to the input coil. The current I_f now flows through the pick-up coils, since it is the only remaining superconducting path. There is no closed superconducting loop, and a flux $2L_m I_f$ is enclosed by the meanders.

3. After $t_h \approx 10\,\mu\mathrm{s}$, we switch off the heater current. As the PCS becomes superconducting, flux conservation in the meander circuit has to be fulfilled again.

4. We stop supplying I_f, and a persistent current

$$I_0 = \frac{2L_m}{2L_m + L_h} I_f = \frac{I_f}{1 + \frac{L_h}{2L_m}} \tag{2.15}$$

continues to flow in the meander circuit.

This process can be automated in software, and completes in milliseconds. Heating of the cryostat is kept to a minimum and the injection is reliable and reproducible [Her18].

2.5 Read-out Using SQUIDs

For all experiments we present in this thesis, the **S**uperconducting **QU**antum **I**nterference **D**evice (SQUID) is an essential part of the read-out chain. Since the topic of SQUIDs is a broad one, we focus here on only those aspects most pertinent to our applications, which include the dc-SQUIDs, two-stage SQUID read-out, and linearization. The reader may refer to textbooks [Cla04] for further information.

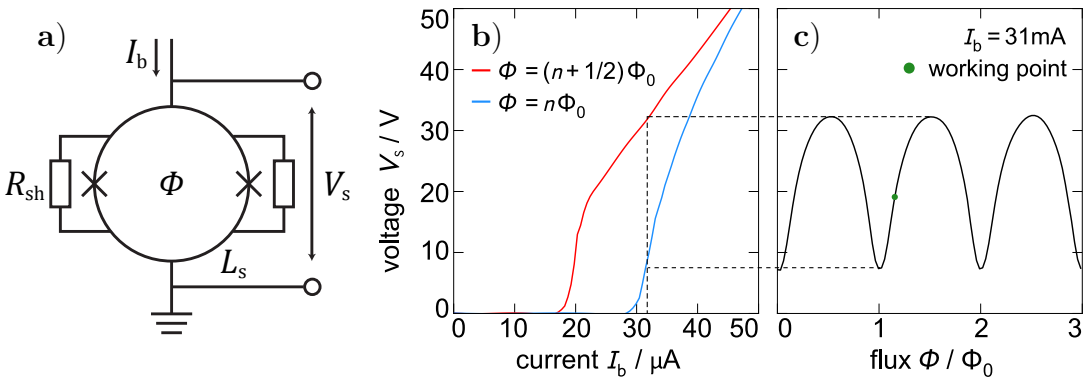

Figure 2.5: **a)** Diagram of a dc-SQUID. **b)** The I_b-V characteristic of a SQUID is dependent on Φ, where the two limiting cases appear in red and blue. **c)** The Φ-V characteristic of a SQUID, given a suitable I_b. Pictured data adapted from literature [Wei96].

2.5.1 dc-SQUIDs

At the core of a dc-SQUID lies a superconducting loop with inductance L_s, as depicted in figure 2.5 a). Two thin barriers of non-superconducting material, marked as crosses, intersect the loop. These so-called Josephson junctions are just a few nanometers thick, and each allows Cooper pairs to tunnel through, as long as a critical current I_c is not surpassed. Above this threshold, a part of the current is carried by quasiparticles across the barrier, and we observe a voltage drop V_s across the SQUID. Shunt resistors R_{sh} suppress hysteretic behavior between these two states. The critical current is dependent on the magnetic flux Φ through the SQUID in a periodic fashion, where the periodicity is given by the magnetic flux quantum $\Phi_0 = 2.07 \times 10^{-15}\,\mathrm{Tm}^2$. The two limiting cases of $\Phi = (n + 1/2)\,\Phi_0$ and $\Phi = n\,\Phi_0$, where $n \in \mathbb{Z}$, appear in figure 2.5 b).

When we operate the SQUID in *current bias*, we run a DC bias current I_b slightly above the maximal dissipation-free current through the SQUID and measure V_s. In this state, we find a periodic $V_s(\Phi)$ dependence as it appears in figure 2.5 c). At certain points in this curve, such as the working point marked in green, the output voltage is highly dependent on the magnetic flux Φ and the SQUID acts as a sensitive flux to voltage converter.

2.5.2 Two-stage Set-up

A schematic of the entire read-out chain appears in figure 2.6. The quantity we want to measure is the current δI produced by the experiment, which flows through the

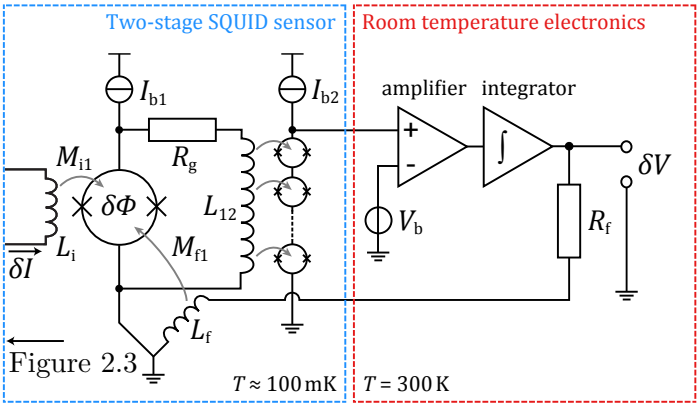

Figure 2.6: Schematic of read-out using a two-stage SQUID set-up, where we omit shunt resistors for clarity. Circuitry earlier in the read-out chain appears in figure 2.3. Image adapted from [Rei17a].

input coil with inductance L_i. The latter is coupled via the mutual inductance

$$M_\mathrm{i1} = \delta\Phi/\delta I \tag{2.16}$$

to the so-called *front-end SQUID*, producing a flux $\delta\Phi$ in the SQUID loop. The main difference to the previously discussed SQUID in figure 2.5 a) is that we operate the front-end SQUID in *voltage bias* by introducing a gain resistor with $R_\mathrm{g} \approx 300\,\mathrm{m\Omega}$ in parallel, which is about one order of magnitude smaller than the shunt resistors of the SQUID. In this configuration, a change in external flux leads to a change in current through the gain resistor and thus the input coil of the so-called *SQUID array*. In our case, the latter consists of 16 SQUIDs connected in series, resulting in a low-noise amplification stage, while keeping the power dissipation in the front-end SQUID, which is close to the potentially temperature sensitive experiment, to a minimum. We call this configuration a two-stage SQUID set-up. The SQUID array is operated in current bias, and thus translates the signal into a change in voltage, which we read out with room temperature equipment via a differential amplifier with bias voltage V_b.

Linearization

During the discussion of figure 2.5 b), we noted that a SQUID only acts as a sensitive flux-to-voltage converter in a small range of magnetic flux around a working point, that is where the Φ-V_s characteristic has a steep slope. In order to expand the linear flux range, we operate the two-stage SQUID set-up in *flux-locked loop* (FLL) mode. As the name suggests, the aim is to lock the flux in the front-end SQUID to a fixed value. To this end, we choose the reference voltage of the amplifier to be the voltage of the working point and feed the amplifier's output to an integrator. When moving off the working point, the integrator increases its output voltage. A feedback resistor with resistance R_f then lets a corresponding current flow through the feedback coil of the front-end SQUID, which is coupled to this SQUID with a mutual inductance M_f1.

This produces a corresponding flux, bringing the SQUID back to the working point. As a result, any change in flux in the front-end SQUID caused by a current in the input coil, which would cause the flux in the front-end SQUID to move away from the working point, is canceled out, and the flux stays constant. The resulting read-out voltage

$$\delta V = R_\mathrm{f} \frac{M_\mathrm{i1}}{M_\mathrm{f1}} \delta I \tag{2.17}$$

is proportional to the current we must send through the feedback coil in order to keep the front-end SQUID at this working point, and therefore proportional to the input current to be measured. This linear relation allows us to reliably read out signals across several Φ_0.

2.6 Pulse Shape

In the previous sections we have discussed the entire process from photon impact to voltage change at room temperature. Now, we take a look at the signal shape such an impact creates.

Consider an MMC with normal-conducting metallic absorber. To good approximation, it is described by the thermodynamic model in figure 2.7 consisting of two subsystems connected to a thermal bath with constant temperature T_0. These are the conduction electrons of sensor and absorber with heat capacity $C_\mathrm{el} = C_\mathrm{el,s} + C_\mathrm{el,a}$, where we assume that sensor and absorber are thermally well coupled, and the spin system with heat capacity C_z, consisting of the erbium ions. Thermal links with thermal conductances $G_\mathrm{el,b}$ and $G_\mathrm{z,el}$ connect C_el with the thermal bath, and C_z with C_el, respectively. We neglect components such as phononic heat capacity, or heat capacity from nuclear moments (see subsection 3.2.4). The heat input of an absorbed photon is in good approximation described by a heating power $P(t) = \delta E\, \delta(t)$. From this thermal model, we construct the system of coupled differential equations

$$\begin{aligned} \dot{E}_\mathrm{el} &= C_\mathrm{el}\dot{T}_\mathrm{el} = G_\mathrm{z,el}(T_\mathrm{z} - T_\mathrm{el}) + G_\mathrm{el,b}(T_0 - T_\mathrm{el}) + \delta E\, \delta(t) \\ \dot{E}_\mathrm{z} &= C_\mathrm{z}\dot{T}_\mathrm{z} \;\; = G_\mathrm{z,el}(T_\mathrm{el} - T_\mathrm{z}) \quad . \end{aligned} \tag{2.18}$$

The change in flux $\delta\Phi_\mathrm{m}$ in the pick-up coil is proportional to the energy content E_z

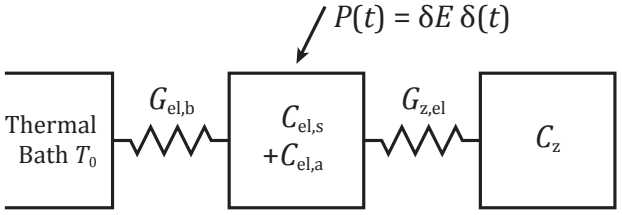

Figure 2.7: Thermodynamic model of an MMC.

of the spin system. We arbitrarily choose the offset $E_z(t \leq 0) = 0$ and solve the system above to obtain the responsivity

$$p(t > 0) = \frac{E_z(t > 0)}{\delta E} = \beta \left(-e^{-t/\tau_0} + e^{-t/\tau_1}\right) \quad , \tag{2.19}$$

which describes the detector response. Here, we introduced the fraction

$$\beta = \frac{C_z}{C_{el} + C_z} \tag{2.20}$$

of the contribution of the spin system to the overall heat capacity. The pulse shape is an exponential rise with a rise time τ_0, followed by an exponential decay with τ_1, with τ_0 and τ_1 depending on the heat capacities and thermal conductivities [Fle05].

A reasonable approximation is $G_{el,b} \ll G_{z,el}$ and C_{el} not too different from C_z, for which we find $\tau_1 = (C_{el} + C_z)/G_{el,b}$. The rise time τ_0 in our model is defined by $G_{z,el}$, which, on a microscopic level, is a measure for the interaction strength between conduction electrons and the 4f electrons of the erbium ions. Using the Korringa relation [Kor50], which gives a relation between the relaxation of magnetic moments and temperature, and measurements of the electron-paramagnetic resonance [VS81], we find typical time constants of under 100 ns [Ban93, Rot08]. This is only a lower limit, however, since in some detectors the approximation of a thermally well coupled absorber and sensor does not hold due to an engineered thermal bottleneck.

2.7 Energy Resolution

In order to estimate the energy resolution of an MMC, we require a measure for the noise affecting the detector. The topic of noise is a particular focus of this thesis, and we dedicate chapter 6 to an overview of possible noise sources. The reader may also refer to chapter 7 for measurements.

We can estimate the energy resolution of an MMC by comparing the detector response to the total noise in the frequency domain. For $\tau_0 \ll \tau_1$, the Fourier transform $\mathcal{F}\{\cdot\}$ of the responsivity from equation (2.19) is

$$|\mathcal{F}\{p\}(f)| = \beta \frac{\tau_0}{\sqrt{1 + (2\pi f \tau_0)^2}\sqrt{1 + (2\pi f \tau_1)^2}} \quad . \tag{2.21}$$

We thus find a frequency dependent signal-to-noise ratio of

$$\mathrm{SNR}(f) = \frac{|\mathcal{F}\{p\}(f)|}{\sqrt{S_z(f)}} \quad , \tag{2.22}$$

where $S_z(f)$ is the noise expressed as energy fluctuations in the spin system. From the signal-to-noise ratio, we calculate the energy resolution of the detector to be

$$\Delta E_{\mathrm{FWHM}} = 2\sqrt{2\ln 2} \cdot \left(\int_0^\infty 4\,\mathrm{SNR}^2(f)\,\mathrm{d}f \right)^{-1/2} \quad , \tag{2.23}$$

where the index refers to the full width half maximum [McC05b]. In order to estimate a possible fundamental limit of the energy resolution of an MMC, we assume the read-out, including SQUIDs, to be free of noise and arbitrarily fast. However, for the canonical ensemble in figure 2.7, the bath temperature T_0 is a fixed quantity, while the energy content of the spin and the electron system fluctuate around their mean values. The spin system exchanges heat quickly with the electrons and slowly with the bath, corresponding to the decay times. It has been shown [Fle01] that these thermodynamic fluctuations of energy of a canonical ensemble with two subsystems lead to a fundamental limit of the energy resolution of

$$\Delta E_{\mathrm{FWHM}} \approx 2\sqrt{2\ln 2}\,\sqrt{4k_{\mathrm{B}}C_{\mathrm{z}}T^2}\,\left(\frac{1}{\beta(1-\beta)}\right)^{1/4}\left(\frac{\tau_0}{\tau_1}\right)^{1/4} \quad , \tag{2.24}$$

where we assume $\tau_0 \ll \tau_1$. For $\beta = 1/2$, this expression minimizes and we obtain

$$\Delta E_{\mathrm{FWHM}} \approx 2\sqrt{2\ln 2}\,\sqrt{4k_{\mathrm{B}}C_{\mathrm{el}}T^2}\,\sqrt{2}\,\left(\frac{\tau_0}{\tau_1}\right)^{1/4} \quad . \tag{2.25}$$

Typical values for our MMCs are $C_{\mathrm{el}} = 10\,\mathrm{pJ/K}$, $T = 100\,\mathrm{mK}$, $\tau_0 = 1\,\mu\mathrm{s}$, and $\tau_1 = 1\,\mathrm{ms}$, which yields an energy resolution of $\Delta E_{\mathrm{FWHM}} = 8.7\,\mathrm{eV}$. Further optimizing the energy resolution requires minimizing the temperature, heat capacity, or rise time, or maximizing the decay time. However, these quantities are limited by the needs of the experiment or material properties. For our MMCs, for instance, the minimal temperature is given by the cryostat in which the detector is meant to operate. The heat capacity may be reduced by material choice, which has its own drawbacks (see subsection 2.1.2), or by reducing the absorber volume. However, the latter is limited by the required sensitive area and quantum efficiency. The rise time is defined at best by the Korringa relation we mentioned in section 2.6. Maximizing the decay time increases the dead time of the detector. As a result, the expression above demonstrates that there is a fundamental limit to the energy resolution of an MMC. Finally, we should reiterate that equation (2.25) is a best-case scenario, where we neglect most noise sources, interactions between magnetic moments, and a number of heat capacities. A more thorough simulation of the detector is the focus of the following chapter 3.

3. Simulating Metallic Magnetic Calorimeters

When developing a new experiment involving an MMC, the first step is to design a detector best suited for the given experiment-specific requirements and restrictions. An MMC has around 50 variable parameters, of which around half are given by outside restrictions and the other half can be actively chosen by the designer to find the best fitting detector. Examples are the dimensions of components, the selection of materials, and the choice of characteristic time constants. Simulations are an indispensable tool, which allow us to find optimal values.

First code for simulating the performance of an MMC was developed around 20 years ago [Sch00, Fle00, Fle05, Fle09a], and has been used for a wide range of MMCs [Bur08, Fle09b, Hen17]. In the framework of this thesis, we have developed a new set of simulation scripts, which are based on the existing algorithms, which were translated from various programming languages to python, merged, and extended to higher temperatures. While our code allows us to simulate the MMCs we discuss in chapters 4 and 5, we also aimed to make it as widely usable as possible and it has, indeed, already found a number of applications [Sch21, Man21, Bau22].

The process of simulating an MMC appears schematically in figure 3.1. Given a particular set of detector parameters, we perform three sets of simulations. The first is simulating the magnetic field distribution $\boldsymbol{B}(\boldsymbol{x})$ and using equation (2.11) to cal-

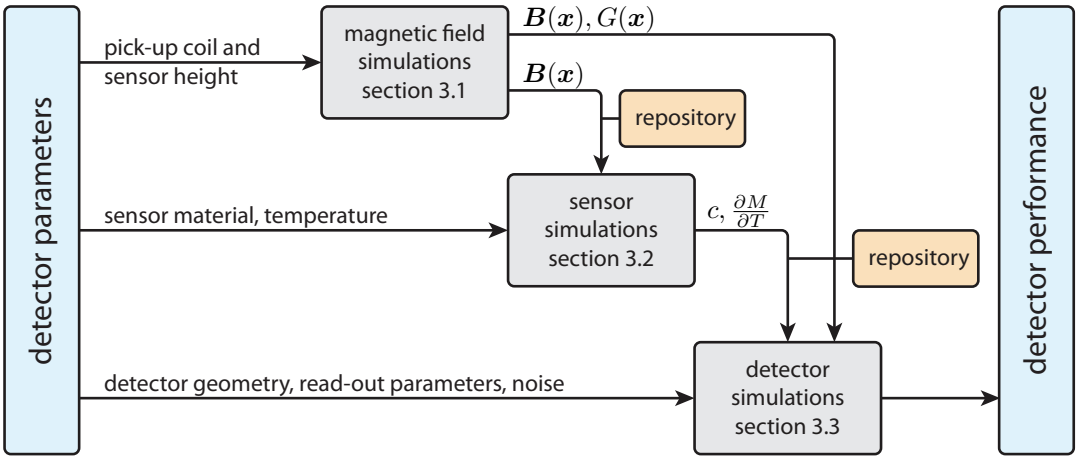

Figure 3.1: Flow diagram for simulating an MMC. Given a set of detector parameters, we simulate the detector performance. The process consists of three parts, which we discuss in the following sections.

culate the distribution of the geometry factor $G(\boldsymbol{x})$ within the sensor. We did not implement any major changes with respect to the original code, and thus cover it only briefly in section 3.1. Second are numeric calculations of the thermodynamic properties of the Ag:Er or Au:Er sensor material, specifically the specific heat $c(B,T)$ and slope $\frac{\partial M}{\partial T}(B,T)$ of the temperature-dependent magnetization. These we explain in some detail in section 3.2. Finally, we simulate the entire detector in section 3.3, which requires input from the previous two simulations. Our code calculates the detector performance based on the initial parameter set, and is also able to automatically optimize up to nine core parameters. At select points in this process, we construct repositories with intermediate results, which can act as starting points for new simulations and reduce duplicate calculations.

3.1 Magnetic Field Simulations

Due to the complex geometry of the meander-shaped pick-up coil, we cannot calculate the magnetic field $\boldsymbol{B}(\boldsymbol{x})$ in the sensor analytically. Instead, we perform finite element simulations using the software FEMM[1]. In figure 3.2 appears the cross-section of two lines of the meander coil, which carry currents of $I_0 = \pm 100\,\mathrm{mA}$. The simulation assumes periodic boundary conditions. Since a real pick-up coil consists of tens of coils, this is a good approximation of the magnetic field distribution in the entire sensor. In our example, the niobium lines have a pitch of $p = 10\,\mu\mathrm{m}$, a width of $w = 5\,\mu\mathrm{m}$, and a height of $h_{\mathrm{Nb}} = 250\,\mathrm{nm}$. The sensor layer has a height of $h_{\mathrm{sens}} = 2\,\mu\mathrm{m}$ and sits on top of a $h_{\mathrm{SiO_2}} = 350\,\mathrm{nm}$ thick layer of insulating SiO_2. We approximate both the sensor and the SiO_2 to have a magnetic susceptibility of $\chi = 0$. As a result of the simulations, we find that the magnetic field inside the sensor is highly inhomogeneous and ranges from 3 mT to 30 mT, with an average value of 8.8 mT. Using equation (2.11), we also calculate the geometry factor G and pass the results on to the sensor and detector simulations.

3.2 Simulation of the Thermodynamics of Au:Er and Ag:Er

There are two different approaches for simulating the thermodynamic properties of noble metals doped with erbium: First, the semi-classical mean field approximation, in which we reduce the system to an Ising model and each magnetic moment interacts with the mean molecular field caused by all others [Wal77, Wal80]. Second, the full quantum-mechanical approach, in which we construct a Hamiltonian based on the pairwise interaction of randomly distributed magnetic moments, and then diag-

[1] Finite Element Method Magnetics by David Meeker, http://www.femm.info.

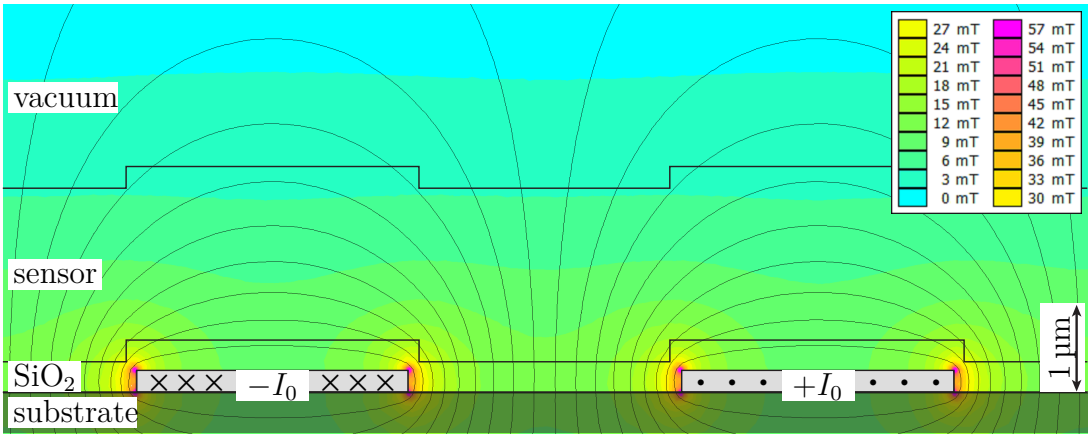

Figure 3.2: Cross-section of the simulated magnetic field distribution $\boldsymbol{B}(\boldsymbol{x})$ caused by a current of $I_0 = 100\,\mathrm{mA}$ flowing through a meander-shaped pick-up coil. Colors indicate the amplitude, and lines the direction of $\boldsymbol{B}$.

onalize it. We focus here on the latter. While it does require more computing time, it describes the system more accurately. Especially collective phenomena including multiple moments are not included in the mean-field approximation. A comparison of the different approaches, as well as the information on the original simulations from the early 2000s, are available in literature [Sch00, Ens00, Fle03]. Additionally, the reader may refer to our previous publication on the topic [Her22], where we primarily discuss the distribution of energy levels and an erbium concentration scaling relation [Sou69], or to similar work recently published by a different group [Ger23]. In the following, we first describe the simulation in detail, and then discuss a number of necessary code optimizations. We present simulation results relevant to high temperature MMCs, and finally discuss the influence of the nuclear moments of erbium and gold, which are not included in this simulation.

3.2.1 Simulation Process

Given a host material (silver or gold), an erbium concentration x_{Er}, an amplitude B of the magnetic field, and a temperatures T, our aim is to find three quantities: the magnetization M, the slope of the magnetization $\frac{\partial M}{\partial T}$, and the specific heat c of this Ag:Er or Au:Er alloy. While technically only the latter two are necessary for determining the performance of an MMC, the magnetization is of interest for other experiments, such as specific heat measurements [Vel19, Her21], and does not require much more effort to calculate. A flow chart of the simulation appears in figure 3.3. Overall, we divide the process into four steps: First, we prepare the lattice, by randomly distributing magnetic moments on fcc sites, applying periodic boundary conditions, and setting a magnetic field with random orientation. Second, we construct the Hamiltonian of this system and diagonalize it. Third, we calculate

the resulting occupation probabilities of the microstates and expectation values of a number of quantities. Finally, we calculate the thermodynamic properties from these quantities. In order to obtain consistent results, we repeat the simulation with different erbium configurations and average the results.

Step 1: Lattice Preparation

Before constructing the lattice, we must choose the number of magnetic moments N_{Er} in our simulated system. Larger numbers yield more precise results, since more complex dynamics are modeled. However, the rank of the Hamiltonian matrix increases by a factor of two per additional spin, which has detrimental effects on computation time and memory usage. Our tests show that values between 6 and 12 are reasonable, with $N_{\mathrm{Er}} = 9$ being the best compromise between speed and accuracy, given the present hardware. Based on N_{Er} and the erbium concentration, we construct an fcc lattice of appropriate size and randomly distribute the magnetic moments on lattice sites. Since moments at edges and corners experience a lower effective concentration, we apply periodic boundary conditions, by copying the lattice 26 times to create a $3 \times 3 \times 3$ matrix of identical lattices. It is important to note that the copied systems are not independent and thus do not increase the size of the Hamiltonian. We use only the magnetic moments from the central lattice to calculate the thermodynamic properties. As a final step, we choose the magnetic field $\boldsymbol{B}$ to point in z-direction and then rotate the matrix of lattices by a random angle, so that $\boldsymbol{B}$ effectively has a random orientation.

Step 2: Hamiltonian Construction

As we discuss in section 2.2, both the Zeeman splitting due to the external magnetic field, as well as interactions between erbium ions influence the energy of a particular arrangement of spins. In order to calculate the possible energy levels for the lattice we prepared, we construct the corresponding Hamiltonian. As a basis for the Hamiltonian, we choose $|S_1, S_2, \ldots, S_{\mathrm{N_{Er}}}\rangle$ with $S_a \in \{|\uparrow\rangle, |\downarrow\rangle\}$, meaning that the Hamiltonian has dimensions of $2^{N_{\mathrm{Er}}} \times 2^{N_{\mathrm{Er}}}$ and $2^{2N_{\mathrm{Er}}}$ entries. We now fill these entries based on equations (2.4), (2.5), and (2.7) by considering each pairwise interaction, including interactions with spin clones from the 26 surrounding lattices. Note that off-diagonal entries are non-zero, due to ladder operators S_+ and S_- originating from the scalar products

$$\boldsymbol{S}_i \cdot \boldsymbol{S}_j = \frac{1}{2}\left(S_i^+ S_j^- + S_i^- S_j^+\right) + S_i^z S_j^z \tag{3.1}$$

in the dipole-dipole and RKKY terms. An example of a complete Hamiltonian in a system with just two magnetic moments is available in literature [Sch00, Fle03].

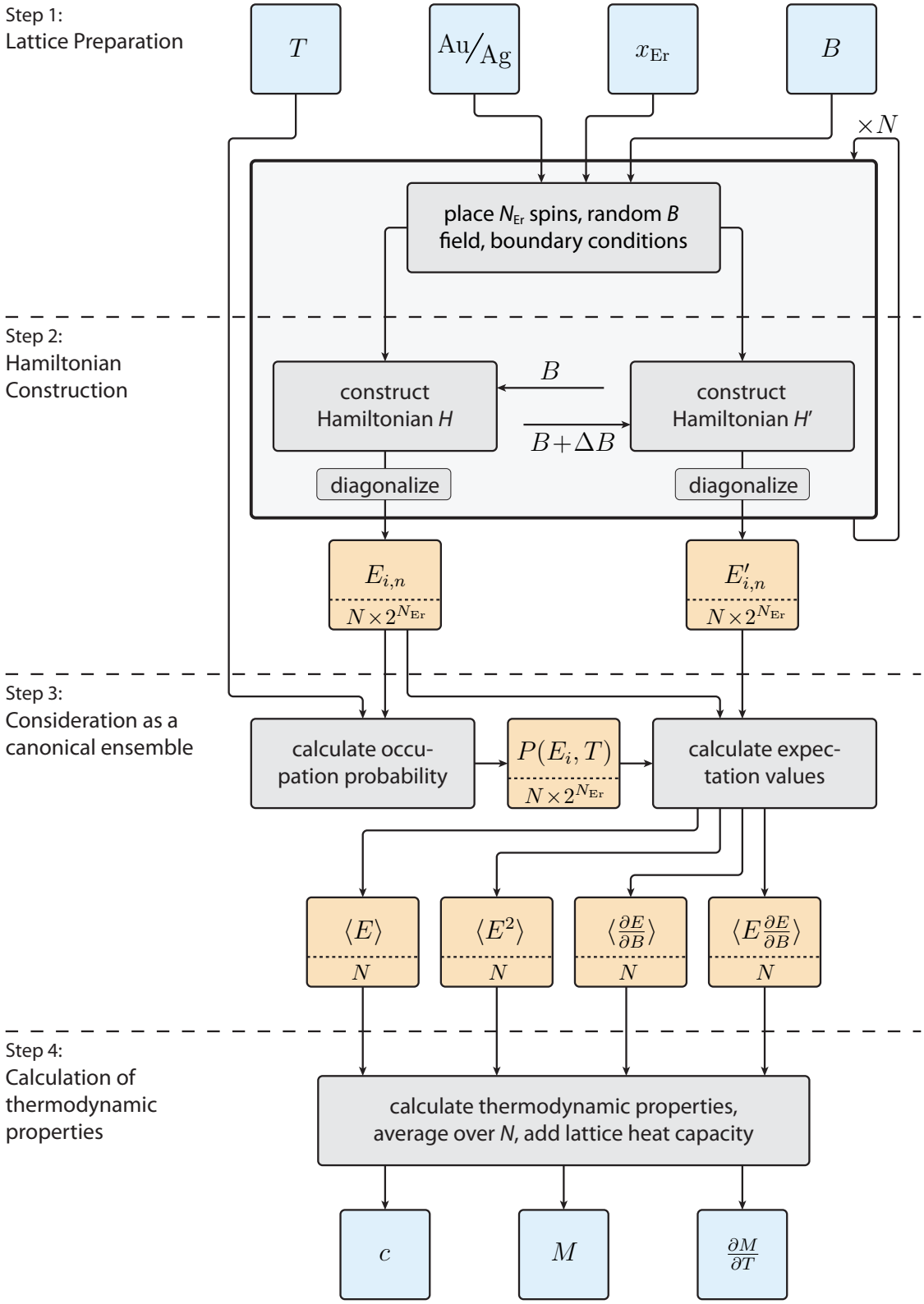

Figure 3.3: Flow diagram for simulating the sensor material. Calculations detailed in the main text appear in gray. Input and output parameters are blue and intermediate results orange. For arrays, the number of elements is written beneath the dotted lines.

Diagonalizing the Hamiltonian gives us the energy eigenstates E_i of this particular random arrangement of spins.

For later calculation of the magnetic properties, it is also necessary to repeat the process above for a slightly larger field $B' = B + \Delta B$. This influences only the Zeeman terms, so the resulting Hamiltonian H' is only slightly altered. However, a second diagonalization is necessary. Additionally, we must repeat all steps discussed so far for other spin distributions, so that we can later average results and obtain representative thermodynamic properties for the erbium alloy in general. Given $N_{\mathrm{Er}} = 9$, our tests show that we get both consistent and accurate results when averaging $N = 10\,000$ times. The result of this step are the two arrays $E_{i,n}$ and $E'_{i,n}$ representing the possible energy levels in magnetic fields B and B'.

Step 3: Consideration as a Canonical Ensemble

After finding the energy levels E_i of a particular configuration of spins, we can determine the expectation value of a number of relevant quantities. This is dependent on the temperature T, so we shift to a thermodynamic view of the problem. Specifically, we work in the framework of a canonical ensemble, where E_i represent the energies of the ith microstate. Using the partition function

$$Z(T) = \sum_i e^{-E_i/k_{\mathrm{B}}T} \quad , \tag{3.2}$$

we find the occupation probability $P(E_i)$ of a microstate i to be

$$P(E_i, T) = \frac{1}{Z(T)} e^{-E_i/k_{\mathrm{B}}T} \quad . \tag{3.3}$$

Finding the expectation value $\langle X \rangle$ of a quantity X then is a matter of calculating

$$\langle X \rangle(T) = \sum_i P(E_i, T) X_i \quad . \tag{3.4}$$

For our purposes, we calculate $\langle E \rangle(T)$, $\langle E^2 \rangle(T)$, $\langle \frac{\partial E}{\partial B} \rangle(T)$, and $\langle E \frac{\partial E}{\partial B} \rangle(T)$. For the latter two, we use the energy levels E'_i to calculate the slope

$$\left(\frac{\partial E}{\partial B} \right)_i \approx \frac{E'_i - E_i}{\Delta B} \quad . \tag{3.5}$$

Step 4: Calculation of Thermodynamic Properties

Given that we are working with a canonical ensemble, the appropriate thermodynamic potential is the Helmholtz free energy

$$F = -N_{\mathrm{Er}} k_{\mathrm{B}} T \ln Z \tag{3.6}$$

with the differential

$$\mathrm{d}F = -S\mathrm{d}T - VM\mathrm{d}B - p\,\mathrm{d}V \quad , \tag{3.7}$$

where we introduce the entropy S, the volume V, the pressure p. Here, the last term can be neglected, as p and $\mathrm{d}V$ are small. We can now use the equations above to calculate

$$\begin{aligned} c(T) &= \frac{x_{\mathrm{Er}} N_{\mathrm{A}}}{N_{\mathrm{Er}} k_{\mathrm{B}} T^2} \left(\langle E^2 \rangle - \langle E \rangle^2 \right) \quad , \\ M(T) &= -\frac{N_{\mathrm{Er}}}{V} \left\langle \frac{\partial E}{\partial B} \right\rangle \quad , \text{ and} \\ \frac{\partial M}{\partial T}(T) &= \frac{N_{\mathrm{Er}}}{V k_{\mathrm{B}} T^2} \left(\left\langle E \frac{\partial E}{\partial B} \right\rangle - \langle E \rangle \left\langle \frac{\partial E}{\partial B} \right\rangle \right) \end{aligned} \tag{3.8}$$

for each individual arrangement of magnetic moments, where $N_{\mathrm{A}} = 1.022 \times 10^{23} \mathrm{mol}^{-1}$ is the Avogadro constant. Finally, we add the specific heat of the lattice and average over all N erbium configurations.

3.2.2 Technical Details and Performance

Performing the described sensor simulations both accurately and efficiently requires some attention to detail. Accuracy is not trivial, since the calculations include a mixture of very small and very large numbers. Efficiency is not optional, since we wrote the code in the comparatively slow programming language python, in order to make it as accessible as possible. We list the most important technical details here.

- When constructing the Hamiltonians, we perform **pre-calculations** of r_{ij}^{-3} and the polar and azimuthal angles for each pair of spins i, j with efficient use of numpy arrays [Har20]. The number of calculations using vectors thus reduces from $\mathcal{O}(2^{2N_{\mathrm{Er}}})$ to $\mathcal{O}({N_{\mathrm{Er}}}^2)$.
- When filling the entries of the Hamiltonians, we use the compiler **Numba**[2] for just-in-time compilation and parallel computing [Lam15].
- Since the matrices describing the Hamiltonians are **hermitian**, we may use significantly faster diagonalization algorithms.

[2] https://numba.pydata.org.

- Since simulations at different temperatures do not require unique Hamiltonians, we perform calculations in steps 3 and 4 for many **temperatures in parallel**.
- The occupation probability matrix $P(E_i, T)$ can quickly **exceed working memory**. For typical parameters of $N_{\mathrm{Er}} = 9$, $N = 10\,000$, and 391 temperature steps between 10 mK and 400 mK, the matrix of P contains $391 \times 2^9 \times 10\,000 \approx 2 \times 10^9$ 64-bit floating-point numbers and thus has a size of 16 GB. The code automatically divides steps 3 and 4 into smaller temperature chunks, calculating them sequentially.
- When calculating the partition function Z according to equation (3.2), the magnitude of terms varies significantly. We use **Kahan summation** [Kah65], in order to reduce the numerical error. Similarly, we must account for potential catastrophic cancellation [Mul18] when calculating the thermodynamic properties according to equations (3.8).
- At low temperatures and spin configurations with large gaps in E_i (densely packed erbium clusters), it becomes unlikely that high energy levels are occupied. Certain terms in equations (3.2) and (3.3) can quickly exceed the maximal possible floating point number native to numpy. Our code detects such cases, and performs the relevant calculations using the **decimal package**, which theoretically allows for arbitrarily large numbers. However, this does increase computation time significantly.

Overall, we are able to simulate $N = 10\,000$ configurations with $N_{\mathrm{Er}} = 9$ spins at $N_T = 391$ temperature steps on a standard desktop PC[3] in 82 minutes, where the largest part (53 minutes) is the diagonalization of the Hamiltonians. In this way, we built up an extensive repository of simulated c, M, and $\partial M/\partial T$ of Au:Er and Ag:Er for $10\,\mathrm{mK} \leq T \leq 400\,\mathrm{mK}$, $0\,\mathrm{mT} \leq B \leq 60\,\mathrm{mT}$, and $0\,\mathrm{ppm} \leq x_{\mathrm{Er}} \leq 3200\,\mathrm{ppm}$ over the course of three weeks.

3.2.3 Simulation Results

In figure 3.4 appear simulation results for an erbium alloy with $x_{\mathrm{Er}} = 2400\,\mathrm{ppm}$ at magnetic fields of $0\,\mathrm{mT} \leq B \leq 20\,\mathrm{mT}$ and temperatures of $10\,\mathrm{mK} \leq T \leq 400\,\mathrm{mK}$. The specific heat on the left is a measure for the distribution of energy levels in the system, since, to first order, an energy difference ΔE between two energy levels causes a Schottky anomaly

$$C_{\mathrm{S}} = k_{\mathrm{B}} \left(\frac{\Delta E}{k_{\mathrm{B}} T} \right)^2 \frac{e^{\Delta E / k_{\mathrm{B}} T}}{(1 + e^{\Delta E / k_{\mathrm{B}} T})^2} \quad , \tag{3.9}$$

[3] Intel©Core™i5-8500 (6 CPUs), 8 GB RAM, no external GPU, Windows 10.

with a maximum of $0.44\,k_\mathrm{B}$ per particle at $T = 0.42\,\Delta E/k_\mathrm{B}$. Zeeman splitting of the Γ_7-doublet, for instance, contributes to the large peak at $\sim 40\,\mathrm{mK}$ for highest magnetic fields. In a system of interacting magnetic moments, however, the random distance between erbium ions causes random shifts of the energy levels. The result is a broader peak, which necessarily is less tall due to conservation of entropy $S = \int C(T)/T\mathrm{d}T$. In the extreme of $B = 0\,\mathrm{mT}$, the broad maximum reflects the distribution of energy levels caused by spin-spin interactions. We have shown previously that the tail at $T \gtrsim 100\,\mathrm{mK}$ is the result of particularly strong locking of individual pairs of erbium ions in certain relative arrangement, which is discussed in detail in [Her22]. For instance, we expect a maximum at around 360 mK due to the RKKY interaction between two erbium ions at a relative position of $(1/2, 1/2, 1)a$, where $a = 4.08\,\text{Å}$ is the side length of the cubic fcc host cell. Such a side peak is visible in the form of B-independent excessive heat capacity at 360 mK in figure 3.4.

Simulation results for the magnetization $M(T)$ appear on the right of figure 3.4. In the limit of non-interacting spins, we expect

$$M = \frac{x_\mathrm{Er} N_\mathrm{A}}{V_\mathrm{mol}} \tilde{g}\tilde{S}\mu_\mathrm{B}\mathcal{B}_{\tilde{S}}(h) \tag{3.10}$$

where V_mol is the molar volume, $h = \tilde{g}\tilde{S}\mu_\mathrm{B}B/(k_\mathrm{B}T)$ is the ratio of magnetic and

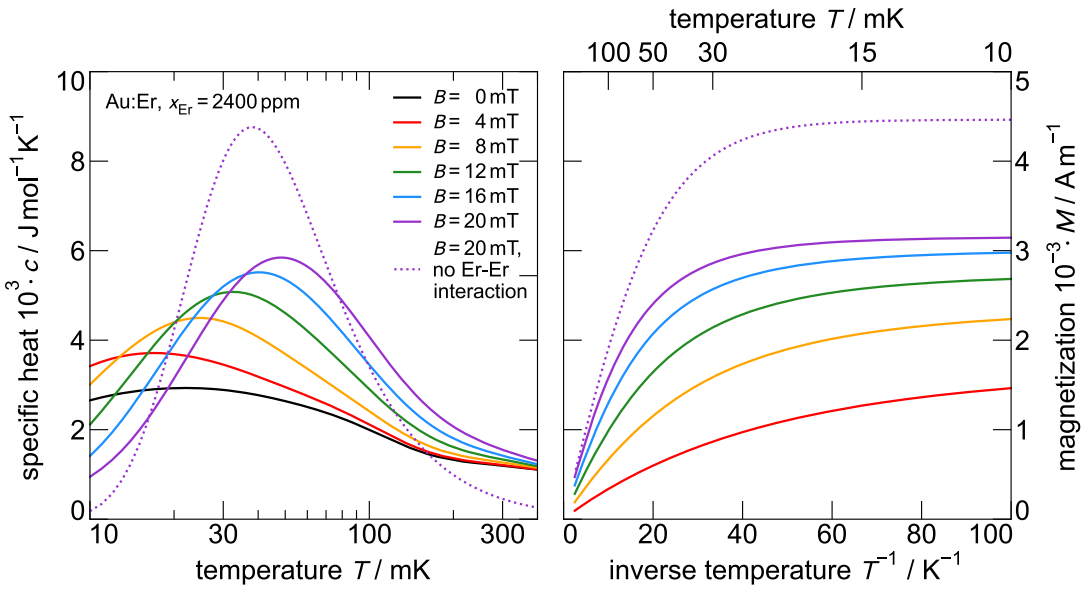

Figure 3.4: Simulated specific heat and magnetization with parameters typical for our high temperature MMCs. We can interpret the specific heat to first order by a sum of Schottky peaks, and the magnetization follows Curie-like behavior at high temperatures. The dotted lines represent a non-interacting system at $B = 20\,\mathrm{mT}$.

thermal energy, and the Brillouin function $\mathcal{B}(h)$ for $\tilde{S} = 1/2$ is $\mathcal{B}_{\tilde{S}=1/2}(h) = \tanh(h)$. For $B = 20\,\mathrm{mT}$, the result is the dotted line, with high temperature behavior well described by the Curie law $M \propto T^{-1}$. At low temperatures, the magnetization approaches a B-independent value of $\frac{x_{\mathrm{Er}} N_{\mathrm{A}}}{V_{\mathrm{mol}}} \tilde{g} \tilde{S} \mu_{\mathrm{B}} \approx 4500\,\mathrm{A/m}$. In the simulated interacting system, however, we do not reach this limit, since some erbium ions are locked in anti-parallel orientations and do not contribute to M. When reducing the magnetic field B, the outside orienting force reduces as well and the number of contributing magnetic moments is lower. Also, thermal activation plays a role down to lower temperatures, so the low T limit is reached only at lower temperatures.

3.2.4 Influence of Nuclear Moments

In our quantum-mechanical calculations of the sensor material, we do not incorporate hyperfine splitting. The reason is that this would break the approximation of a $\tilde{S} = 1/2$ ground state, which allows the Hamiltonian to be comparatively small with a rank of $2^{N_{\mathrm{Er}}}$. Including hyperfine effects from ^{167}Er, for instance, would add $7 + 9 = 16$ energy levels from the $F = 3$ and $F = 4$ states, increasing the rank of the Hamiltonian to $(2 \times 16)^{N_{\mathrm{Er}}}$. Previous simulations using the mean-field method have included hyperfine effects at the cost of other drawbacks [Fle00]. Their results show an additional Schottky anomaly in the specific heat at $50-60\,\mathrm{mK}$, which aligns well with the expected splitting between the $F = 3$ and $F = 4$ multiplet at $B = 0$. From a direct comparison with our simulations, we find that adding a Schottky anomaly with $\Delta E/k_{\mathrm{B}} = 140\,\mathrm{mK}$ and an amplitude of $0.18\,k_{\mathrm{B}}$ per ppm of erbium to our simulations is a good first-order approximation for erbium alloys with natural isotopic composition. The energy gap between different m_F at $B \neq 0$ within each of the two hyperfine multiplets is typically an order of magnitude lower, and thus lies outside our temperature range of interest [Fle03].

Due to this increase in heat capacity, the presence of ^{167}Er degrades the performance of MMCs. For this reason, modern MMCs typically use erbium alloys depleted of the isotope ^{167}Er, where the fraction of ^{167}Er is significantly reduced. For these applications, our simulations are a good fit. However, as we explain in section 4.1, the MMCs discussed in this thesis use erbium with a natural isotopic composition, and we must apply the specific heat correction detailed above.

3.3 Detector Simulations

Given the detector parameters, magnetic field distribution, and the thermodynamic properties of the sensor, we now present our software designed to calculate and optimize the resulting energy resolution of an MMC. A detailed description of this

process from a theoretical standpoint is available in literature [Fle05, Fle09a], so we focus here specifically on the implementation in code. In the following, we initially give an overview of the basic simulation process, before covering additional features of our code. Simulation results for an MMC follow in subsection 4.1.2.

3.3.1 Simulation Process

Before simulation can begin, the user must supply a list of the relevant detector parameters in an external file, as well as appropriate magnetic field and sensor simulation results. The process of calculating the energy resolution then consists of seven steps:

1. Create a square 2D grid of points, each representing the cross-section of one infinitesimal volume element $\mathrm{d}V$ in equation (2.13). The grid covers only the width of two lines, just as the magnetic field simulations. Then, read in the magnetic field simulations and perform a spline-fit interpolation of the data, to obtain a continuous function $B(\boldsymbol{x})$. Evaluate $B(\boldsymbol{x})$ at the grid sites.
2. Read in the simulations of the thermodynamic properties of the sensor material. Interpolate the data, in order to get continuous functions $c(B)$ and $\frac{\partial M}{\partial T}(B)$. Interpolation over temperature is not necessary, since the simulation of the thermodynamic properties of the sensor material gives a high density of temperatures. We simply choose the closest simulated temperature. In comparison, a high density of simulated magnetic fields would require a repeated diagonalization of the Hamiltonian and would be, therefore, unpractical.
3. Evaluate the specific heat $c(\boldsymbol{x})$ and $G \cdot \frac{\partial M}{\partial T}(\boldsymbol{x})$ at each lattice site from step 1, given the magnetic field at that location.
4. Sum the so-calculated values over all mesh sites, then scale the results to the size of the full sensor to obtain C_{sens} and $\int_V G \frac{\partial M}{\partial T} \mathrm{d}V$.
5. Calculate $\delta\Phi_{\mathrm{m}}/\delta E$ using the results above and equation (2.13). Then, calculate the flux coupling $\delta\Phi/\delta\Phi_{\mathrm{m}}$ to the front-end SQUID using equations (2.14) and (2.16), to obtain $\delta\Phi/\delta E$.
6. Calculate the total noise $S_{\Phi,\mathrm{tot}} = \sum_i S_{\Phi,i}$ in the MMC. Table 3.1 offers an overview of all relevant noise components $S_{\Phi,i}$. Listed in the central column are formulae to calculate the respective contributions. Note that we add appropriate coupling factors $\frac{\delta\Phi}{\delta\Phi_{\mathrm{m}}}$, $\frac{\delta\Phi}{\delta\Phi_{\mathrm{exp}}}$, and $\beta^{-1}\frac{\delta\Phi}{\delta E}$, so that the listed formulae all refer to the magnetic flux noise S_Φ in the front-end SQUID. Additionally, we include factors of 2 where appropriate, since the MMCs discussed here typically use the gradiometric design presented in section 2.3, which includes two pixels per read-out channel. Each formula has a corresponding equation with

Noise	$\boldsymbol{S_\Phi = \ldots}$	**Reference**
read-out noise	$S_{\Phi,\mathrm{w}} + S_{\Phi,1/f}$	equations (7.1), (7.2) subsection 7.1.1
Johnson noise: sensor	$2\left(\frac{\delta\Phi}{\delta\Phi_\mathrm{m}}\right)^2 \cdot S_{\Phi,\mathrm{J,m}}$	equation (6.9) subsection 7.4.3
Johnson noise: absorber	$2\left(\frac{\delta\Phi}{\delta\Phi_\mathrm{m}}\right)^2 \cdot S_{\Phi,\mathrm{J,m}}$	equation (6.9)
Johnson noise: exp. platform	$\left(\frac{\delta\Phi}{\delta\Phi_\mathrm{exp}}\right)^2 \cdot S_{\Phi,\mathrm{J}}$	equation (6.10) subsection 7.4.4
erbium noise: Au:Er (high x_Er)	$2\left(\frac{\delta\Phi}{\delta\Phi_\mathrm{m}}\right)^2 S_{\Phi,\mathrm{Er}}$	equation (6.12) subsection 7.4.2
erbium noise: Ag:Er (low x_Er)	$2\left(\frac{\delta\Phi}{\delta\Phi_\mathrm{m}}\right)^2 S_{\Phi,\mathrm{Er}}$	equation (6.12) subsection 7.4.3
energy fluctuations	$2\,\beta^{-2}\left(\frac{\delta\Phi}{\delta E}\right)^2 S_\mathrm{ef}$	equation (6.14)

Table 3.1: Noise contributions that may affect an MMC. The formulae in the center column refer to the magnetic flux noise in the front-end SQUID as a result of each contribution. Parameters are explained in the listed equation references. We also measure a selection of the noise components in chapter 7.

more details. For some noise components, we additionally perform dedicated measurements in chapter 7, and we list the appropriate sub-sections.

7. Calculate the energy resolution ΔE_FWHM according to equations (2.22) and (2.23). Note that we must first translate the flux noise $S_{\Phi,\mathrm{tot}}$ from step 6 to energy fluctuations

$$S_\mathrm{s,tot} = S_{\Phi,\mathrm{tot}}\ \beta^2 \left(\frac{\delta E}{\delta\Phi}\right)^2 \tag{3.11}$$

in the spin system.

3.3.2 Additional Features

Besides the basic calculation of a detector's energy resolution as described above, our code has a number of additional capabilities, in order to make it as widely usable as possible:

- For the parameters T, I_0, x_Er, p, and L_i, as well as the sensor and absorber dimensions, we can quickly iterate through different combinations of values by providing **arrays of input parameters**. The code is structured as a set of

nested loops that minimizes duplicate calculations. Given a fixed ratio w/p, the width w of the meander lines is adjusted to the pitch p.

- The code can automatically **optimize** the above parameters when given upper and lower bounds.
- Our code returns the ratio $\delta\Phi/\delta E$, from which we can calculate the expected **pulse height** $\delta\Phi/\delta E \cdot \delta E$ upon impact of a particle with energy δE.
- Given simulated values of $M(B,T)$, our code returns the expected measured flux upon temperature change, from which we can calculate **magnetization curves**.
- Our code returns the **noise spectrum**, including all components listed in table 3.1.
- We can simulate **non-standard designs**, which include concepts such as double transformer coupling [Muh83], integrated SQUID read-out [Zak03], the hydra principle [Por11], and variable amounts of pixels per read-out channel [Gam19].

4. Quasy-maXs - an MMC Operated at 85 mK

Particle Induced X-ray Emission (PIXE) is a non-destructive technique for analyzing the atomic composition of materials [Joh70, Joh76]. A sample is illuminated with a beam of protons or heavier particles with energies in the low MeV range. As a result, atoms are ionized, in part by the removal of electrons from inner shells. The resulting de-excitation spectrum is characteristic for each element and typically lies in the X-ray range. Applications of PIXE are widespread [Ish19], ranging from archaeology [Pop18] to astrophysics [Nul20].

One crucial component of PIXE spectroscopy is the X-ray detector. While solid state Si(Li) detectors with resolving powers $E/\Delta E_{\mathrm{FWHM}} \gtrsim 35$ and $\Delta E_{\mathrm{FWHM}} \gtrsim 70\,\mathrm{eV}$ are commonly used [Joh88, IAE00], AHEAD2020 project[1], we have collaborated with the Lisbon team to upgrade their TES-based system with a custom-made MMC [Rei23], in the hope of improving on this performance and establishing MMCs as a new technology in this field. To this end, we have, for the first time, developed an MMC specifically designed for PIXE applications: the ***Qu****adratic* ***Asy****mmetric* ***M****MC* ***A****rray for* ***X****-ray* ***S****pectroscopy* (Quasy-maXs). A digital render[2] of this chip appears in figure 4.1. The name is based on the six pixels in the center. Four of the pixels form a 2×2 square, and one lies on either side as part of asymmetric channels. A motivation for this design based on a discussion of the boundary conditions of the envisaged application is the focus of section 4.1. We also present simulations and

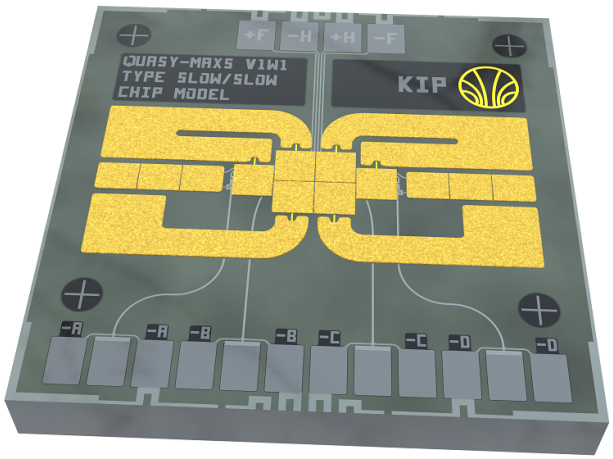

Figure 4.1: Digital render of a Quasy-maXs chip, an MMC designed for particle induced X-ray emission spectroscopy at 85 mK.

[1] Integrated Activities for the High Energy Astrophysics Domain – AHEAD2020, EU Horizon 2020 Framework Programme GA number 871158, ahead.iaps.inaf.it.

[2] All digital renders in this thesis were created with Blender [Com18], http://www.blender.org.

optimization of the energy resolution, with details on the chip and custom-made experimental set-up following in section 4.2. Quasy-maXs is set to see first X-rays in Portugal in mid 2023, and we have characterized the detector in a cryostat in our institute in order to demonstrate its functionality. We present results of these characterizations in section 4.3. Finally, an outlook and suggestions for further optimizing the detector round off this chapter in section 4.4.

4.1 Designing Quasy-maXs

In this section we consider the desired capabilities of the detector, as well as limitations from the broader experimental surroundings. Based on these points, we simulated the detector to find the optimal design parameters.

4.1.1 Design Requirements and Limitations

Since Quasy-maXs is designed for PIXE spectroscopy, the chip and the experimental set-up is heavily influenced by the specific experimental requirements and restrictions. The aim is to construct a detector with the best possible energy resolution within these limitations. We list the most important points here.

- Quasy-maXs must be able to operate in a small, pulse-tube cryostat coupled with an adiabatic demagnetization stage [Rei17b]. This limits the operating **temperature** to $\geq 85\,\mathrm{mK}$.
- PIXE requires no spatial resolution, meaning that a **single pixel** is sufficient. As a result, Quasy-maXs features two asymmetric channels with one pixel and one load inductance without sensor each. This design improves the energy resolution over the classic gradiometric design presented in section 2.3 by up to a factor of $\sqrt{2}$. For operation, the user may choose to illuminate the pixel of either of the two asymmetric channels, with the other acting as a back-up. The central square of four pixels form two gradiometric channels. While in theory having a worse energy resolution, these are less sensitive to temperature or magnetic field variations and may be better suited in some applications.
- In the desired energy range of up to 20 keV [Rei23], the **stopping power** of the absorbers must be sufficiently high to efficiently detect X-rays. We choose absorbers made of gold with a thickness of 5 µm, which absorb over 50 % of the photons across the entire energy range [Hub09].
- The X-rays emitted from the sample are focused by an X-ray lens and then run through a circular collimator with a diameter of 200 µm, so the **absorber**

footprint must be sufficiently large to fully cover the beam. We choose a square absorber with a size of 250 µm × 250 µm.

- The detector must be able to handle a **rate** of 50 photons per second [Rei23]. This limits the decay time τ_1.
- **Alignment** of the absorber in the beam is crucial. The experimental platform with the chip must be movable in the 2D plane orthogonal to the beam and aligned to within a few dozen micrometers. In beam direction, the absorber must be dependably placed at a distance of 500 µm from the X-ray optics.
- The entire system, including the low-temperature read-out chain must be **compact** enough to fit on a cryostat arm contained within a shield with a diameter of 29 mm.

Besides these points related to PIXE spectroscopy, one additional restriction is that we are limited to a single Au:Er alloy throughout all experiments in this thesis. In order to allow for sputter deposition in our cleanroom, we require a sputtering target. The material costs of enriched erbium is high, and enriched ^{168}Er or ^{168}Er in metallic form is currently very difficult to obtain on the market. For this reason, we are limited to Au:Er with an erbium concentration of $x_{\mathrm{Er}} \approx 2500\,\mathrm{ppm}$ with natural isotopic composition. We discuss the chosen erbium concentration in subsection 5.1.1 and describe construction of an appropriate target in subsection 5.2.1.

4.1.2 Simulation and Optimization

The simulation of Quasy-maXs follows the process detailed in chapter 3. One important point we have to consider is the altered geometry of the asymmetric channels. Instead of two identical pick-up coils, each with an inductance L_{m}, these channels contain one normal pick-up coil and one load inductor $L_{\mathrm{load}} \gg L_{\mathrm{m}}$. Using Kirchhoff's rules, we find that this increases the flux coupling from that in equation (2.14) to

$$\delta I = \frac{\delta \Phi_{\mathrm{m}}}{L_{\mathrm{m}} + L_{\mathrm{i}} + L_{\mathrm{w}} + \frac{L_{\mathrm{m}}(L_{\mathrm{i}}+L_{\mathrm{w}})}{L_{\mathrm{load}}}} \approx \frac{\delta \Phi_{\mathrm{m}}}{L_{\mathrm{m}} + L_{\mathrm{i}} + L_{\mathrm{w}}} \quad , \tag{4.1}$$

which would be an increase by up to a factor of ~ 2 in the limit of $L_{\mathrm{i}} + L_{\mathrm{w}} \gg L_{\mathrm{m}}$.

We now discuss the simulation and optimization of the detector for asymmetric pixels at 85 mK, while keeping in mind the restrictions detailed in the previous section. In table 4.1, we list the most important detector parameters in the first column. The result of the optimization are the design values in column 2. For some parameters, measurements after construction of the chip showed slight deviations from the design

Parameter	Design Value	Measured Value	Note
Pick-up coil:			
pitch p	5 µm	5 µm	optimized
width w	2.5 µm	2.5 µm	optimized: $p/2$
niobium height h_{Nb1}	250 nm	269 nm	optimized
SiO_2 height h_{iso}	350 nm	458 nm	optimized
persistent current I_0	100 mA	68 mA	limited by width
Sensor:			
side length a_{s}	120 µm	120 µm	optimized
height h_{s}	500 nm	446 nm	optimized
concentration x_{Er}	2500 ppm	2660 ppm	manufacturing limited
Absorber:			
side length a_{a}	250 µm	250 µm	PIXE requirement
height h_{a}	5 µm	5.28 µm	PIXE requirement
Time constants of fast/fast-type chip at 85 mK:			
rise time τ_0	82 ns	480 ns (63 %)	subsections 4.2.2, 4.3.3
decay time τ_1	500 µs	142 µs (51 %)	subsections 4.2.2, 4.3.3
Time constants of slow/slow-type chip at 85 mK:			
rise time τ_0	24 µs	24 µs (62 %)	subsections 4.2.2, 4.3.3
decay time τ_1	840 µs	612 µs (100 %)	subsections 4.2.2, 4.3.3
Noise of read-out chain:			
$1/f$ noise $\sqrt{S_{\Phi,1/f}}(1\,\mathrm{Hz})$	$3\,\mu\Phi_0/\sqrt{\mathrm{Hz}}$	$5.5\,\mu\Phi_0/\sqrt{\mathrm{Hz}}$	subsection 7.1.1
$1/f$ noise exponent	1	0.74	subsection 7.1.1
white noise $\sqrt{S_{\Phi,\mathrm{w}}}$	$0.3\,\mu\Phi_0/\sqrt{\mathrm{Hz}}$	$0.20\,\mu\Phi_0/\sqrt{\mathrm{Hz}}$	subsection 4.3.4
Erbium noise			
$1/f$ noise $S_{\mathrm{m},1/f}(1\,\mathrm{Hz})$	$0.1\,\mu_{\mathrm{B}}^2/\mathrm{Hz}$	$0.115\,\mu_{\mathrm{B}}^2/\mathrm{Hz}$	subsection 7.4.2
$1/f$ exponent α	-0.9	-1.00	subsection 7.4.2
Johnson noise from the experimental platform:			
white noise $\sqrt{S_{\Phi,\mathrm{J}}}(1\,\mathrm{Hz})$	–	$2.9\,\mu\Phi_0/\sqrt{\mathrm{Hz}}$	subsection 7.4.4
critical frequency f_{c}	–	143 Hz	subsection 7.4.4
low-pass exponent γ	–	1.19	subsection 7.4.4

Table 4.1: Results of simulating Quasy-maXs and experimentally determined values.

value, which we list in the third column. Specifically, we measured the heights of various components with a stylus profilometer[3] and the noted erbium concentration of the sensor results from magnetization measurements using a commercial magnetometer[4]. Measurements of noise components are explained in chapter 7. Note that we did not include Johnson noise from the experimental platform in our simulations, since we only realized its relevancy in later noise measurements. Four time constants are listed, since we produced different versions of the Quasy-maXs chips with different signal rise times and different decay times. As we demonstrate later in subsection 4.2.2, our measurements show that the pulse shape has multiple rise and decay times. We list here the dominant one and its weight in percent, with more information available in table 4.4.

Our simulations project an energy resolution of $\Delta E_{\mathrm{FWHM}} = 8.5\,\mathrm{eV}$ for a fast/fast type chip at 85 mK, based on the design values. When simulating with the measured values after construction, we calculate an energy resolution of $\Delta E_{\mathrm{FWHM}} = 11.3\,\mathrm{eV}$. Main reasons for the difference are the significantly lower persistent current, an increased ratio of rise and decay time, and the 30 % thicker SiO_2.

4.2 Experimental Methods

Based on the simulation results above, we present the Quasy-maXs detector chip, as well as a custom experimental platform optimized for PIXE spectroscopy. Furthermore, we discuss different thermalization options, which allow us to use the detector at a wide range of temperatures.

4.2.1 The Quasy-maXs Chip

Following the design parameters in table 4.1, we construct the Quasy-maXs chip depicted in figure 4.2. Its base consists of a 3.2 mm × 3.2 mm × 380 µm silicon substrate, on which we structure a total of eleven micro-fabricated layers as listed in table 4.2, while it is still part of a three inch silicon wafer. These layers make up four basic components of the chip: a collection of six pixels at the center of the chip, four persistent current switches, four heat baths, and two sets of bond pads. In the following, we explain each of these components in detail.

The six **pixels** are located at the center of the chip. They are separated into four channels arranged from left to right. The two central channels are of a gradiometric type, as introduced in section 2.3 and are each composed of two pixels (1). The

[3] DektakXT from Bruker Corporation, 40 Manning Rd, Billerica, MA 01821, USA.
[4] QD MPMSR XL by Quantum Design GmbH, Im Tiefen See 58, 64293 Darmstadt, Germany.

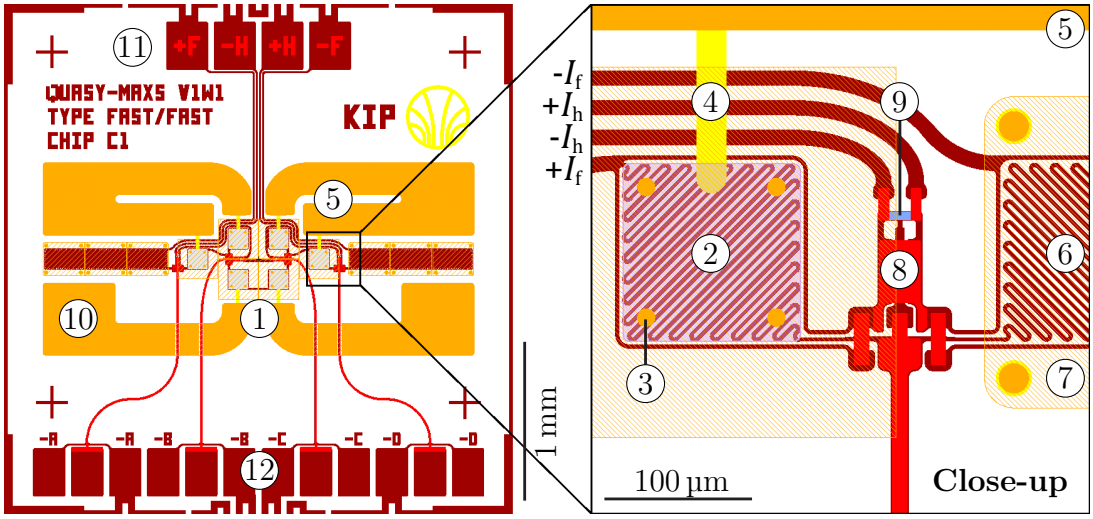

Figure 4.2: Left: Technical drawing of the entire Quasy-maXs chip. Superconducting niobium structures appear in dark and bright red, and thermalization structures made of gold appear in orange and yellow. Absorbers are hatched in orange and isolating layers are omitted for improved visibility. **Right:** Close-up of the right asymmetric channel. Au:Er sensor material is represented by purple hatching, and the AuPd persistent current switch is marked in blue.

left and right channels, on the other hand, each feature a normal pixel containing a pick-up coil, and a load inductor. A close-up of a representative section of the chip appears on the right of figure 4.2. On the left lies a standard pixel (2) with a 120 µm × 120 µm patch of sensor material covering the pick-up coil with a pitch of 5 µm and a width of 2.5 µm. Using equation (2.10), we find a meander inductance of $L_m = 0.80\,\text{nH}$. Located on top of the sensor is the absorber. It sits suspended on four gold stems (3), which mitigate energy loss via athermal phonons. This leads to a more consistent pulse height and signal rise time τ_0. The signal decay time τ_1 is defined by a strip of sputter-deposited gold (4). Heat flows along this path to the large on-chip heat bath (5). Contrasting this is the load inductor (6) on the right of the close-up. It has identical dimensions to the pick-up coil, except that it is 765 µm wide, giving it an inductance of $L_{load} = 5.1\,\text{nH}$. The load inductor is not designed to detect particles. Consequently, it has neither sensor material nor thermalization structures. Instead, the large stems simply act as supports for a canopy of gold (7), shielding the load inductor from any particle hits.

Between the pick-up coil and the load inductor sits the **persistent current switch** (PCS) (8). It is designed to inject a persistent current (see section 2.4) into the superconducting loop consisting of the pick-up coil and the load inductor. Corresponding supply lines for the field current I_f and heater current I_h are shown. The heater made of a AuPd alloy (9) with a resistance of $R_{PCS} \approx 7\,\Omega$ has dimensions

No.	Name	Material	Height	Color in figure 4.2
1	Nb1	niobium	250 nm	dark red
2	Anodization	niobium oxide	$\sim$ 30 nm	not pictured
3	Iso1a	SiO_2	175 nm	not pictured
4	Iso1b	SiO_2	175 nm	not pictured
5	Heater	AuPd	150 nm	blue
6	Nb2	niobium	600 nm	bright red
7	Iso2	SiO_2	175 nm	not pictured
8	Thermalization	sputtered gold	300 nm	yellow
9	Sensor	Au:Er	500 nm	purple (hatched)
10	Stems	galvanized gold	5 µm	orange
11	Absorber	galvanized gold	5 µm	orange (hatched)

Table 4.2: Overview of the eleven micro-fabricated layers of Quasy-maXs, the material they are made of, the design value for their height, and the color they appear in in figure 4.2.

of 15 µm × 5 µm × 150 nm and appears as a small blue rectangle at the top of the PCS. Note that Quasy-maXs features four PCSs, which are connected in series. As a result, we inject current into all four channels simultaneously.

Going back to the view of the entire chip, four large **heat baths** (5) dominate the design. These consist of a 5 µm thick layer of galvanized gold, giving them a large heat capacity. Their particular shape reduces thermal cross-talk between pixels, by maximizing path lengths between pixels thermally connected via the heat bath. Additionally, the four large square areas (10) at the sides of the chips allow us to add additional thermalization to an off-chip heat bath using gold bonding wires.

For operation and read-out, we connect aluminum bonds to the **bond pads** at the top and the bottom of the chip. The former (11) are for supplying the field and heater current. The latter (12) allow for connections to front-end SQUIDs on a separate chip placed right next to Quasy-maXs, one SQUID per channel. The bond pad layout allows for three bonds to be placed per channel, splitting the negative line into two separate lines. This leads to a more gradiometric arrangement of bonding wires, which is less susceptible to magnetic flux noise [Sch19].

4.2.2 Expected Pulse Shape

While specifically designed for PIXE spectroscopy at 85 mK, we have taken a number of measures to expand the application range of Quasy-maXs to other potential experiments. Besides the option to use the non-asymmetric pixels at the center of the chip, this refers mainly to thermal links, which determine the rise and decay times of pulses. These characteristic times are temperature dependent, since ther-

mal conductivities and heat capacities vary with temperature. As a result, different temperatures require different thermal links. By offering multiple designs with different geometries of the thermal links, Quasy-maXs is well suited for applications anywhere between 15 mK and 120 mK. We can choose from two signal rise times and two signal decay times, resulting in four different types of chips. Close-ups of the design of two different thermalization configurations appear in figure 4.3, where the first term in the name refers to the rise time, and the second to the decay time.

Decay Time. As is apparent in figure 4.3, thermalization to the heat bath occurs via a strip of sputtered gold (yellow). Measurements with the stylus profilometer show that this layer is 270 nm thick, 10 % thinner than designed. For chips with fast decay time, the strip thus has a cross-section of $A_{\mathrm{strip}} = 270\,\mathrm{nm} \times 20\,\mu\mathrm{m}$ and a length of $l_{\mathrm{strip}} = 90\,\mu\mathrm{m}$. For chips with slow decay time, on the other hand, the strip is elongated and narrowed to have dimensions of $A_{\mathrm{strip}} = 270\,\mathrm{nm} \times 10\,\mu\mathrm{m}$ and $l_{\mathrm{strip}} = 130\,\mu\mathrm{m}$, effectively reducing the thermal conductance

$$G_{\mathrm{strip}} = \kappa_{\mathrm{Au,s}} \frac{A_{\mathrm{strip}}}{l_{\mathrm{strip}}} \tag{4.2}$$

by a factor of ~ 3. Here, we calculate the specific thermal conductivity $\kappa_{\mathrm{Au,s}}$ of the sputtered gold from the electric resistivity ρ using the Wiedemann-Franz law

$$\kappa = \frac{\mathcal{L}T}{\rho} \quad \text{with the Lorenz number} \quad \mathcal{L} = 2.44 \times 10^{-8} \frac{\mathrm{V}^2}{\mathrm{K}^2} \quad . \tag{4.3}$$

Note that the electric resistivity of sputtered gold at low temperatures is dominated by defects, which we quantify with the residual resistance ratio $RRR = \frac{\rho(300\,\mathrm{K})}{\rho(4\,\mathrm{K})} = 2.2$

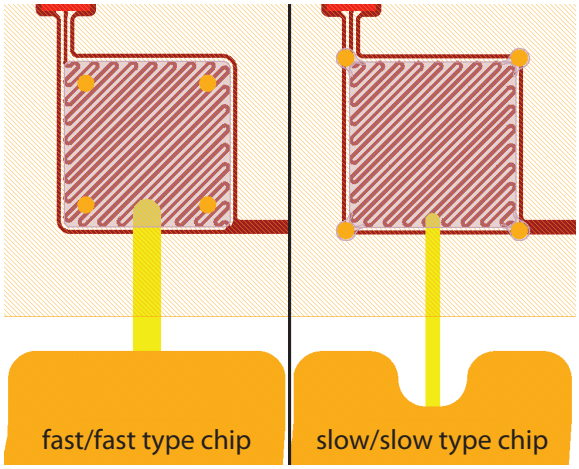

Figure 4.3: Close-up of pixels from two chips with different thermal links. Both the location of the stems (orange circles) and the geometry of the gold thermal links (yellow) to the heat bath (bottom) differ. The pixel on the left produces pulses with faster rise times and faster decay times compared to the pixel on the right.

Temperature	**fast τ_0**	**slow τ_0**	**fast τ_1**	**slow τ_1**
15 mK	467 ns	24 µs	2.72 ms	7.57 ms
41 mK	171 ns	24 µs	1.44 ms	3.35 ms
50 mK	140 ns	24 µs	1.15 ms	2.48 ms
85 mK	82 ns	24 µs	0.50 ms	0.84 ms
120 mK	58 ns	24 µs	0.26 ms	0.37 ms

Table 4.3: Expected signal rise times τ_0 and decay times τ_1 for different Quasy-maXs chips at different temperatures based on calculations in this section.

for our sputter-deposited gold (5N). Since $\rho(300\,\mathrm{K})$ is the sum of the resistivity ρ_{ph} from phonons and ρ_{def} from defects, we find $\rho(4\,\mathrm{K}) = \rho_{\mathrm{def}} = \rho_{\mathrm{ph}}(300\,\mathrm{K})/(RRR - 1)$, with $\rho_{\mathrm{ph}}(300\,\mathrm{K})$ being the resistivity of gold with low defect concentration as listed in tables of material properties. The thermal conductance of the strips at 85 mK are $6.8\,\frac{\mathrm{nW}}{\mathrm{K}}$ and $2.4\,\frac{\mathrm{nW}}{\mathrm{K}}$ for the fast and slow versions, respectively.

We must also take into account the phononic thermalization of the sensor downward into the chip substrate. This path is suppressed by the interfacial thermal resistance, also called Kapitza resistance [Pol69]. For similar geometries, measurements have found thermal conductivities of $G_{\mathrm{K}}(T) = 435\,\frac{\mathrm{W}}{\mathrm{K}^4\mathrm{m}^2} A T^3$ for a contact area A [Hen17]. For $T = 85\,\mathrm{mK}$ and $A = (120\,\mu\mathrm{m})^2$, we find $G_{\mathrm{K}} = 3.5\,\frac{\mathrm{nW}}{\mathrm{m}}$. The decay time then is

$$\tau_1(T) = \frac{C_{\mathrm{s}}(T) + C_{\mathrm{a}}(T)}{G_{\mathrm{strip}}(T) + G_{\mathrm{K}}(T)} \quad . \tag{4.4}$$

We calculate the heat capacity of the sensor using the simulations in section 3.2 and find the time constants appearing in table 4.3.

For applications at $T \lesssim 30\,\mathrm{mK}$, we have the option of placing gold bonds on the four spacious square areas of the galvanized thermalization structures (see figure 4.2). This adds a thermal link via electrons to a detector platform made of bulk copper, which keeps the chip cold at low temperatures and high photon rates. In such a case, the purely phononic link through the bottom of the silicon substrate and the glue to the experimental platform may not suffice, due to the low number of phonons and the Kapitza resistances at low temperatures. Such a design has proven effective in previous set-ups [Sch21, Man21].

Rise Time. Regarding the rise time, either the thermal link between the absorber and the sensor, or between the electron system and the spin system may dominate. For chips with fast rise time, the former is defined by the stems that sit directly on top of the sensor. Repeating the calculation above for stems with radius $r_{\mathrm{stem}} = 6\,\mu\mathrm{m}$,

height $h_{\mathrm{stem}} = 5\,\mu\mathrm{m}$, and $RRR = 12.6$, as measured for our electroplated gold, we find $\frac{C_{\mathrm{a}}}{G_{\mathrm{stem}}} = 23\,\mathrm{ns}$ at $T = 85\,\mathrm{mK}$. This value lies significantly lower than the characteristic time constant $\tau_{\mathrm{K}}(T = 85\,\mathrm{mK}) \approx 80\,\mathrm{ns}$, which we expect from the Korringa relation $\tau_{\mathrm{K}} T = K$. Here, $K = 7\,\mathrm{ns\,K}$ for erbium ions in gold [Ens00]. We thus assume that for these chips, the relaxation of the magnetic moments dominates the pulse shape and $\tau_0 = \tau_{\mathrm{K}}(T)$.

For chips with slow rise times, the stems sit slightly outside the main sensor area. Here, a 11 µm wide thermal bottleneck with an estimated length of 6 µm in the 446 nm thick sensor layer defines the rise time. An analogous calculation to above leads to $\tau_0 = 24\,\mu\mathrm{s} \gg \tau_{\mathrm{K}}$ at $T = 85\,\mathrm{mK}$. This value is almost temperature independent, since to first order, both the thermal conductivity and C_{a} rise linearly with T. Rise times for other temperatures appear in table 4.3.

4.2.3 PIXE Set-up

In order to operate an MMC under the restrictions given by PIXE, we have developed a new experimental platform. A digital render of the new platform appears in figure 4.4. The base is a 16 mm × 17 mm × 1.5 mm piece of copper (1) with clipped corners to make an octagonal shape. Four 1.5 mm high copper pillars (2) act as spacers for the X-ray optics (not shown), allowing us to reliably control the distance between absorber and lens. In order for this distance to be as low as possible, the Quasy-maXs chip (3) sits centrally on a 1 mm high pedestal (4). This design allows the bonding wires leading to the detector to protrude by a minimal amount above the top edge of the Quasy-maXs chip and not come into contact with the optics. Alignment orthogonal to the beam axis is possible via a mechanism at the bottom of the copper holder.

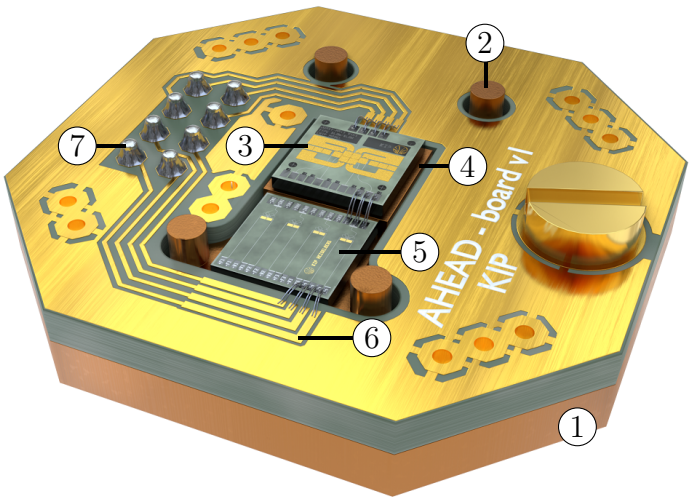

Figure 4.4: Digital render of the end of the detector arm in the PIXE set-up. Mounted on a copper platform in the center is a Quasy-maXs chip. We read out only the rightmost of the four possible channels using a front-end SQUID chip mounted below.

We keep the set-up as compact as possible, by reading out only one channel, which is sufficient for the given application. In figure 4.4, we have connected the right asymmetric channel, with appropriate aluminum bonding wires leading to the front-end SQUID chip (5). The bonding pad layout of Quasy-maXs is chosen to precisely mirror the bonding pad layout of our front-end SQUID chips. As a result, we can easily read out one of the other three Quasy-maXs channels, by placing bonding wires to one of the other three front-end SQUIDs on the SQUID chip. The SQUIDs themselves are connected to gold lines (6) on the dedicated circuit board. The signal path continues to the bottom four pins of an 8-pin plug[5] (7) and from there to a SQUID array module (not shown) [Stä20]. The top four pins contain the heater and field lines and are required for persistent current injection. Via the circuit board, the lines reach the top edge of the Quasy-maXs chip, where we connect them to the chip with bonding wires.

4.3 Characterization of Quasy-maXs

Before permanently installing Quasy-maXs into the PIXE cryostat in Portugal, we perform characterization measurements and test for the functionality of the detector. We carry out these measurements in a dry dilution refrigerator[6], which can reach temperatures of under 10 mK. Since the PIXE set-up described above is only compatible with the matching detector arm, which is already installed in the high resolution high energy PIXE laboratory in Lisbon, we use the experimental platform designed for Hot-maXs (see section 5.2). It is similar in the sense that the detector is mounted on a copper platform in close vicinity to the front-end SQUID chip, but has the advantage of allowing for read-out of all four channels at once.

4.3.1 Persistent Current

In order to operate Quasy-maXs, we inject a persistent current into the pick-up coils. A dedicated current source[7] controlled by the software *AutoFreeze*[8] automatically applies heater and field currents according to the steps we detail in section 2.4. We verify the success of this procedure using a magnetization measurement: If there is a persistent current $I_0 \neq 0$, the sensor material experiences a magnetic field B, and the output voltage δV reflects the temperature dependence of $M(T)$. To first order, the linear relation $\delta V(T) \propto M(T) \propto B \propto I_0$ holds, which our simulations

[5] Cut from an SLR 2 050 G header by Fischer Elektronik GmbH & Co. KG. Nottebohmstraße 28, 58511 Lüdenscheid, Germany.

[6] BF-LD250 from BlueFors Cryogenics Oy, Arinatie 10, 00370 Helsinki, Finland.

[7] CSE-1 by Magnicon, Magnicon GmbH, Barkhausenweg 11, 22339 Hamburg, Germany.

[8] Developed by Marvin Friedrich, unpublished.

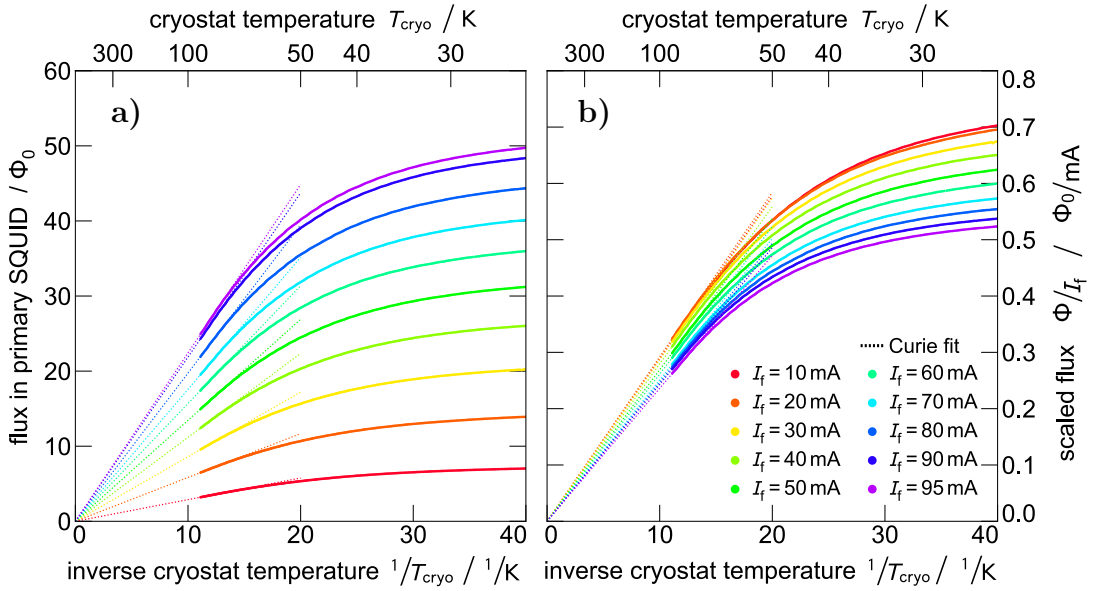

Figure 4.5: a) Measured magnetization curves in units of magnetic flux in the front-end SQUID for different field currents I_f. Dashed lines represent Curie fits to high temperature data. **b)** The same data, scaled by I_f.

confirm for $T \gtrsim 60\,\mathrm{mK}$. Below this temperature, interaction and saturation effects influence the shape of the $M(T)$ curve (see figure 3.4). The high temperature slope of a magnetization curve is thus a measure for I_0.

Of interest is the dependence of the persistent current I_0 on the field current I_f, as well as the heater current I_h and heating time t_h (see section 2.4). Our experiments show that above a critical value of 2.8 mA, varying heat current I_h does not change the injected current I_0. We also do not observe a dependence on the heating time t_h down to the shortest available value of $t_h = 10\,\mu\mathrm{s}$. We have previously reported such behavior for a different experiment [Her18].

Varying the field current I_f yields unexpected results. In figure 4.5 a) appear the magnetization curves for $I_f = 10\,\mathrm{mA}$ to $I_f = 95\,\mathrm{mA}$, the latter being the maximal applicable current before superconductivity breaks. Dashed lines represent Curie fits to the data at $T \geq 80\,\mathrm{mK}$. These fits determine the y-offset of the data. While the persistent current I_0 does increase with field current I_f, the relation is not linear, as the scaled plot in figure 4.5 b) shows. The scaled Curie fits have different slopes, and data for low I_f lie above data with high I_f. Our conclusion is that not the entirety of the field current converts into persistent current during the injection. Assuming $I_0 \approx I_f$ at $I_f = 10\,\mathrm{mA}$, we find a persistent current of $I_0 = 68\,\mathrm{mA}$ for a field current of $I_f = 95\,\mathrm{mA}$. The reason for this behavior is not quite clear. We are not limited by a short section of the pick-up coil with critical current of 68 mA, since

we do not observe heating when applying up to $I_f = 95\,\mathrm{mA}$. Also, according to our simulations, the different magnetic field in the sensor at different persistent current I_0 does not alter the magnetization curve in the observed fashion. Instead, the problem seems to be with the PCS itself, which we have slightly redesigned with narrower lines and smaller margins compared to previous detectors. Further measurements with an expanded temperature range, in particular improved thermalization at lower temperatures, would illuminate the situation.

For the experiments discussed below, we use parameters of $I_h = 3.0, \mathrm{mA}$, $t_h = 10\,\mu\mathrm{s}$, and $I_f = 95\,\mathrm{mA}$, which provides a maximal persistent current, while keeping cryostat warming during the preparation of the current to a minimum.

4.3.2 Thermalization

The magnetization curves in figure 4.5 are plotted as functions of the temperature of the experimental platform of the cryostat. Note that this is not necessarily the temperature of the experiment, since the thermal link to the experimental platform of the cryostat is finite. Heating, mainly from the front-end SQUIDs, can cause the experiment to thermally decouple at low temperatures.

A comparison between experiment and simulation appears in figure 4.6. We inject a current as described above, and measure the magnetization between $T_{cryo} = 10\,\mathrm{mK}$ and $T_{cryo} = 800\,\mathrm{mK}$, while making sure that we vary the cryostat temperature slowly enough for the experiment to be in thermal equilibrium. For data plotted in red, all four front-end SQUIDs are enabled, while for data in blue, only one SQUID is active, which we use to perform the measurement. At high temperatures, data match

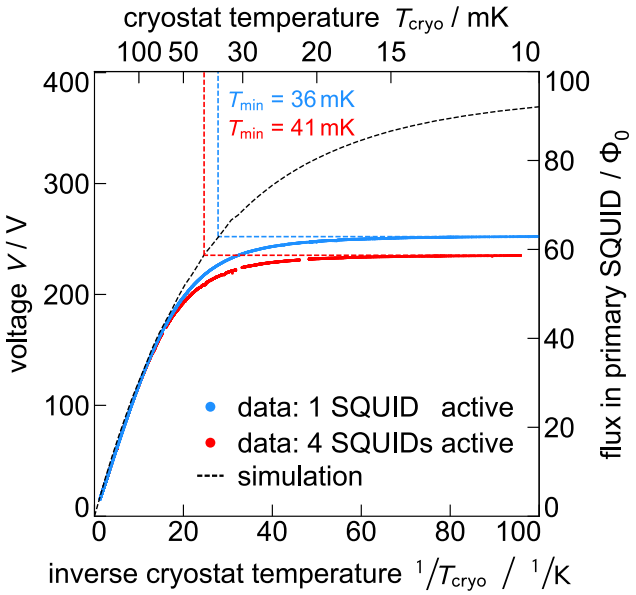

Figure 4.6: Thermalization measurement when one SQUID is active (blue) and when four SQUIDs are active (red). From a comparison with simulations (black dashed line), we find the respective minimal experiment temperatures T_{min}.

a simulation with $I_0 = 68\,\mathrm{mA}$ well, reaffirming our hypothesis that only 68 mA are injected. Below $T_{\mathrm{cryo}} = 60\,\mathrm{mK}$, the temperature of the experiment exceeds that of the cryostat. The difference in the two data sets indicates that heating from the SQUIDs is responsible. At lowest temperatures, we project data onto the simulated curve to find minimal temperatures of $T_{\mathrm{min}} = 41\,\mathrm{mK}$ and $T_{\mathrm{min}} = 36\,\mathrm{mK}$, respectively. We conclude that the experimental set-up is well suited to support measurements at temperatures of 85 mK, which are relevant for Quasy-maXs.

4.3.3 Pulse Shape

As we discuss in section 2.7, the pulse shape influences the performance of the detector. With Quasy-maXs, we have the option of altering the pulse shape by choosing the chip type. We demonstrate this in figure 4.7, where we show the response of a fast/fast and slow/slow-type chip upon the impact of a 5.9 keV X-ray photon. As expected, both the signal rise time and the signal decay time are affected. This is true for data on the left of figure 4.7, taken at the chip's base temperature of 41 mK (see figure 4.6), and for data on the right, taken at the operating temperature of the PIXE cryostat of 85 mK.

While according to equation (2.19) the pulse shape of an MMC can theoretically be described by an exponential rise followed by an exponential decay, such a shape does not fit our data. Instead, the fit appearing in figure 4.7 is based on double

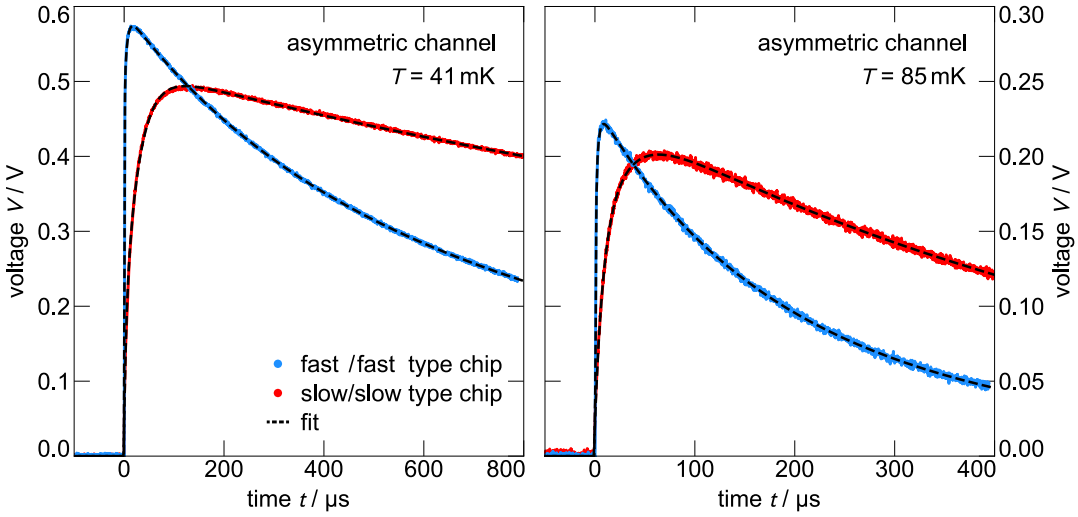

Figure 4.7: Pulse shape of a fast/fast-type chip (blue) and a slow/slow-type chip (red) after the impact of a 5.9 keV X-ray photon. A fit consisting of four exponentials describes the data well. Pulses at lowest temperatures appear on the left, and pulses at PIXE operating temperature, $T = 85\,\mathrm{mK}$ on the right.

chip	T	a_0	$\tau_{0,1}/\mu s$	$\tau_{0,2}/\mu s$	a_1	$\tau_{1,1}/\mu s$	$\tau_{1,2}/\mu s$
fast/fast	41 mK	0.81	0.49	5.4	0.69	1300	316
slow/slow	41 mK	0.69	29	4.1	0.66	5500	1500
fast/fast	85 mK	0.67	0.48	2.6	0.51	142	364
slow/slow	85 mK	0.51	24	7.2	1.00	612	–

Table 4.4: Fit parameters describing the pulse shape of Quasy-maXs according to equation (4.5).

exponentials and has the form

$$p(t) = \Theta(t-t_0)\,A \cdot \Big(a_1\, e^{-(t-t_0)/\tau_{1,1}} + (1-a_1)\, e^{-(t-t_0)/\tau_{1,2}} - a_0\, e^{-(t-t_0)/\tau_{0,1}} - (1-a_0)\, e^{-(t-t_0)/\tau_{0,2}}\Big) \quad . \tag{4.5}$$

Here, $\Theta(\cdot)$ is the Heaviside step function and t_0 is the start time of the signal, which we set to 0 in figure 4.7. Both signal rise and decay consist of two exponential functions weighed by factors a_0 and a_1. Fit parameters for the four displayed pulses appear in table 4.4.

The dominant rise time of the slow/slow-type chip matches our design value of 24 µs. For the fast/fast-type chip, however, we do not reach the values predicted by the Korringa-relation, which lie 2–5 times lower and are temperature dependent. We are also not limited by the SQUID electronics, which would allow for a factor of ~ 3 shorter rise times. Instead, the temperature independence suggests a limiting thermal link, similar to the Au:Er bottleneck for slow/slow type chips. We suspect that the sensor layer itself might form such a bottleneck, as pictured in figure 4.8 a): With the niobium layer being $\sim 8\,\%$ thicker and the sensor layer 11 % thinner than designed, the height difference between these two layers is only 177 nm. On the edge of a niobium line, there might be only a narrow section connecting Au:Er lying between niobium lines to Au:Er lying on top of a line. A Au:Er thermal link with a characteristic width of a_s, a height of 177 nm, and a length of $p/10$ would produce a signal rise time of 0.47 µs.

Regarding the decay times at 85 mK, our measured values lie below the values of 500 µs and 840 µs we projected in table 4.3 for the fast/fast and slow/slow-type chips, respectively. Figure 4.8 b) shows an image taken with a scanning electron microscope, which reveals that absorbers have collapsed and are contacting the thermal link between sensor and thermal bath. Since there is no insulating layer between thermalization and absorber, this creates a thermal path, short-cutting a section of the full thermal link marked by dashed lines. Projecting the footprint of the absorber down onto the thermal link, we find that for fast/fast type chips, the effective length

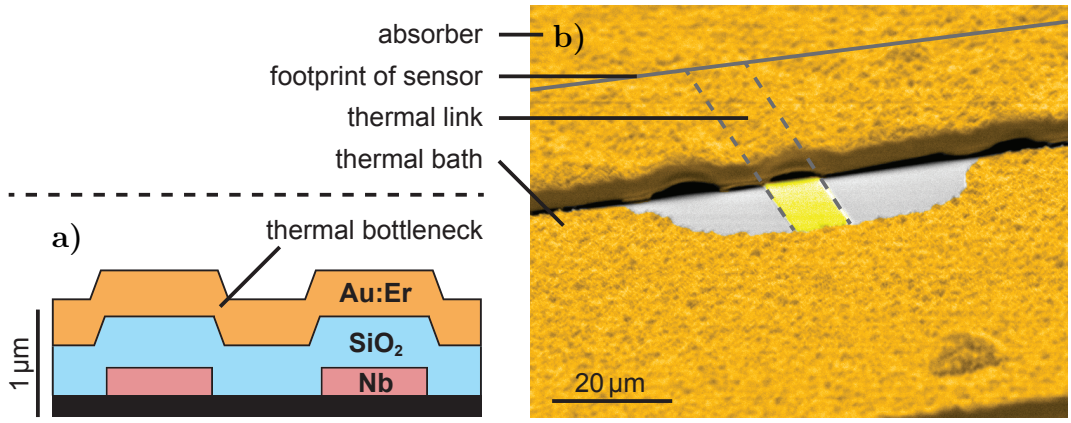

Figure 4.8: a) Cross-section of the pick-up coil, illustrating a thermal bottleneck in the sensor layer. For clarity, height of layers is stretched by a factor of 5. **b)** SEM image of an absorber contacting the thermal link to the thermal bath.

of the thermal link is reduced from 90 µm to 25 µm, and for slow/slow type chips from 135 µm to 65 µm. Using these new values, we find decay times of 193 µs and 619 µs, which are consistent with our measurements.

At low temperatures, the collapsed absorbers change the expected decay times to 440 µs and 1.97 ms, which match decay times we observe. There is, however, a significant contribution from an additional long thermalization time, which may be due to lacking thermalization of the large thermal bath surrounding the pixels. Adding gold bonds to an off-chip location will likely remove this component.

4.3.4 Noise Spectrum

An important indicator of the quality of the experimental set-up is the noise spectrum. Here, we present the noise spectrum of Quasy-maXs in figure 4.9 for $I_0 = 0\,\mathrm{mA}$ and $I_0 = 68\,\mathrm{mA}$ taken at the base temperature of the cryostat. At high frequencies, we observe a plateau. Towards low frequencies, the measurement for $I_0 = 0\,\mathrm{mA}$ increases steadily, while we see an additional shoulder in the $I_0 = 68\,\mathrm{mA}$ data.

Five different noise components appear in various dotted and dashed lines. Their squared sum makes up the solid gray line, which is a remarkable match to the measured $I_0 = 68\,\mathrm{mA}$ data. When summing up all noise components except for the energy fluctuations, we obtain the solid black line, which matches the $I_0 = 0\,\mathrm{mA}$ data well. Note that these lines are not fit to our data, but instead the direct result of simulations and measurements using secondary experiments. We give a quick summary of each component:

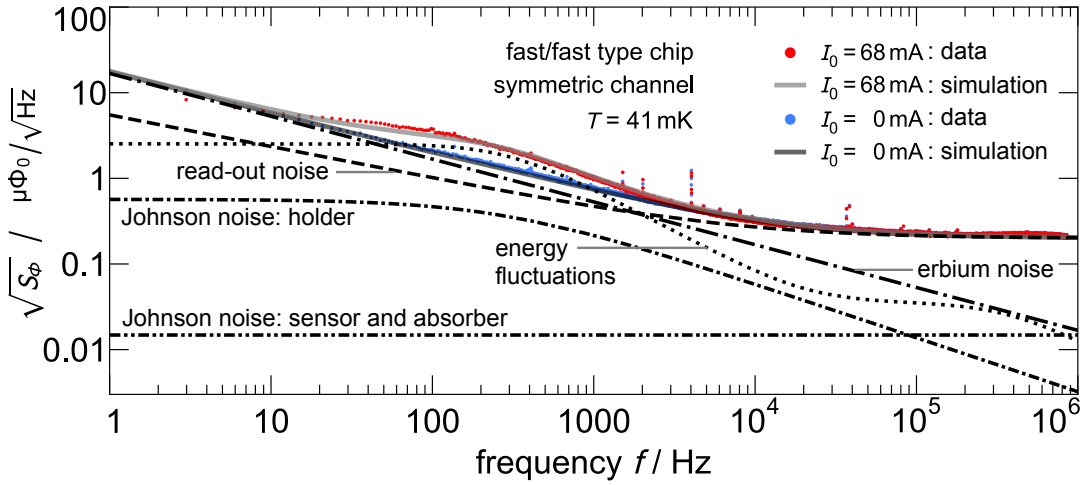

Figure 4.9: Noise spectrum of a symmetric channel on a fast/fast-type Quasy-maXs chip at 41 mK. Data for $I_0 = 68\,\mathrm{mA}$ appear in red and data for $I_0 = 0\,\mathrm{mA}$ in blue. The sum of different simulated noise contributions are the solid gray and black lines.

- Noise from **energy fluctuations** (see section 6.5) only contributes, if there is persistent current in the pick-up coils, since it originates from the detector's response upon particle impact. The theoretical description in equation (6.14) only allows for signal shapes described by two single exponentials. As an approximation, we have chosen only the dominant time constants measured in the previous subsection. This could be the cause for a slight deviation to our measured data in the region of 10 – 1000 Hz.

- The displayed **erbium noise** contribution (see section 6.4) is the result of measurements of the complex susceptibility of Au:Er. We present this analysis in subsection 7.4.2.

- The **read-out noise** (see section 6.2) is the sum of various noise sources in the read-out chain (see subsection 7.1.1) and varies when exchanging SQUID chips. The displayed contribution comes from a previous cryostat run using the same front-end SQUID and SQUID array.

- We measured various **Johnson noise** components (see section 6.3) using cross-correlated read-out of a dedicated noise measurement device. Measurements of noise from the experimental holder are available in subsection 7.4.4, and from the sensor in subsection 7.4.3. We have not explicitly measured noise from the absorbers, but since the physics is identical to Johnson noise from the sensor, we feel confident that the corresponding predictions are robust.

The accurate description of the noise of an MMC is a central accomplishment of this thesis. It is a result of our new software package for simulations, a clean experimental set-up, and dedicated noise measurements of the individual contributions. Our data show that Quasy-maXs is working as intended without unexpected outside noise sources, and that we have a good understanding of the involved principles.

4.3.5 Energy Resolution

The ultimate metric of Quasy-maXs is the energy resolution for X-rays in the keV range. We experimentally determine this value by illuminating our detector with an ^{55}Fe source. This isotope undergoes electron capture with a half-life of 2.74 years. The resulting ^{55}Mn is typically in an excited state and de-excites via the emission of Auger electrons and X-ray photons. While the former are stopped by a beryllium window enclosing the source, the latter reach Quasy-maXs absorbers after passing through a collimator. The theoretical spectrum is dominated by peaks at 5.9 keV and 6.5 keV, which correspond to the K_α and K_β lines respectively, with a number of lines from minor transitions widening the peaks. Most important is fine-structure splitting into $K_{\alpha1}$ and $K_{\alpha2}$ of the K_α line, which is in the order of 12 eV [Höl97].

In an initial characterization, we record ~ 5000 events per pixel of a fast/fast-type chip at base temperature with a rate of ~ 0.1 Bq per pixel. SQUIDs are controlled by a Magnicon XXF-1 SQUID Electronics[9], whose output we digitize via a 16-channel, 16bit SIS3316 digitizer card[10]. Data acquisition occurs via the program *PAQS*[11] [Hen17] and data evaluation via the software package *darq*[12] [Bar23]. We perform a template fit to the pulses [Ham21], then apply time information cuts [Ham21] and a χ^2 cut. There follows a temperature correction [Ung20] and finally an energy calibration, in which we translate the measured amplitude into an energy scale.

For an asymmetric channel, a histogram of the resulting energies in the region of the K_α-line appears on the left hand side of figure 4.10. The fine-structure splitting is clearly visible and is emphasized by the dashed line, which is the natural line shape. A convolution (solid line) of the natural shape and a Gaussian results in a fit matching the histogram of our data and we find $\Delta E_{\mathrm{FWHM}} = (7.8 \pm 0.1)$ eV. In order to find the intrinsic energy resolution, it is also useful to apply the same algorithms to so-called baselines, which are time traces without a pulse. The corresponding histogram appears on the right hand side of figure 4.10. A Gaussian describes our data well and we find a baseline energy resolution of $\Delta E_{\mathrm{FWHM}} = (5.2 \pm 0.2)$ eV. This

[9] Magnicon GmbH, Barkhausenweg 11, 22339 Hamburg, Germany.

[10] Struck Innovative Systeme GmbH, Harksheider Str. 102, 22399 Hamburg, Germany.

[11] **P**arallel data **ac**q**u**isition **s**ystem, developed by Daniel Hengstler.

[12] **D**ata **a**nalysis and **r**eduction for **q**uantum sensors, developed by Arnulf Barth and Robert Hammann.

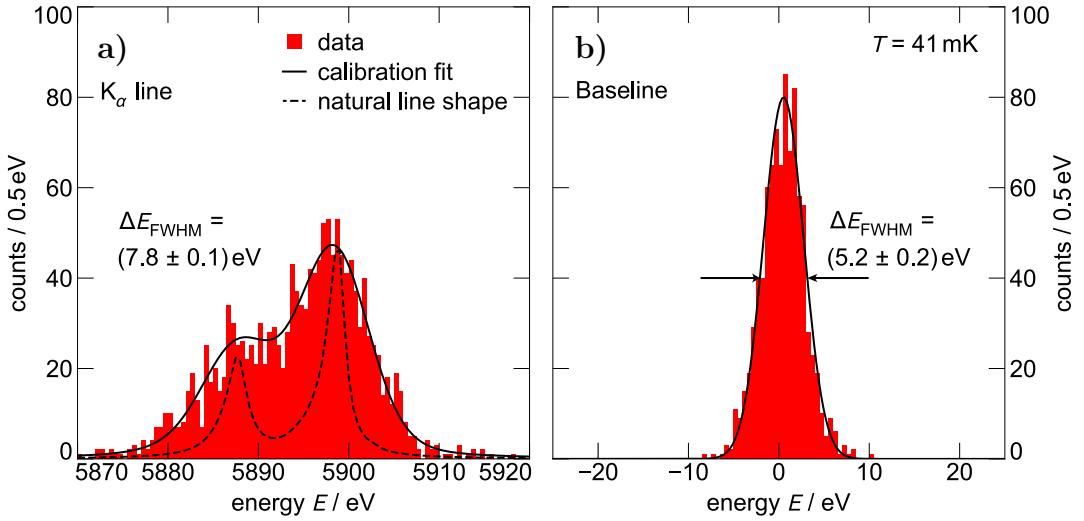

Figure 4.10: a) Histogram of the K_α line of a ^{55}Fe source as measured with an asymmetric channel of a fast/fast-type Quasy-maXs chip at $T = 41\,\mathrm{mK}$. Data (red) is fit by a convolution (solid line) of a Gaussian with 7.8 eV FWHM and the natural line shape (dashed line). **b)** Baseline histogram of the same channel fit by a Gaussian.

lies only slightly above the simulated value of 4.5 eV we expect for an asymmetric channel of a fast/fast-type chip at 41 mK.

We perform the same analysis for pixels of symmetric channels, and for slow/slow-type chips, where we always used temperature information from an asymmetric channel for temperature correction. The results appear in table 4.5, where we also list the energy resolution at 85 mK. We observe a general trend that symmetric channels have a $\sim 50\,\%$ worse energy resolution than asymmetric channels. This matches the expected effect of the differing magnetic flux coupling from the pick-up coil to the front-end SQUID, which we calculate to be 0.057 for symmetric channels and 0.087 for asymmetric channels. Our data thus demonstrates that the asymmetric design improves energy resolution as intended. Note that this effect is stronger at higher temperatures, since fluctuations of the chip temperature, which are especially impactful at low temperatures, degrade the performance of asymmetric channels slightly. For PIXE applications at 85 mK, we thus suggest using asymmetric channels.

A less pronounced effect is the difference between fast/fast-type chips and slow/slow-type chips. Our data suggest that the former slightly outperforms the latter. This is understandable when consulting equation (2.25), which states that $\Delta E \propto (\tau_0/\tau_1)^{1/4}$. Our measurements of the pulse shape show that this fraction is lower for fast/fast-type chips. Following this theory, fast/slow-type chips should have an even better energy resolution, but we have not yet tested this chip type in a cryostat. In practice, requirements from the detector's application can have a larger impact than the slight

chip type	channel type	Baseline 41 mK	K_α-line 41 mK	Baseline 85 mK	K_α-line 85 mK
fast/fast	asymmetric	5.23 eV	7.76 eV	14.5 eV	19.0 eV
slow/slow	asymmetric	5.52 eV	10.2 eV	18.8 eV	19.7 eV
fast/fast	symmetric	7.59 eV	10.7 eV	29.6 eV	28.9 eV
slow/slow	symmetric	no data	8.73 eV	33.0 eV	29.3 eV

Table 4.5: Measured energy resolution of different chip and channel types.

difference in energy resolution. For PIXE spectroscopy, for instance, the goal of a high count rate makes fast/fast-type chips more attractive than fast/slow-type chips.

4.4 Future Improvements

In this chapter we have presented a first generation MMC designed for PIXE spectroscopy. Based on our characterization measurements, we have found that best suited for PIXE is an asymmetric channel on a fast/fast-type chip. At 85 mK, we measured an energy resolution of 19.0 eV at 5.9 keV, which corresponds to a resolving power of over $E/\Delta E = 300$. With this value, our first generation Quasy-maXs chip already outperforms the transition edge sensor previously used in the PIXE set-up in Lisbon (15 eV at 1.5 keV, 40 eV at 10.6 keV [Cha14]). We have thus demonstrated that MMCs can represent a true upgrade, with the next immediate step being the implementation of Quasy-maXs in the high resolution high energy PIXE laboratory in Lisbon in mid 2023.

Our characterization measurements have also shown that a number of improvements for a second generation chip are possible. In the following, we list the most important points, where we consider the performance of Quasy-maXs in a PIXE setting, that is an asymmetric channel on a fast/fast-type chip at 85 mK.

- A sensor made of **enriched erbium** would improve performance. Our simulations show that without the additional heat capacity originating from the hyperfine splitting, the energy resolution would be 16 % better. Additional improvements due to a steeper $\partial M/\partial T$ curve are likely in the order of a few percent.

- Our current injection tests show that the maximal **persistent current** is only 68 % of the optimal value, leading to a degrading of the energy resolution by 13 %. The problem seems to be the persistent current switch or the freezing procedure itself, and may be caused by a slight redesign of the PCS. A simple

fix would be to copy the design of a previously proven persistent current switch from a different detector.

- Preventing the collapse of absorbers by optimizing stem size and placement would lead to more consistent and overall longer **decay times**. According to our simulations, a fast/fast-type chip at 85 mK with the designed decay time of 500 µs instead of the measured decay time of 190 µs has a 15 % better energy resolution. Such a change must be in accordance with the count rate requirements for PIXE.

- A similar fix of the **rise time**, which we believe is limited by the thermalization within the sensor material, could be achieved by a slightly thinner Nb1 layer, a slightly thicker sensor layer, and additional stems. While this would have a positive effect on the response function, the corresponding noise from energy fluctuations lies in a region that is dominated by read-out noise. As a result, such a fix would not improve the noise of the device noticeably and the potential gain in energy resolution is only around 1.5 %.

- The insulating **SiO_2 layer** between the sensor and underlying pick-up coil ended up 31 % thicker than expected. As a result, the sensor material experiences less magnetic field, and changes of the magnetic flux couple less strongly into the pick-up coil. The estimated loss in energy resolution is 6 %.

From our simulations, we find that implementing all of the changes above would improve the theoretically possible energy resolution of Quasy-maXs in a PIXE environment from 11.3 eV to 6.6 eV. As a result, we feel confident that a second generation Quasy-maXs detector operated at 85 mK can achieve an energy resolution of under 10 eV and a resolving power of over 500 at a photon energy of 6 keV.

5. Hot-maXs - an MMC Operated at 300 mK

In the previous chapter we presented a detector, which pushes the limits of the typical MMC design in terms of operating temperature. Quasy-maXs is a device meant to work in an environment that is atypical, but still reasonable for an MMC. In this chapter, we go one step further. The ***H**igh **O**perating **T**emperature **MMC** **A**rray for **X**-ray **S**pectroscopy* (Hot-maXs) takes the concept of an MMC to its extreme, trying to achieve the highest possible operating temperature that is still compatible with the basic principle of magnetic micro-calorimetry. While Quasy-maXs is primarily designed to have immediate and specific applicability, Hot-maXs is a proof-of-principle detector. The goal is not to achieve the best possible energy resolution, the largest detection area, or the highest number of pixels, but to demonstrate that operating temperatures of hundreds of millikelvin are feasible. To this end, we rethink key aspects of an MMC regarding materials and design (section 5.1), and fabrication (section 5.2). We demonstrate the functionality of Hot-maXs in section 5.3 and discuss future steps in section 5.4.

5.1 Designing Hot-maXs

A digital render of the Hot-maXs chip appears in figure 5.1. While the appearance of Quasy-maXs is dominated by gold structures, we forgo this material entirely, due to the high electronic heat capacity. The eight absorbers instead consist of macroscopic $1\,\mathrm{mm}^2$-sized cuboids of superconducting lead, which we mill from bulk material using a small, fast spinning CNC mill. The substrate is a large $6\,\mathrm{mm} \times 4\,\mathrm{mm} \times 0.5\,\mathrm{mm}$ piece of transparent fused silica and dedicated thermalization structures are omitted entirely. In the following, we discuss design choices and present the chip in detail.

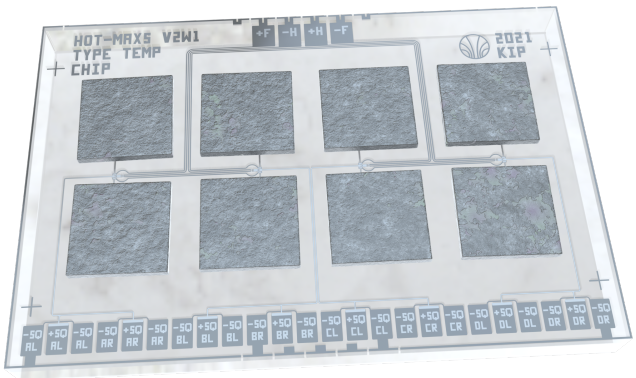

Figure 5.1: Digital render of a Hot-maXs chip, designed to perform metallic magnetic calorimetry at the highest possible temperatures.

5.1.1 Sensor Material

The main challenge with operating MMCs at high temperatures is the temperature dependence of the sensor material's magnetization, which is significantly flatter at high T. In figure 5.2, we use the simulations we present in section 3.2 to plot $\partial M/\partial T\,(T)$ of Au:Er normalized with the erbium concentration for a typical magnetic field of 8 mT. For $x_{\mathrm{Er}} = 400$ ppm, $\partial M/\partial T$ is 40 times lower at 200 mK than at 20 mK. In order to nevertheless have a measurable signal, we must increase the total number of erbium ions. There are two ways to do this: either by increasing the erbium concentration, or by increasing the sensor volume.

Increasing erbium concentration. If erbium ions are packed closer together, stronger erbium-erbium interactions occur in the sensor, decreasing the magnetization. However, the reduced paramagnetism shows itself mainly by a saturation of $M(T)$ at low temperatures [Her22], leaving the high temperature magnetization largely unaffected. As an example, we see in figure 5.2 that at 20 mK, increasing the concentration from 400 ppm to 3200 ppm decreases the scaled $\partial M/\partial T$ by a factor of three. At $T = 200$ mK on the other hand, the difference is only 25 %. We are thus able to pack the erbium ions more densely at high temperatures, without losing much signal to erbium ions being locked in a spin state by the interaction with neighboring erbium ions and thus not contributing to the magnetization.

Increasing sensor volume. If we implement the volume increase with a larger sensor footprint A_{sens}, the inductance of the meander coil $L_{\mathrm{m}} \propto A_{\mathrm{sens}}$ is larger.

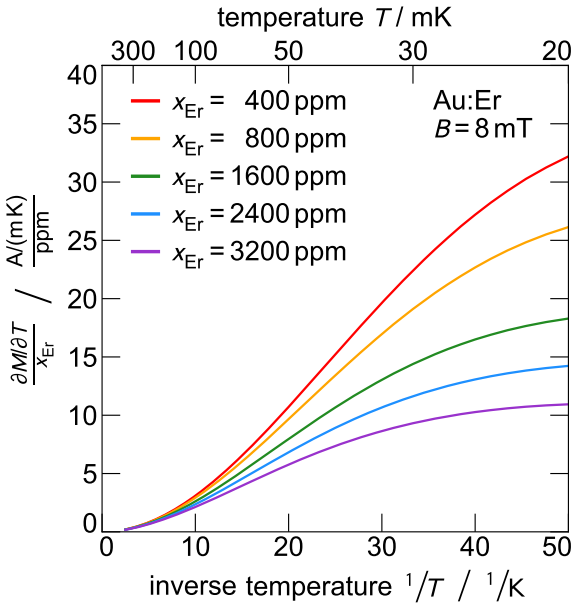

Figure 5.2: Simulated temperature dependence of the slope of $M(T)$ in a field of 8 mT for Au:Er. The curves of the five different alloys are scaled by their erbium concentration x_{Er}.

According to equation (2.14), this decreases the flux coupling to the front-end SQUID and would ideally require SQUIDs with adjusted input inductances $L_\mathrm{i} = L_\mathrm{m}/2$. While such devices are not available to us at the moment, SQUIDs with an input inductance of $\sim 6\,\mathrm{nH}$ are currently under development [Kah23, Krä23] and may find application in the future. However, even for matched input coil inductance, the coupling to the SQUID would decrease with $\sqrt{L_\mathrm{m}}$. If we instead increase the sensor's volume by increasing its height, magnetic coupling between sensor and pick-up coil is worse, which we best express via the average $\langle G^2 \rangle$ of the square of the position-dependent geometry factor. As an example, consider Au:Er placed on a meander-shaped pick-up coil with a pitch of 6 µm, a line width of 3 µm, a niobium height of 250 nm, and an insulating layer of 350 nm of SiO_2. Using finite element simulations, we find that a sensor with a height of 500 nm and $x_\mathrm{Er} = 3200\,\mathrm{ppm}$ has an average squared geometry factor $\langle G^2 \rangle$ of 0.37. A sensor with $x_\mathrm{Er} = 400\,\mathrm{ppm}$ and the same number of erbium ions has a height of 4 µm, and we find $\langle G^2 \rangle = 0.11$.

We conclude that detrimental effects of increasing the sensor volume are more significant than the 25% penalty in the scaled $\partial M/\partial T$ when adjusting the erbium concentration. An ideal value is reached, before the erbium-erbium interactions cause the Schottky anomaly originating from RKKY interactions to widen too far towards high temperatures. Based on our simulations, we found that a value of $x_\mathrm{Er} \approx 2500\,\mathrm{ppm}$ promises good performance for $100\,\mathrm{mK} \leq T \leq 300\,\mathrm{mK}$.

5.1.2 Absorber

Since an MMC measures the temperature change caused by a particle impact, the heat capacity of the absorber is an important quantity to consider. In fact, we have shown in equation (2.25) that energy resolution scales with the square root of heat capacity. As an example, we compare two absorbers, where one is made of gold and the other made of superconducting lead. Each has a detection area of $1\,\mathrm{mm}^2$ and an absorption probability of 50 % for a 60 keV photon, leading to the lead absorber being 1.6 times thicker [Hub09]. Their heat capacities appear in figure 5.3 as a function of temperature. While the specific heat of electrons dominates in gold, only the specific heat from phonons is relevant in lead, leading to a significantly lower absorber heat capacity. If operated at 200 mK, a 60 keV X-ray heats up the absorber made of gold by 9 µK, while heating the absorber made of lead by 100 µK. Even when adding the MMC's sensor heat capacity to make a more accurate thermodynamic model, this order in magnitude remains, since we generally optimize the heat capacity of the spin system. This typically leads to matched heat capacities of absorber and sensor [Fle05].

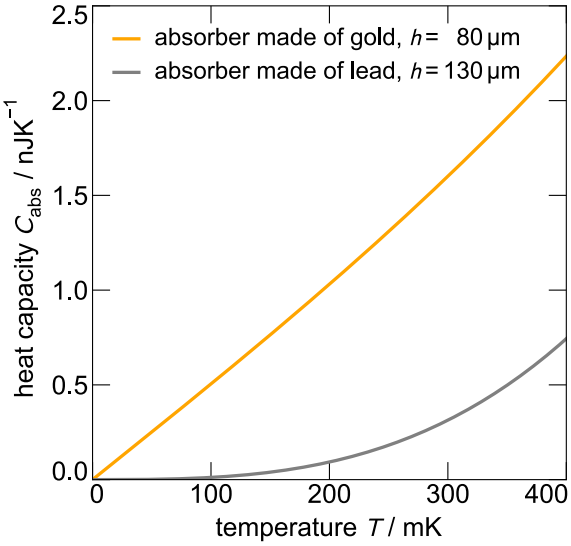

Figure 5.3: Heat capacity of two absorbers with a footprint of 1 mm^2 and a stopping power of 50 % at 60 keV as a function of temperature. The absorber made of gold (orange) has a higher heat capacity than the absorber made of lead (gray).

The main drawback of using a superconductor as an absorbers is energy down-conversion, which is both slow and not fully understood. As a result, we expect it to have a negative impact on the performance of the detector. However, experiments have pointed towards this effect being less detrimental at $T \geq 2 \times 10^{-4}\,\Theta_D$ [Cos93, Wel08], which is compatible with our goal of reaching high temperatures.

In summary, the expected benefits outweigh the negatives and decided to test a superconducting absorber for Hot-maXs. Specifically, we choose lead, due to its large stopping power, high superconducting transition temperature of 7.2 K, and ease of manufacturing. Furthermore, with a comparably low Debye temperature of $\Theta_D = 106\,\mathrm{K}$ [Ste83], the limit of $T \geq 2 \times 10^{-4}\,\Theta_D$ is reached already at 21 mK.

5.1.3 Thermalization

While for Quasy-maXs we specifically designed structures in order to speed up thermalization to a heat bath, we face the opposite challenge for Hot-maXs and must artificially reduce thermalization. The reason is that the rise time τ_0 should be significantly smaller that the decay time τ_1. This is not simple to achieve for Hot-maXs, for two reasons. First, the thermalization time of the superconducting absorber is large, and with it, τ_0. Second, due to the high temperatures, any link to a heat bath is stronger, reducing τ_1. We attempt to tackle this challenge by constructing a thermal bottleneck between sensor and the cryostat in the form of an amorphous chip substrate. In comparison to high-purity crystalline silicon, thermal transport is diffusive and the mean free path of phonons is short.

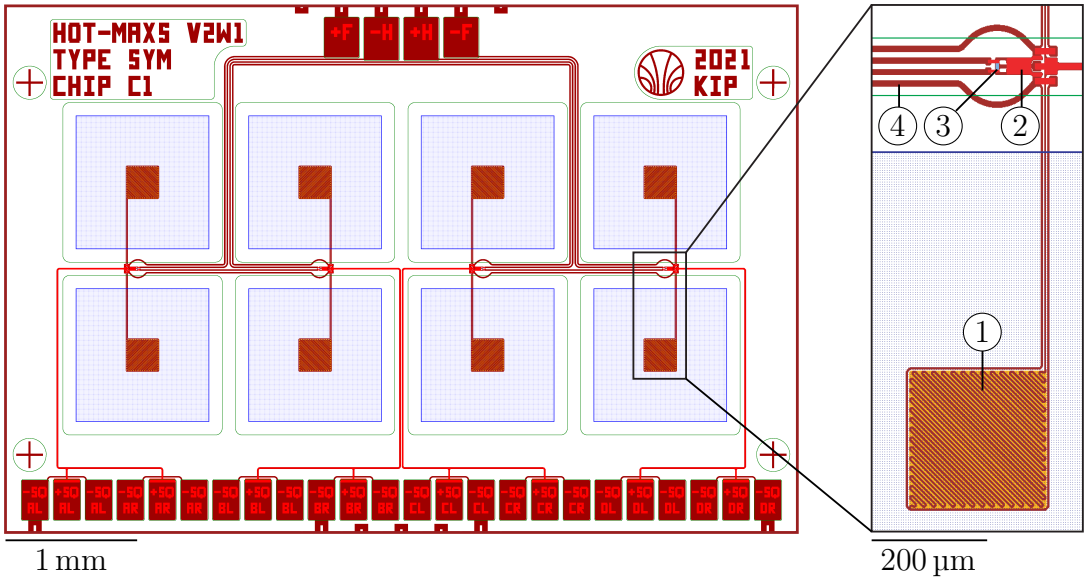

Figure 5.4: Schematic of a Hot-maXs chip, with a close-up of a single channel on the right. Colors of different materials are listed in table 5.1.

5.1.4 The Hot-maXs Chip

Based on the results of the simulation and optimization process, we present here a first prototype Hot-maXs chip, which consists of eight micro-fabricated layers, which we list in table 5.1. The design of the layers appears in figure 5.4, where we depict the entire chip on the left and a close-up section on the right. The chip is based on a $4\,\text{mm} \times 6\,\text{mm} \times 0.5\,\text{mm}$ fused silica substrate and is made up of three distinct parts. These are the eight pixels, the four persistent current switches, and the two sets of bond pads. In the following, we describe these components in detail.

Hot-maXs features four channels side-by-side, each reading out two **pixels**. Central to each pixel is the meander-shaped pick-up coil (1) with a line width of 3 µm and a pitch of 6 µm. With a side length of 240 µm, we use equation (2.10) to calculate the inductance of the pick-up coil to be $L_\text{m} = 2.6\,\text{nH}$. A 560 nm thick film of Au:Er (orange) with $x_\text{Er} = 2490\,\text{ppm}$ covers the pick-up coil. These two components are galvanically decoupled by two 175 nm thick films of SiO_2, which cover almost the entire chip. Blue squares outline the later locations of the lead absorbers, which we center on each Au:Er temperature sensor. Since we apply pressure to the absorbers during the attaching process, only the minimal amount of components lie within these blue squares, to prevent potential damage, especially structures in the second niobium layer. Rounded green squares just outside of the planned locations of the absorbers mark inner edges of a final protective SiO_2 layer, additionally protecting structures fabricated in Nb2.

No.	Name	Material	Height	Color in figure 5.4
1	Nb1	niobium	250 nm	dark red
2	Anodization	niobium oxide	~ 30 nm	not pictured
3	Iso1a	SiO_2	175 nm	not pictured
4	Iso1b	SiO_2	175 nm	not pictured
5	Heater	AuPd	150 nm	blue
6	Nb2	niobium	600 nm	bright red
7	Sensor	Au:Er	560 nm	orange
8	Iso2	SiO_2	175 nm	green

Table 5.1: Overview of the eight micro-fabricated layers of Quasy-maXs. Listed are the materials they are composed of, and the color in which they appear in figure 5.4. Further steps to attach absorbers follow in subsection 5.2.3.

Protected in such a way are the **persistent current switches** (PCSs) (2), of which four identical copies are located along the center of the chip. Each PCS allows us to inject persistent current into the pick-up coils directly above and below itself. At the center of the PCS lies the AuPd heater (3), with heater current flowing through a non-superconducting strip with dimensions of $12\,\mu m \times 5\,\mu m \times 150$ nm. Other parts of the circuitry, such as the field lines (4) and lines to the pick-up coils, have a distance of at least 50 µm from the heater, in order to prevent inadvertent breaking of superconductivity in these sections during current injection.

Going back to the overview image of the chip, two sets of bond pads line the top and bottom edges. The former set allows for direct connection to an outside circuit board (see figure 5.5), through which we supply field and heater current. Note that these currents run through all four PCSs in series, so that we inject current in all four channels at once. Along the bottom is a collection of bond pads, with which we connect the chip to front-end SQUID chips placed next to the Hot-maXs chip. With a width of 6 mm, Hot-maXs is designed to be read-out using two 4-channel, $3\,mm \times 3\,mm$ sized, HDSQ-type front-end SQUID chips placed side-by-side, of which we use 2 channels of each. By offering two sets of bond pads for each Hot-maXs channel, we have a choice of two possible channels on the front-end SQUID to connect to, allowing us to avoid possible SQUID channels with poor performance.

5.2 Experimental Methods

Several experimental methods developed for the Hot-maXs project were used throughout this thesis. Most notable is the high concentration Au:Er target, which we also utilize for the fabrication of Quasy-maXs and which we analyze with the noise-o-

meter. Here, we explain its fabrication. The same is true for the high temperature set-up, which is a versatile detector arm with an exchangeable detector module. Besides the first light of Hot-maXs and the characterization of a number of Quasy-maXs chips, we also use this hardware as part of the copper set-up for the noise-o-meter. This section concludes with a new tool we constructed to accurately diffusion weld lead absorbers onto Hot-maXs.

5.2.1 Au:Er Target Construction

In order to fabricate layers with sub-micron precision, we utilize photo-lithography techniques [Koc20]. This includes a step of depositing material onto a wafer via sputter deposition, which requires a target made of the respective material. For our machines, this is typically a disk with a diameter of 2 inches and a height of 5 mm. For our applications, we require a sensor material with a large erbium concentration, so a key part is the fabrication of an appropriate Au:Er target.

Due to the high price of gold, we construct only a single target in the framework of this thesis, which we base on a pre-existing Au:Er target with an erbium concentration of $x_{\mathrm{Er}} = 775\,\mathrm{ppm}$. The erbium is of natural isotopic composition. Simply adding erbium in a crucible to obtain the high concentration necessary for our high temperature experiments is not possible with our available hardware, due to the high melting point of erbium. Instead, we add an in-between step, in which we mix $\sim 20\,\mathrm{mg}$ of erbium with $\sim 1.2\,\mathrm{g}$ of gold via arc-melting in a clean (5N) argon plasma. By rotating and remelting the resulting pellet multiple times, we ensure a homogeneous erbium distribution. The resulting pellet has a concentration of $\sim 1.5\,\%$, which we verify with a magnetization measurement using a commercial SQUID magnetometer[1]. After constructing 19 of these pellets, we add them to the preexisting target in a graphite crucible. At a pressure of $\lesssim 2 \times 10^{-4}\,\mathrm{mbar}$, we heat the crucible to 1100°C for 60 s, and then place the resulting disk in nitric acid to remove contaminants on the surface. After repeating the melting and etching steps a total of three times, sputtered Au:Er films show consistent erbium concentrations of $(2500 \pm 200)\,\mathrm{ppm}$ with minimal contamination.

The erbium we add is of a natural isotopic composition, instead of the favorable enriched ^{168}Er, since the cost of sufficient isotopically enriched ^{168}Er is high. Also, since the original target already contained non-enriched erbium, a significant amount of ^{167}Er would have still been present.

[1] QD MPMSR XL from Quantum Design Inc, 10307 Pacific Center Court, San Diego, CA 92121, USA.

5.2.2 High Temperature Set-up

The high temperature set-up is based on a refurbished detector arm originally designed for the maXs-20 detector [Sch12]. A digital render appears in figure 5.5. The arm itself is a 130 mm long copper rod, coated with a 1.5 µm thick layer of gold, which prevents oxidation. Mounted at the end is a copper disk with a diameter of 40 mm, onto which we can place a second, thinner, un-coated copper experimental holder with a printed circuit board. The latter two parts make up the detector module. This module is held in place by a set of commercially available plugs[2]. As shown in the reverse render, it thus allows for quick replacement with another detector module with a different experiment, which is glued to the center of the detector module. In the close-up, for instance, a Hot-maXs experiment is prepared. The detector itself sits next to two front-end SQUID chips, which are in turn bonded to the circuit board. Omitted for clarity is a collimator with a thin slit allowing for X-rays to impact the eight lead absorbers, while protecting the substrate and SQUIDs. The same is true for a niobium shell surrounding the entire detector arm, which acts as a superconducting shield. Read-out of the detector occurs via lines on the circuit board, which feed through to the back of the copper disk. From there, two standard plugs[3], allow for further read-out.

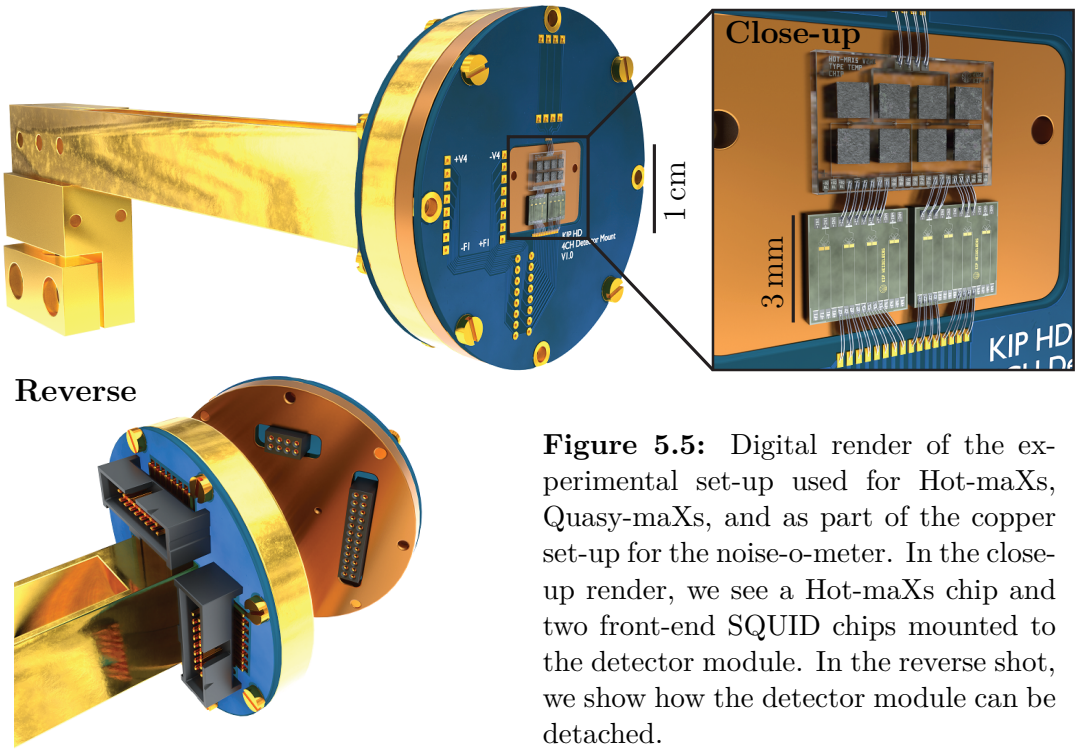

Figure 5.5: Digital render of the experimental set-up used for Hot-maXs, Quasy-maXs, and as part of the copper set-up for the noise-o-meter. In the close-up render, we see a Hot-maXs chip and two front-end SQUID chips mounted to the detector module. In the reverse shot, we show how the detector module can be detached.

[2]cut from SLR 2 50 G and BLR 2 50 Z type plugs by Fischer Elektronik GmbH & Co. KG. Nottebohmstraße 28, 58511 Lüdenscheid, Germany.

[3]SHF-108-01-L-D-SM by Samtec, New Albany, 520 Park East Boulevard, USA.

5.2.3 Absorber Fabrication

Adding the eight 1 mm × 1 mm × 100 µm superconducting lead absorbers is the last step in manufacturing a Hot-maXs chip. Using a CNC machine[4] with a 400 µm flat end mill, we cut absorbers individually out of a 200 µm thick lead foil. In the center of each absorber is a raised section with the same footprint as the sensor and a height of 30 µm, making each absorber look like a square mushroom. This contact pad ensures that physical contact to the main chip occurs primarily via the sensor.

In figure 5.6, a side-on view of a finished absorber (1) appears. In order to accurately align the absorbers, we construct a dedicated micro-fabricated chip (2). It is a 7 mm × 5 mm × 380 µm silicon substrate, into which we etch eight 50 µm deep square holes (3) using a Bosch process [Lae15], in an inductively coupled plasma etching system[5]. These depressions are dimensioned 50 µm larger than the footprint of the absorbers, allowing us to easily place inverted absorber mushrooms (4) inside. The contact pads of the absorbers now align with the sensors (5) of a Hot-maXs chip (6), which we place upside-down on top of the contact pads. Since the fused silica substrate is transparent, it is possible to use a microscope to look through the back of the Hot-maXs chip and align the sensor patches to the absorber contact pads by hand to within ∼ 50 µm.

In this configuration, we apply a weight of 400 g on top of the inverted Hot-maXs chip and heat the set-up to 150 °C for 60 minutes. In this diffusion welding process, gold atoms from the sensor intersperse with lead atoms from the absorber to join the two components. After cooling down, the absorbers are able to withstand up to ∼ 1 N of sideways force. When removed, the underside of the contact pads show clear markings from the meander-shaped pick-up coil, indicating that the weld was successful. In figure 5.7, we have taken a number of microscope images of an absorber still attached to a sensor through the transparent substrate of an upside-down Hot-

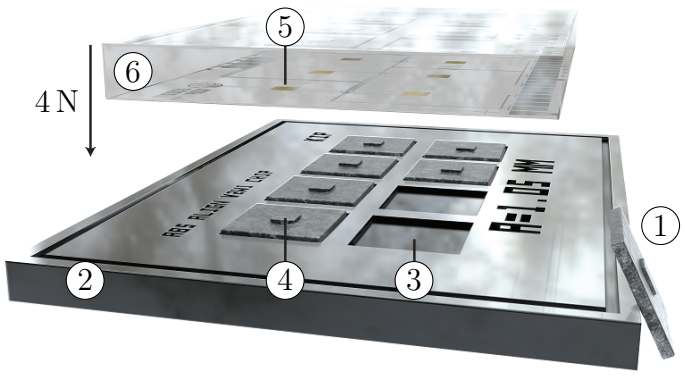

Figure 5.6: Digital render of our set-up designed for attaching lead absorbers to a Hot-maXs chip.

[4]COMPACT-Line 0404 by Sorotek, Withig 12, 77836 Rheinmünster, Germany.
[5]PlasmaPro 100 Cobra, Oxford Instruments, Abingdon OX13 5QX, United Kingdom.

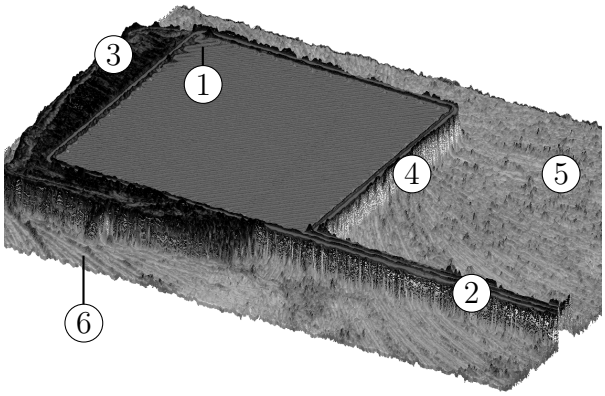

Figure 5.7: 3D profile extracted from stacked microscope images taken through the back of an inverted Hot-maXs chip after attaching an absorber.

maXs chip. Using focus stacking, we construct a 3D profile[6] of the underside of the absorber and the micro-structured layers of Hot-maXs. Visible is the pick-up coil (1), with meander stripes running horizontally. At the lower right, lines (2) run to the persistent current switch. Shifted by $\sim 40\,\mu m$ to the left of the pick-up coil is the underside of the contact pad of the absorber (3), which is slightly misaligned with respect to the pick-up coil. We see a 30 µm drop (4) to the bottom face of the absorber (5), which covers the entire image. This corresponds to a 30 µm gap between the substrate of Hot-maXs and the main body of the absorber and confirms that stem of the mushroom-shaped absorber has not collapsed. The circular markings (6) on the surface of the absorber originate from the milling process. Our tests demonstrate that we are able to align absorbers sufficiently well, perform a stable diffusion weld, and preserve the contact pad of the absorber.

5.3 Proof-of-Principle Measurements

Analogous to the first viewing of a newly constructed telescope, we present here the results of the first measurement - the first light - of a Hot-maXs detector. For this characterization, we irradiate our detector with an ^{55}Fe source and an ^{241}Am source simultaneously. As we mention in subsection 4.3.5, the spectrum of the former is characterized by peaks at 5.9 keV and 6.5 keV. The latter source decays with a half-life of 433 years via α-decay to ^{237}Np, which de-excites further. In particular the γ photons emitted from nuclear de-excitation are of interest to us, with the dominant energies being 26.345 keV and 59.541 keV [Pie12]. While the housing of the source absorbs the initial α particle as well as Auger electrons from the following de-excitations, X-rays and γ photons can reach our detector after passing through a beryllium window and a lead collimator. The latter is mounted in immediate vicinity to the Am source and is designed to reduce its effective activity, so that the photon rate from the Fe and Am sources are similar. The overall rate is ~ 0.8 Bq per pixel.

[6]Image created with PICOLAY by Heribert Cypionka, www.picolay.de.

5.3.1 Pulse Shape

In figure 5.8, we show pulses from 60 keV photons impacting Hot-maXs at temperatures between 41 mK and 300 mK. A wide variety of characteristic time constants is visible. In general, we observe larger pulses with an amplitude of up to $0.5\,\Phi_0$ at lower temperatures, which have slow rise times τ_0 and slow decay times τ_1. Towards higher temperatures, the pulse height decreases, and time constants are shorter, as expected. We are able to observe pulses up to temperatures of 300 mK, at which point we are limited by the signal-to-noise ratio.

We take a closer look at the pulse at 41 mK, which has a rise time of 95 µs. According to equation (2.3), we expect the first part of the quasiparticle thermalization process, that is the relaxation to the energy gap, to occur with a characteristic time of $\tau_s \approx 10\,\mu s$ at 41 mK. Since this value is significantly lower than our observed rise time, we believe that the quasiparticle recombination dominates. Consequently, recombination occurs with $\tau_{rec} \approx 85\,\mu s$, which cannot be explained solely by inelastic phonon processes [Kap76]. Instead, more complex dynamics, such as enhanced recombination at impurities, Abrikosov vortices, or increased disorder, are likely involved [Gol93, Ull98, Bar09]. Thermalization times approaching those of normal-conducting absorbers have been reported for $T \geq 2 \times 10^{-4}\,\Theta_D$ [Cos93, Wel08]. This condition is fulfilled for lead at 41 mK . With this assumption, we find that the thermalization of our absorber could be described as the thermalization of a normal-conducting lead absorber with a residual resistance ratio of $RRR = 2$. With a characteristic absorber length scale of $l = \sqrt{2(a_{abs}/2)^2 + (h_{abs}/2)^2} = 0.71\,\text{mm}$ and

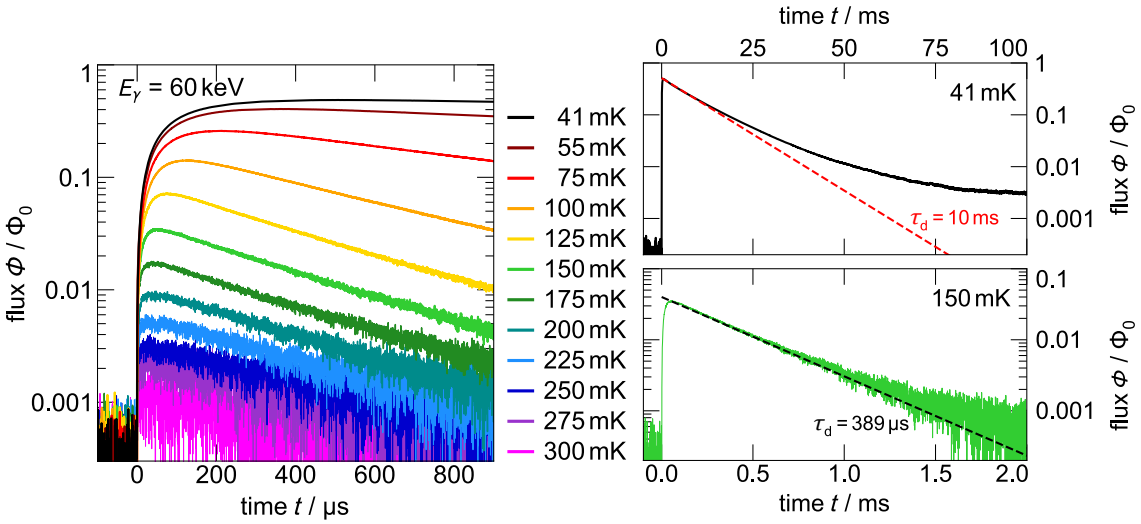

Figure 5.8: Hot-maXs response to a 60 keV photon at different temperatures. The field current in the meander-shaped pick-up coils is ∼ 90 mA.

a thermal diffusion constant $a(RRR = 2) \approx 5\,\mathrm{mm}^2/\mathrm{ms}$, such an absorber would thermalize via diffusion with a time constant $\tau_{\mathrm{dif}} = l^2/a \approx 100\,\mu\mathrm{s}$. However, since $RRR = 2$ would be an astoundingly low value for a pure, bulk material, it is unlikely that the signal rise time is limited by defect scattering.

The decay of the pulse at 41 mK is best visible in the longer time window in the top right of figure 5.8. We find a primary decay time of $\tau_1 \approx 10\,\mathrm{ms}$ and an additional tail with an amplitude of $\sim 0.5\%$, so there is no full thermalization with the thermal bath within the recorded time trace. Such a tail can be reliably found and is not the result of a random slope in the baseline. In contrast, the pulse at $T = 150\,\mathrm{mK}$ is well described by a single decay time of 389 µs. This can be explain by thermalization via the glassy substrate into the experimental holder, which we model as thermal diffusion originating from the sensor and moving outward radially. A similar decay time of $\tau_1 \approx 400\,\mu\mathrm{s}$ is visible for all pulses above 125 mK.

5.3.2 Energy Resolution

Data evaluation occurs in a similar fashion to Quasy-maXs and involves a template fit, time information cuts, a χ^2 cut, temperature correction, and an energy calibration [Bar23]. The thus obtained energy resolution of three Hot-maXs channels at 11 different temperatures appears in figure 5.9 a), where we evaluate 5000 to 20 000 signals per pixel. The baseline resolution is marked by squares. Best resolutions of 26.2 eV, 22.6 eV, and 23.9 eV for the three channels are reached at lowest temperatures, with the energy resolution increasing roughly by an order of magnitude for each 100 mK increase in temperature.

The exponential temperature dependence of the baseline energy resolution is supported by simulations (gray). However, the projected resolutions lie a factor of 2 to 3 lower. We believe that channels may suffer from temperature fluctuations from particle impacts in the substrate and neighboring pixels. Evidence for this comes from the noise spectrum, which gains a significant low frequency component after injecting a persistent current. Two points enhance the effect: First, the long thermalization time at low temperatures due to the weakly designed thermal link to the experimental platform makes each photon impact influence measurements for the subsequent hundreds of milliseconds. Second, since we place the absorbers manually onto the sensors, there are slight variations in the absorber position from pixel to pixel. As lead is superconducting, this directly influences the magnetic field distribution in the sensor material in a unique way, effectively reducing the gradiometry of each channel. Channels are thus more susceptible to chip-wide temperature fluctuations.

The difference in energy resolution at high temperatures between channel 3 and the other two channels is explained by different persistent currents I_0. While in channels

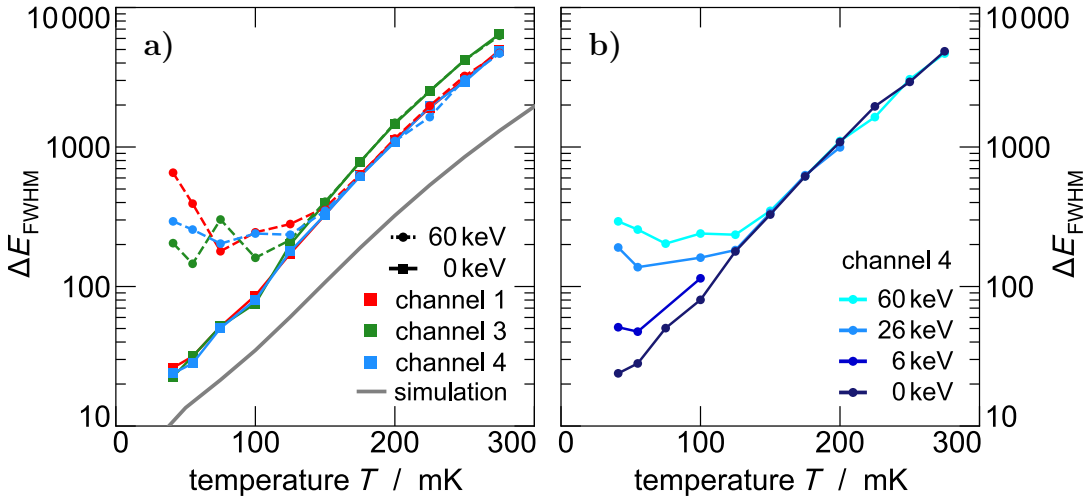

Figure 5.9: a) Temperature dependent energy resolution of Hot-maXs for baselines and at 60 keV. **b)** Energy resolution of a single channel for different photon energies.

1 and 4 we were able to inject up to 80 mA and 90 mA, respectively, we were unable to inject more than 20 mA into channel 3. According to simulations, this causes a degradation of the energy resolution only above $\sim$ 100 mK, which matches our data. The reason for the different maximal I_0 lies in a manufacturing error in the second niobium layer, where too-thick photoresist with significant undercut caused ill-defined structures in the region of the persistent current switch. For the same reason we were unable to inject any meaningful persistent current in channel 2, and we have omitted these data.

Appearing as circles in figure 5.9 a) is the energy resolution at 60 keV. Two distinct regions are apparent: above 125 mK, the energy resolution is almost identical to the baseline resolution. Here, we are limited by the stationary, total noise of the detector signal. Below 125 mK, however, the energy resolution is constant at around 200 eV. In this region, we find inconsistencies in the pulse shape, which manifest themselves on a variety of levels.

- Variations in both the **rise and decay times** are visible between different pulses of the same pixel. This may indicate an impact position dependence, which Hot-maXs is particularly susceptible to, due to the lack of a thermal bottleneck between absorber and sensor, especially in conjunction with the slow thermalization times of the absorber.

- We observe pulse shape variations dependent on **photon energies**. This can be explained in combination with the previous point, since low-energy photons are mostly absorbed in the upper parts of the absorber, while more energetic particles may penetrate deeper.

- **Different pixels** show different distributions of pulse shapes. We attribute this to the manually constructed absorbers, which have manufacturing inconsistencies untypically large for a microstructured device. One particular effect we observe is that some pixels show two families of pulses with slightly different pulse heights, which we believe originates from some absorbers being not fully free-standing and contacting the chip substrate. Some energy from a photon impacting near such a point may flow into the substrate before the sensor is thermalized.

Besides varying pulse shapes, a second reason for the high energy resolution may be poor temperature information. With the long low-energy tails in the order of hundreds of ms at low temperatures, and a comparatively high photon rate of $\sim$ 0.8 Bq per pixel, the channel we use for temperature information may not represent the chip temperature at some other position for a significant fraction of the time.

In figure 5.9 b), we plot the energy resolution of only one pixel for different photon energies. While at high temperatures we always reach the baseline resolution, the low temperature plateau is dependent on the input energy. This supports the explanation of being limited by variations in the pulse shape, since such effects are more influential at higher energies.

5.4 Future Improvements

In this chapter, we have presented a proof-of-principle MMC for high temperatures and have shown that we are able to detect 60 keV photons at up to 300 mK. To our knowledge, this is the highest temperature an MMC has ever been operated at. We were also able to identify a number of areas in which our prototype could benefit from improvements.

- An immediate upgrade is a correctly functioning **persistent current switch**, which would make pulses across channels more consistent, improve energy resolution at high temperatures, and give us higher statistics. We have located the relevant step in the manufacturing procedure and are aware how to avoid it in future.

- An upgrade to the absorber attaching process by implementing a **micromanipulator** could reduce variations between pixels.

- Less susceptibility to thermal fluctuations may be achieved by altering the chip substrate. One method of thermal isolation used for transition edge sensors is employing thin **silicon nitride membranes**, which have a low thermal

conductivity while having a relatively high mechanical strength [Uki00]. Due to the thin membrane, the chance for photon absorption in the substrate is low. Such a technique is currently considered for a metallic magnetic bolometer for cosmic microwave background measurements at temperatures of hundreds of millikelvin [Ger23].

- When given a specific operating temperature, it is possible to adjust the geometry of various components for **temperature specific optimization** of the energy resolution. For instance, the detector we present in this chapter is optimized for $T = 100\,\mathrm{mK}$. According to our simulations, by increasing the sensor volume, we can reduce the energy resolution at $T = 300\,\mathrm{mK}$ by around a factor of two.

Since this prototype is currently outperformed by more classical MMCs at lowest temperatures [Pie12], transition edge sensors at around 100 mK [Ohn17], and semiconductor detectors at high temperatures, an immediate applications is not obvious. However, as a demonstrator project, Hot-maXs sets a benchmark for future high temperature MMCs, and, with concrete ideas for improvements, hopefully inspires future work in this area.

Part II

Noise in Superconducting Microstructures

6. Overview of Noise Contributions

Noise, as we discuss it here, refers to random fluctuations in a physical quantity such as magnetic flux, current, or voltage. In this overview chapter, we introduce the necessary mathematical concepts and discuss the most relevant noise sources in the context of our experiments. Most commonly, we thereby refer to noise via its power spectral density, which we plot in a noise spectrum. The following section 6.1 gives an overview of these concepts. Regarding noise sources, we lay a particular focus on noise in metallic magnetic calorimeters, but at key sections we broaden our view to superconducting microstructures in general. We cover SQUID noise in section 6.2, magnetic Johnson noise in section 6.3, magnetic flux noise in section 6.4, and noise from energy fluctuations in section 6.5.

6.1 The Noise Spectrum

Since the topic of noise in electronics is too broad to cover here, we defer to literature for a general overview [Mot93, Kog96]. Instead, we introduce only those concepts relevant for the following chapters using a simple example. Consider a time trace $u(t)$ as it appears in gray in figure 6.1 a) representing the output voltage of a device. Its noise-free zero-signal (red) is obscured by voltage noise S_V. If we wish to experimentally quantify this noise, we perform a measurement of the time trace over a finite time $\mathcal{T}$. This is equivalent to applying a window function to $u(t)$. While commonly non-trivial functions such as the Hamming window or Blackman window are used in signal processing, the time traces we consider in this thesis work well with a simple rectangular window, resulting in the truncated time trace $u_\mathcal{T}(t)$, which is overlaid in black in figure 6.1 a). We then calculate the *Power Spectral Density* (PSD)

$$S(f) = \lim_{\mathcal{T}\to\infty} \frac{1}{\mathcal{T}} |\mathcal{F}\{u_\mathcal{T}\}(f)|^2 \tag{6.1}$$

of the time trace, which describes the noise power per frequency bin. Here, $\mathcal{F}\{u_\mathcal{T}\}$ is the Fourier transform of the truncated time trace $u_\mathcal{T}(t)$. In practice, we replace the limit in time $\mathcal{T} \to \infty$ with a limit in number of measurements $N \to \infty$, each with a finite measurement time $\mathcal{T}$, so that

$$S(f) = \lim_{N\to\infty} \frac{1}{N\mathcal{T}} \sum_j^N |\mathcal{F}\{u_{\mathcal{T},j}\}(f)|^2 \quad , \tag{6.2}$$

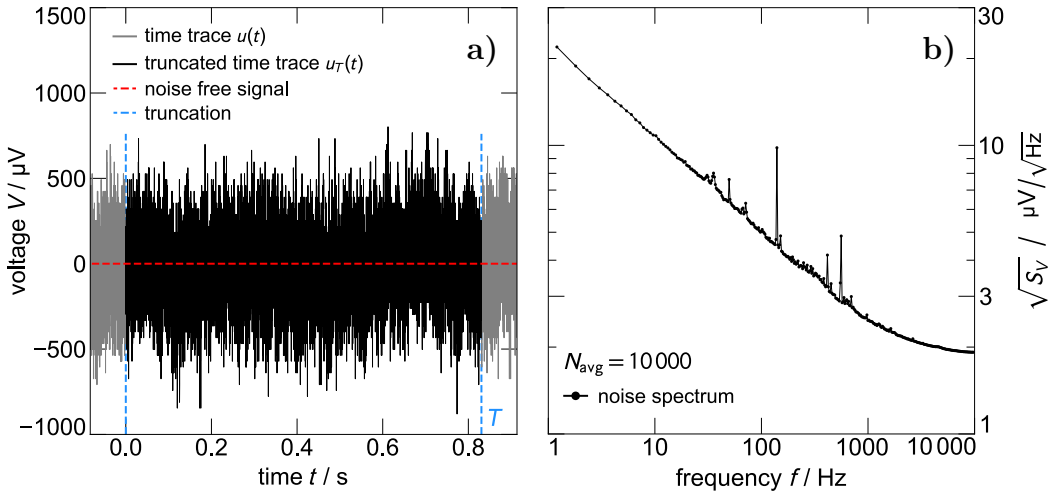

Figure 6.1: a) Example of a time trace $u(t)$ (gray) of the output voltage of a device with zero signal (red). Voltage noise S_V causes fluctuations. We truncate $u(t)$ over a finite time $\mathcal{T}$ and obtain $u_\mathcal{T}(t)$ (black). **b)** The power spectral density as calculated from 10 000 truncated time traces reveals the frequency dependence of S_V.

where we assumed our time traces to be ergodic. While this makes measurements and data handling much simpler, it does mean that the PSDs are limited to frequencies above $1/\mathcal{T}$, as supposed to the much lower $1/(N\mathcal{T})$ we could reach during the same measurement time.

An alternative way to think of the PSD is to first consider the auto-correlation function $R_{uu}(\tau)$, which for real signals is defined as the expectation value $\mathbb{E}$ of multiplying the signal with itself, but delayed by a certain time τ. Using the same truncation over a measurement time $\mathcal{T}$ as above, we find

$$\begin{aligned} R_{uu}(\tau) &= \mathbb{E}[u(t)\,u(t-\tau)] \\ &= \lim_{\mathcal{T}\to\infty} \frac{1}{\mathcal{T}} \int_0^{\mathcal{T}} u(t)\,u(t-\tau)\mathrm{d}t \\ &= \lim_{\mathcal{T}\to\infty} \frac{1}{\mathcal{T}} \int_{-\infty}^{\infty} u_\mathcal{T}(t)\,u_\mathcal{T}(t-\tau)\mathrm{d}t \quad . \end{aligned} \tag{6.3}$$

The Wiener-Khinchin theorem then states that the power spectral density is the Fourier transform of the auto-correlation function [Wie30, Khi34]. It follows that

$$\begin{aligned} S(f) = \mathcal{F}\{R_{uu}(\tau)\} &= \int_{-\infty}^{\infty} \lim_{\mathcal{T}\to\infty} \frac{1}{\mathcal{T}} \int_{-\infty}^{\infty} u_\mathcal{T}(t)\,u_\mathcal{T}(t-\tau)\mathrm{d}t\, e^{-2\pi i f\tau}\mathrm{d}\tau \\ &= \lim_{N\to\infty} \frac{1}{N\mathcal{T}} \sum_j^N \int_{-\infty}^{\infty} \int_{-\infty}^{\infty} u_{\mathcal{T},j}(t)\,u_{\mathcal{T},j}(t-\tau)\mathrm{d}t\, e^{-2\pi i f\tau}\mathrm{d}\tau \\ &= \lim_{N\to\infty} \frac{1}{N\mathcal{T}} \sum_j^N \mathcal{F}\Big\{ \int_{-\infty}^{\infty} u_{\mathcal{T},j}(t)\,u_{\mathcal{T},j}(t-\tau)\mathrm{d}t \Big\} \quad . \end{aligned} \tag{6.4}$$

If we apply the convolution theorem at this point, we once again arrive at the expression from equation (6.2).

Figure 6.1 b) shows the so-calculated PSD based on $N_{\mathrm{avg}} = 10\,000$ time traces. Note that we plot the square-root $\sqrt{S_V}$ of the PSD. While the units on the ordinate might change from voltage noise to flux noise or current noise, depending on the physical quantity studied, we display all noise data in a graph of this type, which we call a *noise spectrum*.

6.2 SQUID Noise

Due to the wide application range of SQUIDs [Cla06], understanding their noise is of great interest and a number of detailed texts exist in literature [Cla04, Wel04]. For our work, it is sufficient to divide SQUID noise into two basic components: low frequency $1/f$ noise and frequency independent white noise. The former is caused in part by two-level fluctuators in the Josephson junctions causing noise in the critical current and in the Josephson energy [Wak86, Wel04]. Additionally, there is a poorly understood temperature dependent magnetic flux noise component at low frequencies [Koc83, Kem16], which is present in a number of different superconducting microstructures. Indeed, one main motivation for experiments we present in chapter 7 is to get a better understanding of this magnetic flux noise. For now, however, we simply model the $1/f$ noise contribution with the phenomenological

$$S_{1/f} = \frac{S_{1/f,1\,\mathrm{Hz}}}{f^{\alpha}} \quad , \tag{6.5}$$

where we introduce the noise level at 1 Hz, $S_{1/f,1\,\mathrm{Hz}} = S_{1/f}(1\,\mathrm{Hz})$ and the exponent $\alpha \approx 1$.

The frequency independent white noise in SQUIDs is fundamentally thermal noise. Consider an Ohmic resistor with resistance R and temperature T. The thermal agitation of the electrons causes Johnson-Nyquist noise [Joh28, Nyq28] given by

$$S_V = 4k_{\mathrm{B}}TR \quad . \tag{6.6}$$

In a dc-SQUID at its working point, Johnson-Nyquist noise originates from the two shunt resistors R_{sh} and the two Josephson junctions[1]. We separate this noise into two parts: First, an in-phase component, in which the voltage noise across each part is identical. This leads to an overall voltage noise $4k_{\mathrm{B}}TR_{\mathrm{dyn}}$ across the SQUID, where $R_{\mathrm{dyn}} = \partial V/\partial I$ is the dynamic resistance of the SQUID as extracted from the Ohmic

[1] Note that we approximate the SQUID as a linear system by choosing only the first term of the Taylor expansion of the more general Nyquist theorem [Gup78, Gup82].

part of the I-V curve. Second, an out-of-phase component, in which the voltage noise across the SQUID is zero, but a noise current $4k_\mathrm{B}T/2R_\mathrm{sh}$ flows in the SQUID loop leading to flux noise in the SQUID. In this case, we neglected the Josephson junctions, as their contribution is small and difficult to quantify. The current noise S_I in the loop causes flux noise of $S_\Phi = L_\mathrm{s}^2 S_I$ in the SQUID, which we translate into voltage noise using the slope $V_\Phi = \partial V/\partial\Phi$ of the Φ-V curve. Overall, we obtain the white noise

$$S_{V,\mathrm{S}} = \frac{4\,k_\mathrm{B}T}{2R_\mathrm{sh}}\,L_\mathrm{s}^2 V_\Phi^2 + 4k_\mathrm{B}TR_\mathrm{dyn} \quad , \tag{6.7}$$

which is dependent on the working point. From numerical simulations [Tes77, Bru82], we find for a given L_s ideal values for R_sh and the working point and simplify the equation to

$$S_{V,\mathrm{S}} \approx 18k_\mathrm{B}TR_\mathrm{sh} \quad \text{and} \quad S_{\Phi,\mathrm{S}} \approx 18k_\mathrm{B}T\frac{L_\mathrm{s}^2}{R_\mathrm{sh}} \quad , \tag{6.8}$$

where we neglect the dynamic resistance of the SQUID.

In our experiments, we use a two-stage SQUID read-out, as introduced in subsection 2.5.2. As a result, the front-end SQUID, the SQUID array, and the necessary room temperature SQUID electronics all have noise contributions, which we must consider. A quantitative breakdown of these components for our experiment follows in subsection 7.1.1.

6.3 Magnetic Johnson Noise

Besides voltage noise, as described by equation (6.6), the Brownian motion of electrons in normal-conducting materials may also cause flux noise in an experiment. An example are random electron movements in the sensor or absorber of an MMC causing fluctuating magnetic fields, which then couple into the respective pick-up coil. In this particular case, we expect magnetic Johnson noise

$$S_{\Phi,\mathrm{J,m}} = \frac{2.376}{4\pi}\mu_0^2 k_\mathrm{B}T\sigma Ap\left(\mathrm{e}^{-2\pi z/p} - \mathrm{e}^{-2\pi(z+d)/p}\right) \quad , \tag{6.9}$$

caused by a cuboid of thickness d and electrical conductivity σ at a distance z above the meander-shaped coil with pitch p and overlapping area A [Pie08, Pie12]. In a slightly different geometry, in which the noise is picked up by a simple circular loop with area A oriented in parallel to, and at a distance z from the surface of a conducting plate of thickness d, the magnetic Johnson is

$$S_{\Phi,\mathrm{J}} = \frac{\mu_0^2 k_\mathrm{B}T\sigma d}{8\pi z^2}\cdot A^2 \quad . \tag{6.10}$$

The derivation assumes the lateral dimension of the conductor to be much larger than z and A, and $z \ll d$ [Var84, Rot98]. This is a good model for Johnson noise originating from the experimental platform a device is mounted to. Note that this latter equation allows for magnetic coupling of the noise across far larger distances, since the exponential terms caused by the high gradiometry of the meander coil are lacking. In either case, the noise is independent of frequency. This changes, however, when we consider the skin effect, which states that the current density of alternating current decreases exponentially with distance to the surface of the conductor. The characteristic length scale is the frequency dependent skin depth

$$\delta(f) = \sqrt{\frac{2}{2\pi f \mu_0 \sigma}} \quad . \tag{6.11}$$

This means that only parts of the conductor contribute, as soon as the skin depth corresponds to the thickness of the conducting plate. The result is a cut-off in the noise spectrum at a critical frequency f_c.

6.4 Magnetic Flux Noise

The topic of low frequency magnetic flux noise is a broad one, since it occurs in a wide variety of devices. Examples are flux, phase, and transmon qubits [Yos06, Bia07, Pal14], as well as SQUIDs [Dru11, Kem16], where it contributes to the $1/f$ noise discussed in section 6.2. Our focus lies here, however, on the $1/f$ erbium noise found in MMCs. This noise source, first observed in the early 2000s, is temperature independent [Fle04] and scales linearly with the amount of erbium, both when changing the erbium concentration [Fle03], and the volume of the Au:Er [Dan05]. These observations suggest that the source is, indeed, the erbium. Measurements using MMCs resulted in a noise level of $S_{\mathrm{m},1/f} \approx 0.1\mu_\mathrm{B}^2/\mathrm{Hz}$ per erbium ion at 1 Hz [Fle09a]. Using this value and equation (2.12), we calculate the erbium noise in the pick-up coil of an MMC to be

$$S_{\Phi,\mathrm{Er}} = \frac{\mu_0^2 \langle G^2 \rangle}{p^2} N_\mathrm{Er}\, S_{\mathrm{m},1/f} \cdot \left(\frac{f}{1\,\mathrm{Hz}}\right)^\alpha \quad , \tag{6.12}$$

where p is the pitch of the meander, G the geometry factor, N_Er the total number of erbium ions in the sensor, and $\alpha \approx 1$ the slope of the noise.

The physical mechanism behind this noise is not fully clear. One possibility is fluctuating, interacting magnetic moments. This mechanism causes magnetic flux noise in spin glasses [Kog81], which are characterized by a disordered magnetic state below a freezing temperature T_g. A thorough description of spin glasses is available in lit-

erature [Myd93]. A comparison with our Au:Er is natural, since especially metallic site-random spin glasses like $Au_{1-x}Fe_x$ and $Cu_{1-x}Mn_x$ are structurally similar, in that they consist of a low concentration of magnetic impurities diluted in a non-magnetic lattice. In fact, gold doped with a few hundred ppm of erbium does become a spin glass at temperatures well below 1 mK [Fle00]. However, the presumption that the physics is identical in both system is dubious, since the magnetic flux noise in spin glasses strongly decreases with temperature above T_g and we observe temperature independent erbium noise in Au:Er up to 4.2 K [Fle03].

Nevertheless, a comparison to spin glasses can be of great value, with our focus lying on the magnetic properties. One useful tool is the correlation of the in-phase component χ' of the magnetic susceptibility with the out-of-phase component χ''. Following [Lun81], the equation

$$\chi'' = \frac{\pi}{2} \frac{\partial \chi'}{\partial \ln f} \tag{6.13}$$

is fulfilled for spin glasses. Importantly, for this relation to hold, there must be a broad logarithmic distribution of magnetic relaxation times. This is the case in spin glasses, due to the formation of superparamagnetic clusters as described in Néel's cluster model [Nee49]. Simulations suggest that similar clusters form in Au:Er and Ag:Er alloys [Her22], which may be connected with erbium noise. We discuss this point further during the analysis of our data in subsection 7.4.2, where we use equation (6.13) as a metric for the distribution of relaxation times.

6.5 Noise from Energy Fluctuations

One fundamental noise source in MMCs originates from the particular connection of thermal systems within the device. Consider the thermodynamic model in figure 6.2, which is similar to the model we previously introduced in figure 2.7 a). We model an MMC as a collection of three thermal systems: the heat bath at a constant temperature T_0, the electronic system $C_{el} = C_{el,s} + C_{el,a}$, and the spin system C_z. These systems are linked by $G_{el,b}$ and $G_{z,el}$. Similar to the Johnson-Nyquist noise in equation (6.6), the fluctuation-dissipation theorem states that a thermal link G is the source of noise $S_P = 4k_B T^2 G$. This quantity has units of W^2/Hz and we can

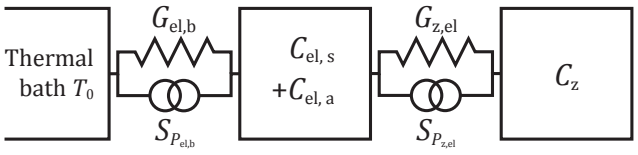

Figure 6.2: Thermodynamic model of an MMC. Each thermal link G is a source of noise S_P from energy fluctuations.

see it as fluctuating fluxes of heat, that is power, across the thermal links. In our thermodynamic model, we thus incorporate the two noise sources $S_{P_{\mathrm{el,b}}} \propto G_{\mathrm{el,b}}$ and $S_{P_{\mathrm{z,el}}} \propto G_{\mathrm{z,el}}$. Following calculations in literature [Fle05], we find that these cause the energy content of the spin system to fluctuate with a noise power spectral density

$$S_{\mathrm{ef}}(f) = k_{\mathrm{B}} C_{\mathrm{z}} T^2 \left((1-\alpha_1) \frac{4\tau_0}{1+(2\pi\tau_0 f)^2} + \alpha_1 \frac{4\tau_1}{1+(2\pi\tau_1 f)^2} \right) \quad . \tag{6.14}$$

The constant α_1 is dependent on the heat capacities and thermal conductivities, and can be approximated as the ratio $\beta = C_{\mathrm{z}}/(C_{\mathrm{el}} + C_{\mathrm{z}})$ for C_{el} not too different from C_{z} and $\tau_0 \ll \tau_1$. The rise and decay times τ_0 and τ_1 define two cut-off frequencies $(2\pi\tau_0)^{-1}$ and $(2\pi\tau_1)^{-1}$. As a result, the thermodynamic noise $S_{\mathrm{ef}}(f)$ has a characteristic double-plateau shape.

In the next chapter, we switch from a theoretical viewpoint of noise to an experimental one. We explore methods on how to quantify different noise sources in a device and present measurement results pertaining to some of the noise sources mentioned above. Towards the end of the chapter, we then relate the concept of noise to the dynamics of interacting moments and use our measurements to gain insight into the microscopic nature of sample materials.

7. Noise-o-meter - a Device to Disentangle Noise

As discussed in the previous chapter, an MMC can suffer from a plethora of different noise sources, such as read-out noise from SQUIDs, Johnson noise, magnetic flux noise, and noise from energy fluctuations. We try to minimize noise as much as possible in order to improve performance. The first step towards that goal is quantifying and understanding the noise. However, a simple measurement of the output of a device, such as in the example in figure 6.1, only gives us the frequency dependent sum of all noise components. The resulting noise spectrum thus does not allow us to identify individual noise sources and it can be difficult to minimize them.

In an effort to tackle this problem, we have developed a new device called the *noise-o-meter*. As the name suggests, its aim is to measure, and especially disentangle, different noise sources present in a particular superconducting device. A render of a first generation noise-o-meter chip appears in figure 7.1. This particular chip, for instance, is designed to identify noise sources in our high temperature MMCs: It features similar materials (niobium: gray, SiO_2: transparent, Au:Er: yellow), arranged to form similar components (meander-shaped coils, insulation layers, sensor layers). Using such a chip, we measure MMC-relevant noise in three different measurement modes, where each mode is sensitive to a different group of potential noise sources. By comparing the three results, we are able to identify the source of the most relevant noise components. With this knowledge, we can then improve the experimental set-up or the design of our MMCs accordingly.

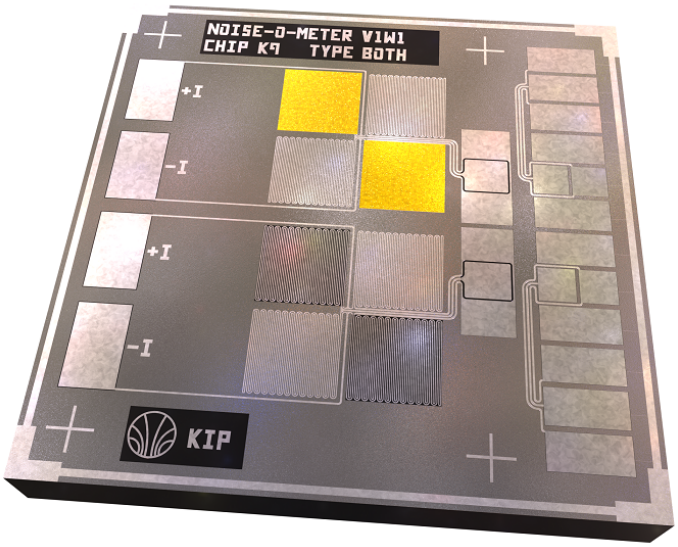

Figure 7.1: Digital render of a first generation noise-o-meter chip, designed to measure potential noise sources in high temperature MMCs. We recognize a number of components such as meander coils made of niobium (gray), insulating SiO_2 (transparent), and Au:Er sensor layers (yellow). A detailed explanation of the measurement methods, surrounding hardware, and calibration is the focus of this chapter.

Besides this purely practical application, there is an additional fundamental research aspect to the noise-o-meter. This is in regard to $1/f$ magnetic flux noise, which is a poorly understood phenomenon in many devices (see section 6.4). The noise-o-meter allows us to specifically measure magnetic flux noise via the complex impedance of the superconducting microstructure. We demonstrate this in chapter 7.4, where we analyze erbium noise, an important contribution to the magnetic flux noise of MMCs.

For now, we present the three measurement modes of the noise-o-meter in section 7.1, where we also introduce the concepts of cross-correlation and the fluctuation-dissipation theorem. Section 7.2 focuses on the two different experimental set-ups we use in conjunction with the noise-o-meter, followed by calibration measurements in section 7.3. Section 7.4 contains our experimental results, which we recently summarized [Her23], and we end with an outlook regarding the noise-o-meter in section 7.5.

7.1 Measurement Modes

For the following discussions, an overview of the layout of the noise-o-meter is of use. A diagram appears in figure 7.2. The central part is a 3.2 mm × 3.2 mm large silicon chip. Using micro-fabrication techniques, we deposit four meander-shaped coils made of superconducting niobium, arranged as a Wheatstone-like bridge. Each coil has an area of 500 µm × 500 µm and consists of 50 lines with a width of 5 µm and a pitch of 10 µm. If we wish to measure noise originating from a particular material, we place this material as a sample on two opposite coils. This changes the inductance of the underlying meander-shaped coil from L_0 to L. Note that the chip in the digital render above features two identical Wheatstone bridges, one with Au:Er sample material (top), and one to measure SiO_2 (bottom). In the diagram, on the other hand, we neglect the duplicate components for clarity.

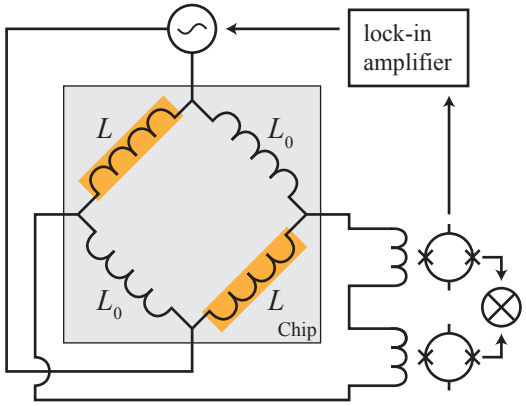

Figure 7.2: Circuit diagram of the noise-o-meter. A central chip (see figure 7.1) features four inductors arranged as a Wheatstone-like bridge, two of which are covered with a sample material (orange). Depending on the measurement mode, read-out of the chip occurs via a combination of SQUIDs and a lock-in amplifier.

Surrounding the chip are a number of devices used for read-out. Most important are a lock-in amplifier, and a set of two two-stage SQUID read-out chains, represented in the diagram by the symbol of a dc-SQUID. In the following sections we explain in detail the relevance of these devices when discussing the three different read-out methods: single channel mode, cross-correlation mode, and susceptibility mode.

7.1.1 Single Channel Mode

Of the three measurement modes, the most intuitive one is the *single channel mode*, which appears schematically in figure 7.3. We read out time traces using one of the two SQUID read-out channels and ignore grayed out components. Using the methods detailed in section 6.1, we can translate the time traces into a noise spectrum. The advantages of this measurement mode are twofold. First, data evaluation is simple enough that we have the option to perform it online in real time using the measurement software PAQs [Hen17]. This enables us to easily optimize parameters, such as the precise settings of the SQUIDs. Second, since only one SQUID is active and we supply no further external current, this measurement mode allows for the lowest possible temperatures.

The noise we read out is a combination of the noise originating from the noise-o-meter device, and noise from the read-out chain. The latter may, in some applications, be of interest in itself. Usually, however, such read-out noise obscures smaller, more interesting noise contributions from the device. In order to estimate the minimally measurable noise level, we sum up the different noise sources in the read-out chain.

White noise. Let us initially consider white noise, which has contributions from the front-end SQUID, the SQUID array, and the necessary room temperature control

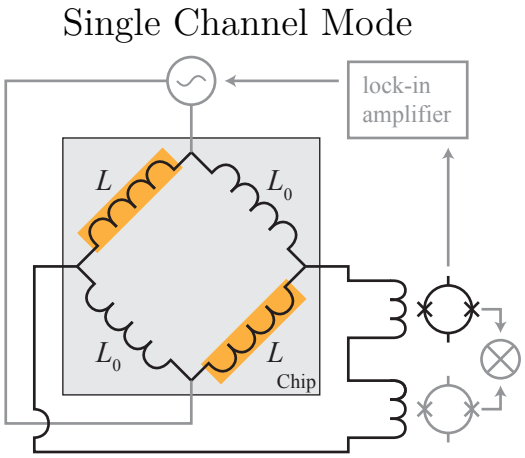

Figure 7.3: Schematic of the noise-o-meter in single channel mode. Using one of the two read-out chains, we read out the noise of the noise-o-meter circuit.

electronics. The noise from other components in the schematic in figure 2.6, such as the gain resistor $R_\mathrm{g} = 300\,\mathrm{m\Omega}$ and the current sources I_b1 and I_b2, are negligible [Kaa20]. Both for front-end SQUIDs and SQUID arrays, we use chips of the HDSQ series, which are developed and fabricated in-house by our research group. The front-end SQUIDs have shunt resistances of $R_\mathrm{sh} \approx 5\,\Omega$ and washer inductances in the order of $L_\mathrm{s} \approx 60\,\mathrm{pH}$. Using equation (6.8), we find a white noise level of around $\sqrt{S_{\Phi,\mathrm{s}}} \approx 0.1\,\mu\Phi_0/\sqrt{\mathrm{Hz}}$ at a typical working temperature of $T \approx 200\,\mathrm{mK}$ [Fer15]. Reducing the SQUID temperature in order to reduce noise is not feasible, since the Joule heating of the shunt resistors is too strong to be overcome by the relatively poor electron-phonon coupling of a thermal link to a colder heat bath.

The SQUID arrays[1] of the two-stage read-out chains consist of $N = 16$ SQUIDs connected in series, meaning that the flux-to-voltage transfer coefficient V_Φ is increased by a factor of N, while the voltage noise $\sqrt{S_{V,\mathrm{a}}} = \sqrt{18 k_\mathrm{B} T R_\mathrm{sh,a}}$ of individual SQUIDs adds up incoherently and only scales with $\sqrt{N}$. We estimate the shunt resistors in the array to be at $T \approx 400\,\mathrm{mK}$ and to have a resistance of $R_\mathrm{sh,a} = 3.6\,\Omega$ [Fer15], resulting in $\sqrt{N S_{V,\mathrm{a}}} \approx 76\,\mathrm{pV}/\sqrt{\mathrm{Hz}}$. Additionally, the HDSQ front-end SQUIDs and SQUID array chips are designed in a way that the flux change in the SQUID array is greater than that in the front-end SQUID by a factor of $G_\Phi \approx 2.6$ [Fer15].

Finally, we need to consider the room temperature control electronics[2]. Since they have a finite output impedance of $50\,\Omega$, we cannot consider them as a perfect voltage source and must include both the intrinsic white voltage noise of $\sqrt{S_{V,\mathrm{ce}}} \approx 0.33\,\mathrm{nV}/\sqrt{\mathrm{Hz}}$ and the intrinsic white current noise of $\sqrt{S_{I,\mathrm{ce}}} \approx 2.6\,\mathrm{pA}/\sqrt{\mathrm{Hz}}$ [Dru06]. For easier comparison, we translate these noise levels into effective flux noise in the front-end SQUID using typical transfer coefficients of $V_\Phi \approx 80\,\mu\mathrm{V}/\Phi_0$ and $I_\Phi \approx 4\,\mu\mathrm{A}/\Phi_0$ [Ric17]. Overall, we find an effective white noise level in our set-up of

$$\begin{aligned} S_{\Phi,\mathrm{w}} &= S_{\Phi,\mathrm{s}} + \frac{N S_{V,\mathrm{a}}}{G_\Phi^2 N^2 V_\Phi^2} + \frac{S_{V,\mathrm{ce}}}{G_\Phi^2 N^2 V_\Phi^2} + \frac{S_{I,\mathrm{ce}}}{G_\Phi^2 I_\Phi^2} \\ &\approx 0.01\,\frac{\mu\Phi_0^2}{\mathrm{Hz}} + 0.0005\,\frac{\mu\Phi_0^2}{\mathrm{Hz}} + 0.01\,\frac{\mu\Phi_0^2}{\mathrm{Hz}} + 0.06\,\frac{\mu\Phi_0^2}{\mathrm{Hz}} \approx 0.08\,\frac{\mu\Phi_0^2}{\mathrm{Hz}} \quad , \end{aligned} \tag{7.1}$$

with the control electronics dominating the white noise.

$1/f$ noise. At low frequencies, $1/f$ noise of the different components shifts the picture. When assuming a constant exponent of $\alpha \approx 1$, the noise at 1 Hz is a good metric. The room temperature electronics have $1/f$ noise of $\sqrt{S_{V,\mathrm{ce}}}(1\,\mathrm{Hz}) \approx 0.33\,\mathrm{nV}/\sqrt{\mathrm{Hz}}$ and $\sqrt{S_{I,\mathrm{ce}}}(1\,\mathrm{Hz}) \approx 13\,\mathrm{pA}/\sqrt{\mathrm{Hz}}$ [Dru06]. For the front-end SQUID,

[1] We label quantities referring to the SQUID arrays with the index 'a'.

[2] XXF-1 SQUID electronic by Magnicon, Magnicon GmbH, Barkhausenweg 11, 22339 Hamburg, Germany.

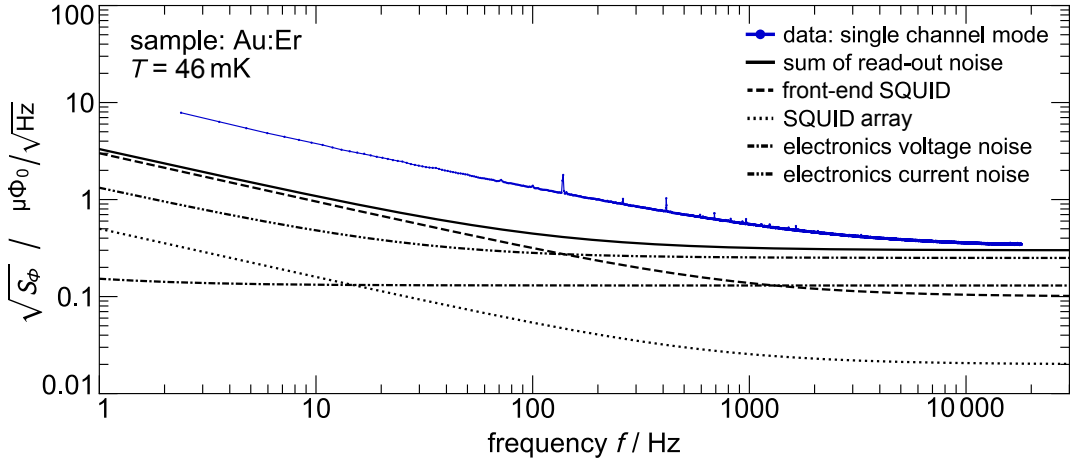

Figure 7.4: Measurement of a noise-o-meter with a Au:Er sample in single channel mode. Data appear in blue, with the estimated read-out noise plotted in various black lines.

we estimate $\sqrt{S_{\Phi,\mathrm{s}}}(1\,\mathrm{Hz}) \approx 3\,\mu\Phi_0/\sqrt{\mathrm{Hz}}$, and for the SQUID array $\sqrt{NS_{\Phi,\mathrm{a}}}(1\,\mathrm{Hz}) \approx 1.3\,\mu\Phi_0/\sqrt{\mathrm{Hz}}$ [Fer15]. A similar calculation to equation (7.1) then yields

$$S_{\Phi,1/f}(1\,\mathrm{Hz}) \approx 9\,\frac{\mu\Phi_0^2}{\mathrm{Hz}} + 0.25\,\frac{\mu\Phi_0^2}{\mathrm{Hz}} + 0.01\,\frac{\mu\Phi_0^2}{\mathrm{Hz}} + 1.6\,\frac{\mu\Phi_0^2}{\mathrm{Hz}} \approx 11\,\frac{\mu\Phi_0^2}{\mathrm{Hz}} \tag{7.2}$$

for the $1/f$ noise at 1 Hz. We thus expect the front-end SQUID to dominate $1/f$ noise and that $1/f$ noise is more significant than white noise at $f \lesssim 10\,\mathrm{Hz}$.

Figure 7.4 shows a measurement of a Au:Er sample in single channel mode. The noise spectrum has a white noise component visible at high frequencies, and a $1/f$ component dominant at low frequencies. In various black lines appear the four components of the read-out noise discussed above, including their sum, which approaches the measured data at high frequencies. We can deduce that read-out noise contributes significantly to the measured white noise, but that an additional low frequency component must originate from the experiment itself. We discuss this point further in subsections 7.1.2 and 7.4.2.

One important note is that the values pertaining to the SQUIDs are only rough estimates, since there is some variation from SQUID to SQUID. In particular, the $1/f$ noise at 1 Hz of our home-made front-end SQUIDs can vary from $1-5\,\mu\Phi_0/\sqrt{\mathrm{Hz}}$ [Kaa20]. As a result, every read-out channel will have slightly different noise, and we cannot simply subtract the noise levels calculated above to find the noise originating from the experiment. Instead, the values $\sqrt{S_{\Phi,\mathrm{w}}}$ and $\sqrt{S_{\Phi,1/f}}$ are estimates for the lower boundaries for the noise that we can detect in single channel mode.

7.1.2 Cross-correlation Mode

In single channel mode, the read-out chain limits the minimally measurable noise level. In order to improve its resolution, the noise-o-meter can operate in *cross-correlation mode*. A schematic appears in figure 7.5. We read out noise using two identical read-out chains ① and ② and cross-correlate the resulting time traces. In the following, we introduce the mathematical idea behind cross-correlation, estimate cross-talk between the read-out channels, and discuss methods to reduce cross-talk.

Cross-correlation

The noise-o-meter incorporates two complete and independent two-stage SQUID read-out chains ① and ② with independent noise contributions $n_1(t)$ and $n_2(t)$. If the noise produced within the experiment and before the read-out chain is given by a time trace $a(t)$, the total noise we read out in the two channels is

$$\begin{aligned} u(t) &= a(t) + n_1(t) \quad \text{and} \\ v(t) &= a(t) + n_2(t) \quad . \end{aligned} \tag{7.3}$$

We now apply the concept of cross-correlation, which allows us to remove uncorrelated components from a pair of signals, leaving us only with those components that are present in both signals. Mathematically, the cross-correlation

$$R_{uv}(\tau) = \mathbb{E}[u(t)\, v(t-\tau)] \tag{7.4}$$

of the two real-valued time traces $u(t)$ and $v(t)$ is very similar to the auto-correlation introduced in section 6.1. Following the same calculations, given by equations (6.3)

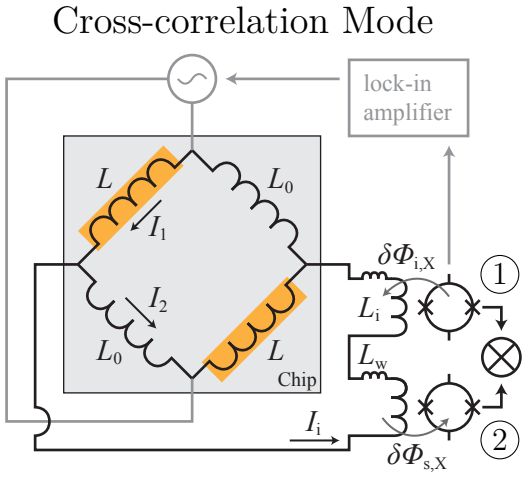

Figure 7.5: Schematic of the noise-o-meter in cross-correlation mode, in which we read out noise via two cross-correlated read-out chains. To calculate cross-talk from channel ① to channel ②, we assume a flux change $\delta\Phi_{\mathrm{i,X}}$ from one read-out chain feeds back into the circuit, causing a flux change $\delta\Phi_{\mathrm{s,X}}$ in the other read-out chain.

and (6.4), we find

$$S_{uv}(f) = \lim_{N\to\infty} \frac{1}{N\mathcal{T}} \sum_{j}^{N} \mathcal{F}\left\{ \int_{-\infty}^{\infty} u_{\mathcal{T},j}(t)\, v_{\mathcal{T},j}(t-\tau) \mathrm{d}t \right\} \quad . \tag{7.5}$$

By applying the convolution theorem in order to Fourier transform the two time traces individually, we get

$$S_{uv}(f) = \lim_{N\to\infty} \frac{1}{N\mathcal{T}} \sum_{j}^{N} \mathcal{F}^*\{u_{\mathcal{T},j}\}(f) \cdot \mathcal{F}\{v_{\mathcal{T},j}\}(f) \quad , \tag{7.6}$$

where the asterisk denotes the complex conjugate. In the following, we simplify notation by introducing the truncated Fourier transform $X = \mathcal{F}\{x_{\mathcal{T}}(t)\}$ of a time trace $x(t)$. The experimentally measured quantity $\langle S_{uv} \rangle_N$, which is the cross-correlated power spectral density averaged over N measurements, is

$$\begin{aligned} \langle S_{uv} \rangle_N &= \frac{1}{\mathcal{T}} \langle U^* V \rangle_N \\ &= \frac{1}{\mathcal{T}} \langle (A^* + N_1^*)(A + N_2) \rangle_N \\ &= \frac{1}{\mathcal{T}} \left(\langle A^* A \rangle_N + \langle A^* N_2 \rangle_N + \langle N_1^* A \rangle_N + \langle N_1^* N_2 \rangle_N \right) \\ &= \frac{1}{\mathcal{T}} \langle A^* A \rangle_N + \mathcal{O}\left(1/\sqrt{N}\right) \quad . \end{aligned} \tag{7.7}$$

In the crucial last step we use the fact that the time traces of each noise source fluctuate randomly around zero, meaning that the expectation value of the Fourier transform is zero as well. Multiplying the Fourier transforms of two uncorrelated noise sources again results in a random fluctuation and an expectation value of zero. The product of two correlated spectra such as A^* and A, however, is always positive and the average does not vanish for large N.

As a result of the cross-correlation, we are left with only the noise $S_a = \frac{1}{\mathcal{T}} \langle A^* A \rangle$ originating from the experiment, if we average over a sufficiently large number of measurements. We are thus able to measure noise sources that would otherwise be hidden beneath the read-out noise. An example appears in figure 7.6, where we repeat the measurement previously shown in figure 7.4. Here, data from single channel mode in blue has a low frequency $1/f$ component and a white noise component dominating at high frequency, with an unknown read-out noise component. By applying cross-correlation (red), we see that there is a significant $1/f$ component at low frequencies that does not originate from the read-out. We are able to measure this component also at high frequencies, where it lies an order of magnitude beneath the single channel noise.

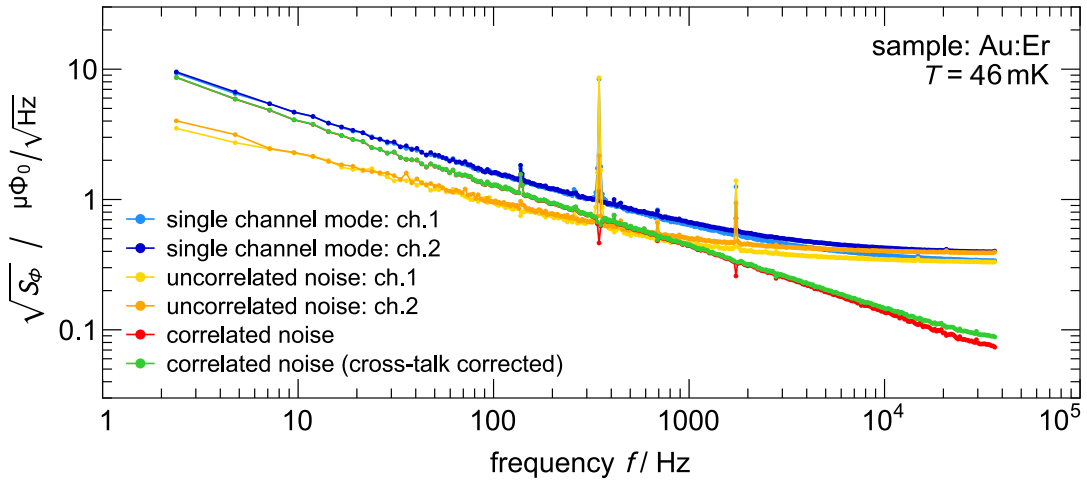

Figure 7.6: Recorded noise spectrum of a noise-o-meter with a Au:Er sample. Single channel mode data appears in blue. By cross-correlating, we make the correlated (red) and uncorrelated (yellow) components visible. When applying mathematical cross-talk correction to the correlated data (see end of subsection 7.1.2), we obtain the green curve, which is a better representation of the ideal cross-talk free correlated noise.

A slight modification of equation (7.7) enables us to also calculate the uncorrelated noise: Instead of performing the cross-correlation between $u_\mathcal{T}$ and $v_\mathcal{T}$, we use, for instance, $u_\mathcal{T}$ and $u_\mathcal{T} - v_\mathcal{T}$. By cross-correlating these quantities, we get

$$\begin{aligned}\langle S_{u,u-v}\rangle_N &= \frac{1}{\mathcal{T}}\langle (A^* + N_1^*)(A + N_1 - A - N_2)\rangle_N \\ &= \frac{1}{\mathcal{T}}\left(\langle A^* N_1\rangle_N - \langle A^* N_2\rangle_N + \langle N_1^* N_1\rangle_N - \langle N_1^* N_2\rangle_N\right) \\ &= \frac{1}{\mathcal{T}}\langle N_1^* N_1\rangle_N + \mathcal{O}\left(1/\sqrt{N}\right) \quad ,\end{aligned} \tag{7.8}$$

which results in only the read-out noise of channel one. Similarly, we obtain noise of channel two by cross-correlating $v_\mathcal{T}$ and $v_\mathcal{T} - u_\mathcal{T}$. The results appear in yellow in figure 7.6 and represent the actual read-out noise in the measurement. In this example, we find white noise levels of $\sqrt{S_{\Phi,\mathrm{w},1}} = 0.33\,\mu\Phi_0/\sqrt{\mathrm{Hz}}$ and $\sqrt{S_{\Phi,\mathrm{w},2}} = 0.40\,\mu\Phi_0/\sqrt{\mathrm{Hz}}$ for channels 1 and 2, respectively. The $1/f$ noise at 1 Hz is $\sqrt{S_{\Phi,1/f,1}} = 5\,\mu\Phi_0/\sqrt{\mathrm{Hz}}$ with $\alpha = 0.73$ and $\sqrt{S_{\Phi,1/f,2}} = 6\,\mu\Phi_0/\sqrt{\mathrm{Hz}}$ with $\alpha = 0.74$, which was previously obscured by the red, correlated component of the noise-o-meter device. These values for read-out noise roughly match our calculations in subsection 7.1.1 and show the variation in read-out noise between channels.

Cross-talk

In the calculations above, we assume that the two read-out channels are perfectly independent of each other, so that cross-correlation removes all components that do not originate from the experiment. However, in a realistic experimental setting, there will be a finite amount of cross-talk between the channels, leading to a finite amount of left-over read-out noise after cross-correlation. This component then is indistinguishable from noise originating from the main experiment and distorts our final results. The main channel of cross-talk is via the linked input coils of the two front-end SQUIDs. Any noise that feeds back from one SQUID into this part of the circuit can thus directly reach the other SQUID causing a correlated read-out noise component.

Consider a model of the noise-o-meter as in figure 7.5. Here, we combined the inductances of the aluminum bonds between a SQUID and the noise-o-meter chip into L_w and assumed that all inductors in the Wheatstone bridge are identical with an inductance of L_0. Cross-talk coupling into the SQUID input coil at channel (1) causes a flux change $\delta\Phi_{\mathrm{i,X}}$, where the first index refers to the location of the flux and the second the cause, X-talk. A variety of current changes δI_1, δI_2, and δI_i (see figure 7.5) follow, which finally results in a flux change $\delta\Phi_{\mathrm{s,X}}$ in the front-end SQUID of channel (2). Using flux conservation in closed superconducting loops and current conservation at vertices, we find the system of equations

$$\begin{aligned} 0 &= 2L_0\delta I_1 + 2L_0\delta I_2 \\ 0 &= -2L_0\delta I_2 + 2(L_\mathrm{i} + L_\mathrm{w})\delta I_\mathrm{i} - \delta\Phi_{\mathrm{i,X}} \\ 0 &= -\delta I_1 + \delta I_2 + \delta I_\mathrm{i} \quad , \end{aligned} \tag{7.9}$$

which we solve to find the flux change

$$\delta\Phi_{\mathrm{s,X}} = M_\mathrm{is}\frac{\delta\Phi_{\mathrm{i,X}}}{L_0 + 2(L_\mathrm{i} + L_\mathrm{w})} \tag{7.10}$$

in the SQUID due to cross-talk. As previously defined, M_is refers here to the mutual inductance between input coil and front-end SQUID.

By similar means, we calculate that a flux change $\delta\Phi_\mathrm{m}$ produced by a magnetic sample in one of the meander coils of the Wheatstone bridge results in a flux change

$$\delta\Phi_{\mathrm{s,m}} = M_\mathrm{is}\,\frac{\delta\Phi_\mathrm{m}}{2L_0 + 4(L_\mathrm{i} + L_\mathrm{w})} \tag{7.11}$$

in the SQUID. While at first glance both these couplings should vanishes for large L_0, we can keep $\delta\Phi_{\mathrm{s,m}}$ almost independent of L_0, as $\delta\Phi_\mathrm{m} \propto L_0$. This is the case,

because the increase of L_0 is the result of an increase in inductor area A_m and thus an increase of probed sample material. We then find $\delta\Phi_\mathrm{m} \propto A_\mathrm{m} \propto L_0$, and indeed an L_0-independent $\delta\Phi_\mathrm{s,m}$. As a result, the ratio

$$\frac{\delta\Phi_\mathrm{s,m}}{\delta\Phi_\mathrm{s,X}} \propto L_0 \tag{7.12}$$

of the two possible signals increases for larger meander coils to the point that it is theoretically possible to effectively remove cross-talk via the linked input coils. For the noise-o-meters used in this thesis, we use a Wheatstone bridge with an area of $1\,\mathrm{mm} \times 1\,\mathrm{mm}$ with $L_0 \approx 7\,\mathrm{nH}$, and expect $\delta\Phi_\mathrm{s,X} \approx 0.02\,\delta\Phi_\mathrm{i,X}$. This is an upper limit for the cross-talk via the input coils, since it represents the maximum amount of the signal that can get transferred between SQUIDs. We expect the actual cross-talk to be smaller and discuss its size in subsection 7.3.2.

Mathematical Reduction of Cross-talk

In practice, a perfect removal of cross-talk by increasing L_0 is not possible due to size or sample constraints. However, we can improve our result by mathematically correcting for cross-talk. We assume a simple model in which some fraction ε of the originally cross-talk free signals $u(t)$ and $v(t)$ from equation (7.3) are fed to the respectively other channel. The actually measured time traces are then

$$\begin{aligned} s_1(t) &= (1-\varepsilon)\,u(t) + \varepsilon\,v(t) \quad \text{and} \\ s_2(t) &= (1-\varepsilon)\,v(t) + \varepsilon\,u(t)) \quad , \end{aligned} \tag{7.13}$$

which we solve to obtain cross-talk-corrected free signals

$$\begin{aligned} u(t) = a(t) + n_1(t) &= \frac{s_1(t) - \varepsilon(s_1(t) + s_2(t))}{1-2\varepsilon} \quad \text{and} \\ v(t) = a(t) + n_2(t) &= \frac{s_2(t) - \varepsilon(s_1(t) + s_2(t))}{1-2\varepsilon} \quad . \end{aligned} \tag{7.14}$$

Cross-correlating these corrected signals then yields a more precise value for the noise $a(t)$ originating from the experiment. In the example in figure 7.6, such a correction with $\varepsilon = -1\,\%$ (see subsection 7.3.2) appears in green. The strongest difference is visible at high frequencies, since the absolute value of the noise is smallest there. Note that both a correction which increases or decreases the noise is thinkable, depending on the sign of ε. The circuit of the noise-o-meter suggests ε to be negative.

7.1.3 Noise Read-out Using Susceptibility

The third and final measurement mode of the noise-o-meter is the *susceptibility mode*. In contrast to the first two measurement modes, we are not merely listening for noise, but actively probing the sample material by driving the Wheatstone bridge with an alternating current $I_0(f,t) = \hat{I}_0 e^{i2\pi ft}$. Looking at the corresponding circuit diagram in figure 7.7, this current flows equally along the left and right branch, if all four inductors in the Wheatstone bridge are identical. This symmetry is broken, however, if we coat two opposite inductors with a sample material with a finite magnetic susceptibility χ. This changes the inductance of the coils to $L = (1 + \chi F)L_0 \neq L_0$, with a dimensionless filling factor $F < 1$. Since there is no sample material underneath the meanders, the filling factor is even bound by $F < 0.5$ here. Some current $I_\mathrm{i}(f,t) = \hat{I}_\mathrm{i} e^{i(2\pi ft-\theta)}$ now flows through the input coils of the front-end SQUIDs and is measurable. We use only one of the read-out chains, at the end of which sits a lock-in amplifier[3] [Cos34]. This device compares the output signal with the driving alternating current, giving us a precise measure of the relative amplitude $\hat{I}_\mathrm{i}/\hat{I}_0$ and the phase difference θ between I_i and I_0.

In order to quantify how the measured $\hat{I}_\mathrm{i}/\hat{I}_0$ and θ relate to the sample material, we perform a calculation similar to the cross-talk calculation in section 7.1.2. We make use of flux conservation in closed superconducting loops, and current conservation at vertices, and find the system of equations

$$\begin{aligned} 0 &= -LI_1 - L_0 I_2 + L_0 I_3 + LI_4 \\ 0 &= -L_0 I_2 - LI_4 - 2(L_\mathrm{i} + L_\mathrm{w})I_\mathrm{i} \\ I_0 &= I_1 + I_3; \quad I_0 = I_2 + I_4; \quad I_1 = I_2 + I_\mathrm{i} \quad , \end{aligned} \tag{7.15}$$

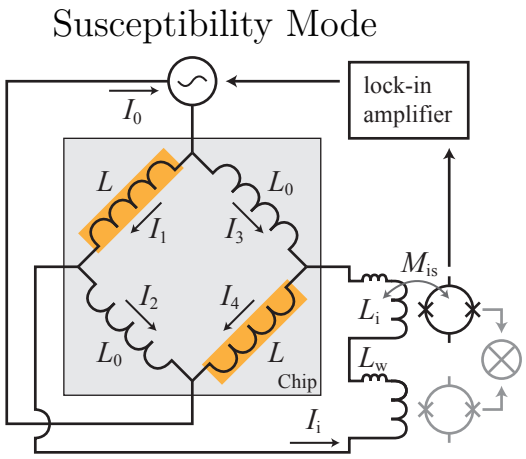

Figure 7.7: Schematic of the noise-o-meter in susceptibility mode. We drive an alternating current I_0 through the Wheatstone bridge, which results in a finite current I_i flowing through the input coils of the front-end SQUIDs, if $L \neq L_0$. We compare these currents with a lock-in amplifier and calculate the complex susceptibility $\chi' + i\chi''$ and the magnetic flux noise produced by the sample.

[3]Signal Recovery 7265 DSP Lock-In Amplifier, AMETEK GmbH, Rudolf-Diesel-Straße 16, 40670 Meerbusch, Germany.

which we solve to get the relation

$$I_{\mathrm{i}}(f,t) = I_0(f,t)\frac{L-L_0}{2L_{\mathrm{tot}}} = I_0(f,t)\frac{\chi F L_0}{2L_{\mathrm{tot}}} \quad . \tag{7.16}$$

Here, we introduced the total inductance $L_{\mathrm{tot}} = (L+L_0)/2 + 2(L_{\mathrm{i}}+L_{\mathrm{w}})$ of the circuit as experienced by I_{i}. We see that I_{i} is dependent on L, and thus on the sample's magnetic susceptibility χ. The latter is a complex quantity $\chi = \chi' + i\chi''$ and describes the magnetic behavior of the sample. The real component

$$\chi' F = \frac{2L_{\mathrm{tot}}}{L_0}\frac{\hat{I}_0}{\hat{I}_{\mathrm{i}}}\cos(\theta) \tag{7.17}$$

is a measure for the number of magnetic moments orienting themselves in the magnetic field fast enough to be in phase with the continuously changing AC field. As we elude to in chapter 2.2, this is dependent on a complex network of microscopic interactions for a material such as Au:Er. The noise-o-meter now offers us a method to probe these interactions by measuring the frequency and temperature dependence of $\chi' = \chi'(f,T)$. The imaginary component

$$\chi'' F = \frac{2L_{\mathrm{tot}}}{L_0}\frac{\hat{I}_0}{\hat{I}}\sin(\theta) \tag{7.18}$$

is caused by magnetic moments in close vicinity to a meander coil not orienting themselves instantaneously with respect to the magnetic field generated by I_0. Since energy is temporarily stored in the spin system, χ'' represents a loss. In fact, since the total inductance $L_{\mathrm{b}} = 1/2\,(L+L_0)$ of the Wheatstone bridge becomes a complex quantity, the bridge's impedance Z_{b} gains a dissipative component

$$\begin{aligned}
\mathrm{Re}(Z_{\mathrm{b}}) &= \mathrm{Re}\,(i\,2\pi f\,L_{\mathrm{b}}) \\
&= \mathrm{Re}\,(i\,\pi f\,(L+L_0)) \\
&= \mathrm{Re}\,(i\,\pi f\,(2L_0 + L_0(\chi'+i\chi'')F)) \\
&= -\pi f L_0 \chi'' F \quad .
\end{aligned} \tag{7.19}$$

Since $\chi'' < 0$, this corresponds to a real, positive resistance of the Wheatstone bridge with a corresponding voltage noise

$$S_V(f) = 4k_{\mathrm{B}}T\,\mathrm{Re}(Z_{\mathrm{b}}) \quad . \tag{7.20}$$

It is important to understand what this quantity represents. The above equation is a special case of the fluctuation-dissipation theorem - a general concept in statistical physics, which links a fluctuating quantity, such as noise, with a dissipating quantity,

such as resistance [Cal51]. The theorem states that they are directly proportional. The microscopic origin of the two quantities is identical. Since in our case the dissipative part originates from magnetic moments in close vicinity to the meander coils, the noise in (7.20) consists of only magnetic flux noise. More precisely, it is the magnetic flux noise that is distributed asymmetrically across the Wheatstone bridge, since any symmetric component, such as magnetic moments in large-scale, insulating SiO_2 layers, would affect all meander coils equally and not cause a change in I_i. Since the Wheatstone bridge is symmetric except for the sample material, by measuring the imaginary part χ'' of the susceptibility, we measure only magnetic flux noise from the sample material.

In a final step, we transform the voltage noise into flux noise in the front-end SQUID. Since $S_V(f)$ is created across the impedance $Z_\mathrm{tot} = i\,2\pi f L_\mathrm{tot}$ of the entire Wheatstone bridge, we obtain the important relation

$$\sqrt{S_\Phi(f)} = M_\mathrm{is}\,\frac{\sqrt{S_V(f)}}{|Z_\mathrm{tot}|} = \frac{M_\mathrm{is}}{L_\mathrm{tot}}\sqrt{\frac{k_\mathrm{B}TL_0|\chi''|F}{\pi f}} \quad . \tag{7.21}$$

7.2 Experimental Set-up

As we discuss in the introduction to this chapter, the noise-o-meter has two central applications: First, analyzing noise sources affecting a specific device, in our case high temperature MMCs. Second, performing fundamental research, especially regarding $1/f$ magnetic flux noise. For this reason, we have developed two different experimental set-ups to match the needs of these two applications. The first set-up is designed to mimic an MMC environment as closely as possible, in order to find noise sources affecting our detectors. Based on the material of the chip holder, we call it the *copper set-up*. The second is designed to maximize the performance of the noise-o-meter and has low background noise and a large temperature range. This *silver set-up* is well suited to measure sample materials in general and determine their magnetic flux noise. Both set-ups are based on the general layout in figure 7.2, but differ in their concrete implementation, which we explain in this section.

7.2.1 Copper Set-up

A schematic of the noise-o-meter chip used for the copper set-up appears in figure 7.8. The chip is based on a 3.2 mm × 3.2 mm × 250 µm high-purity silicon substrate. The main structures consist of 250 nm thick niobium (red), which becomes superconducting below 9.2 K. The structures make up two separate, identical versions of the experiment, one on the top and one on the bottom of figure 7.8. As a result, it is pos-

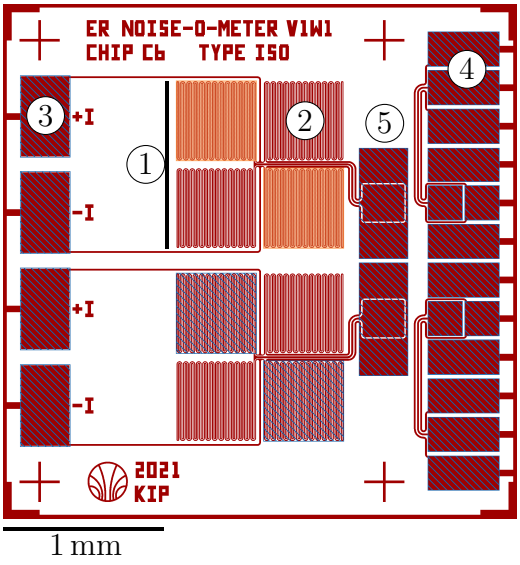

Figure 7.8: Design of the noise-o-meter chip used for measurements with the copper set-up. Each chip features two identical superconducting circuits made of niobium (red). Each Wheatstone bridge (1) consists of four meander-shaped coils (2). The entire chip is covered with insulating SiO_2, except for areas marked with blue hatching in the lower bridge. In the upper bridge, Au:Er sample material (orange) covers two meander coils. Bond pads lead to the AC source (3) and to SQUIDs (4), (5).

sible to measure two different sample materials during one cool-down of the cryostat. This saves measurement time and allows the user to measure two samples in precisely the same environment. At the center of each section is the Wheatstone bridge (1), consisting of four identical meander-shaped coils arranged in a square. Each meander coil (2) consists of 50 lines with a width of 5 µm and a pitch of 10 µm. On the left are bond pads to feed in the alternating current necessary for the operation in susceptibility mode (3), and on the right are bond pads for SQUID read-out (4). These are arranged to allow either for single channel read out or for cross-correlated read-out. In the former case, we connect the SQUIDs directly to the left column of bond pads (5). In the latter, we connect the left column with the right column via bonds, and then bond the SQUIDs to the right column of bond pads. The entire chip and its circuitry, with the exception for areas marked in blue such as the bond pads, is covered with sputtered SiO_2. Sample materials must be deposited on opposite meander coils. In figure 7.8, we see Au:Er (orange) deposited on the top Wheatstone bridge, while the bottom bridge features holes in the SiO_2 layer (blue hatching). These holes act as a sample material in susceptibility mode, just as squares of SiO_2 would, since only the asymmetry in the distribution of material is relevant.

Since the aim of the copper set-up is to mimic the environment of an MMC as closely as possible, we place the chip on precisely the same experimental holder we already presented in subsection 5.2.2. The chip has the same dimensions and bond pad layout as Quasy-maXs, with the lines for the alternating current designed to run through the same wires that the field and heater lines use in an MMC set-up. We use the same front-end SQUIDs and SQUID arrays, the same read-out system, cryostat, and shielding. Overall, the copper set-up allows for fast, representative, and easily implementable measurements in a typical MMC environment, without the need to add additional, or modify existing hardware such as wiring, SQUIDs, or shielding.

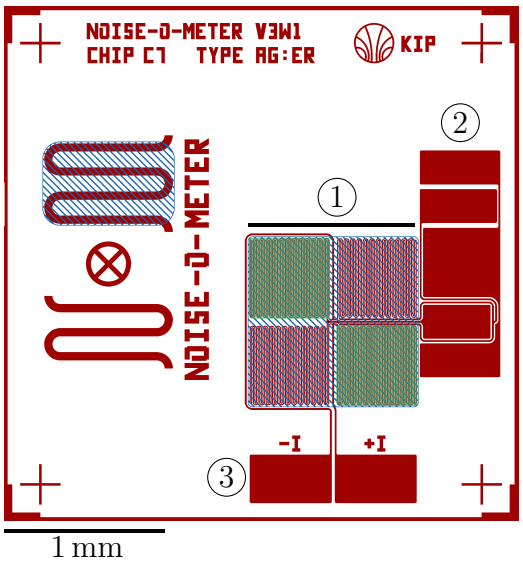

Figure 7.9: Schematic of a noise-o-meter chip designed for measurements with the silver set-up. A single Wheatstone bridge (1) is fully covered with SiO_2 and asymmetrically covered with Ag:Er sample material (green). Note that, while in figure 7.8 the blue hatching marks holes in the SiO_2, it represents actual SiO_2 structures, here. The Wheatstone bridge sits close to bond pads leading to the SQUIDs (2) and to bond pads for the driving current (3).

7.2.2 Silver Set-up

In the framework of the Bachelor's thesis of *Rui Yang* [Yan23], we have developed a second experimental platform designed for low-noise measurements of sample materials. Data on Ag:Er samples originate from this set-up. A noise-o-meter chip, designed to work with the silver set-up, appears in figure 7.9. The silicon substrate has dimensions of 3.2 mm × 3.2 mm × 380 µm. Microstructured on top is only one Wheatstone bridge (1), since the silver experimental holder only allows for read-out of two SQUIDs. The dimensions of the meander-shaped coils are identical to those in the copper set-up. Bond pads on the right (2) lead to the SQUIDs and bond pads for the driving current are on the bottom (3). Since high precision measurements always require cross-correlation, the option to only use one read-out channel is omitted. In exchange, the shorter bonding wires and lines leading to the Wheatstone bridge have less inductance and a smaller enclosed area susceptible to magnetic stray fields. The specific chip in figure 7.9 is set up for measuring a 5 µm thick Ag:Er sample with an erbium concentration of $x_{\mathrm{Er}} = 480\,\mathrm{ppm}$ (green), which we sputter-deposit on opposite coils. This requires the Wheatstone bridge to be covered symmetrically with 350 nm of SiO_2 (blue hatching). This galvanically decouples the sample material from the underlying niobium structures, while having a negligible noise contribution in cross-correlation mode.

The experiment holder of the silver set-up is the modified body of a C3NT 01 type noise thermometer [Fle20, Stä20]. A digital render in figure 7.10 shows the hardware as it sits in the cryostat on the right. In the center, the shield is removed to display further detail, with a zoomed section of the noise-o-meter and SQUID chips in the top left. The main body of the set-up (1) is based on a high purity (5N) silver cylinder with a diameter of 8 mm and a height of 50 mm. The upper half has a 1 µm

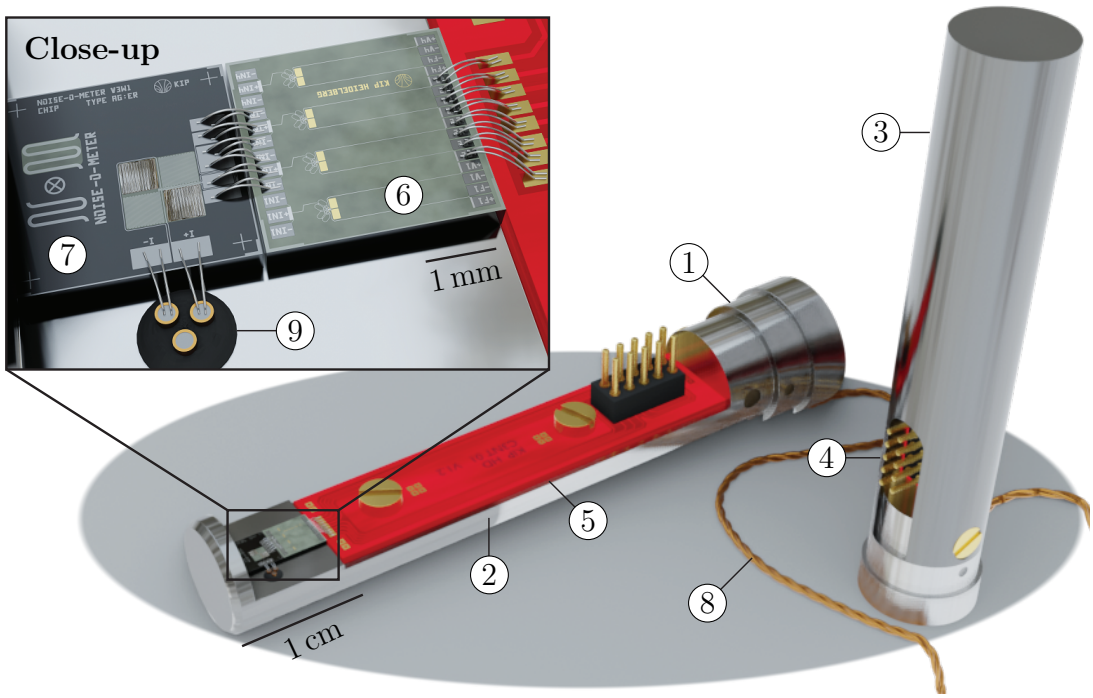

Figure 7.10: Digital render of the silver set-up. In the cryostat, we mount the experiment vertically and with a niobium shield, as is shown on the right. In the center, the shield is removed to show more detail. A zoom of the chips appears in the top left. We explain the different components (1) – (9) in the main text.

thick coating of superconducting niobium (2). This prevents electric Johnson noise from the silver coupling magnetically into our experiment. We shield from outside stray fields using a tight-fitting niobium shell (3). When performing a measurement, we attach the silver body directly to the mixing chamber platform of the cryostat, which results in excellent thermal contact. We then connect to the experiment via a 10-pin plug[4] (4). A circuit board (5) leads wiring to a front-end SQUID chip (6), which in turn sits in close proximity to the noise-o-meter chip (7). The driving current enters the experiment via superconducting wires made of a single core of Nb/Ti in a Cu/Ni matrix (8). We use two of the three wires of a twisted triplet, where one wire remains as back-up. The triplet initially runs along a groove in the back of the silver body, where it is embedded in a two-component epoxy resin[5]. It reaches the front via a through-hole (9). By bonding directly from the sanded ends of the individual wires to the noise-o-meter chip, we obtain a completely superconducting connection without any heating. The required SQUID amplifier

[4]cut from an SLR 2 050 G header by Fischer Elektronik GmbH & Co. KG. Nottebohmstraße 28, 58511 Lüdenscheid, Germany.

[5]LOCTITE®STYCAST 2850FT, Henkel AG & Co. KGaA, Henkelstraße 67, 40589 Düsseldorf, Germany.

modules are located in a separate housing (not shown here), which was previously used for noise thermometers [Stä20].

Overall, the silver set-up allows for high precision noise measurements of sample materials. In comparison to the copper set-up, it has better shielding from noise not originating from the sample, due to the niobium coating of the silver body underneath the SQUID and the noise-o-meter chip, and tight-fitting niobium shell. Additionally, the silver set-up can reach lower temperatures, due to improved thermal contact to the experimental platform of the cryostat and the alternating current running exclusively through superconducting wiring. Finally, by reducing the set-up to the strictly necessary components and operating only one Wheatstone bridge, it is more compact and easier to install.

7.3 Calibration

A number of characterizations of different hardware components are necessary, in order to perform the measurements we present in section 7.4. For cross-correlation mode, this encompasses the analog-to-digital converter, and an experimental determination of the cross-talk. We also introduce cuts for the time traces, which allow for even more accurate measurements even in noisy environments. Regarding susceptibility mode, we demonstrate a calibration of the lock-in amplifier, and a method for correcting for small manufacturing inaccuracies in the Wheatstone bridge. Finally, we perform thermalization measurements using the silver set-up.

7.3.1 Analog-to-digital Converter

One central piece of room-temperature hardware in cross-correlation mode is the analog-to-digital converter (ADC). In our set-up, we use a 16-channel SIS3316 digitizer card[6]. In the read-out chain, this device is attached to Magnicon XXF-1 SQUID Electronics[7] and translates the analog output of the electronics into digitized 16 bit integers. In the framework of noise-o-meter measurements, we performed a number of tests on the ADC, in order to make sure that the resulting noise spectra are accurate, reproducible, and consistent for different settings and across different hardware. We summarize our most important results here:

- The **input impedance** R_{ADC} of the ADC determines, together with the output impedance $V_{\mathrm{ce}} = 50\,\Omega$ of the SQUID FLL-electronics, the fraction $V_{\mathrm{ADC}}/V_{\mathrm{ce}} = R_{\mathrm{ADC}}/(R_{\mathrm{ADC}} + R_{\mathrm{ce}})$ of voltage that drops off over the ADC In 'high impedance

[6]Struck Innovative Systeme GmbH, Harksheider Str. 102, 22399 Hamburg, Germany.
[7]Magnicon GmbH, Barkhausenweg 11, 22339 Hamburg, Germany.

mode', in which we perform all our experiments, we measured $R_{\mathrm{ADC}} = 1080\,\Omega$ [Hen23], meaning that this fraction is only 96 %. In order for our results to be comparable to other hardware, we correct for this with a scaling factor 1/0.96 and thus plot the noise as if measured by an ADC with infinite input impedance.

- The **voltage range** of the ADC is the maximum voltage that is accurately converted into a 16 bit number, so the voltage that corresponds to a value of $2^{16} - 1$. While the manufacturer states two possible settings with voltage ranges of 2 V and 5 V, we measured these values to be 2.25 V and 5.2 V for our device [Hen23]. We use the former setting for our noise measurements. Not accounting for this fact would translates directly into a 12.5 % error in $\sqrt{S_V}$.
- The ADC converts the continuous input voltage into discrete voltage values representing individual time intervals with a certain **sampling rate**. Further averaging of multiple consecutive samples occurs, which we call **oversampling**. Finally, the **sample length** determines the length of the time trace. Our tests show that a variation of these three values yields consistent results. However, since these values influence the frequency interval we probe, noise from outside this frequency range can cause aliasing effects and lead to deviations of around 2 % at the overlap point of two noise spectra with different frequency ranges.

After applying appropriate corrections, we were able to verify that noise spectra taken with the ADC are consistent across different settings and that online evaluation using the measurement software PAQS[8] [Hen17] matches offline evaluation of time traces. Additionally, the spectra fulfill Parseval's theorem and match those obtained using a stand-alone network analyzer[9] to within the measurement accuracy of a few percent.

7.3.2 Quantization of Cross-talk

As we discuss in subsection 7.1.2, we are able to improve cross-correlated data by mathematically reducing the cross-talk. As a prerequisite, however, we must quantify the cross-talk ε. In a previous set-up involving cross-correlated noise read-out of a noise thermometer [Stä20], an experiment was suggested, in which one drives current through the feedback coil of the front-end SQUID and observes its cross-talk into the second read-out channel. This is done by switching off the SQUIDs in the first channel, meaning that FLL is disabled and no currents or voltages are applied to the SQUIDs. Hence, the front-end SQUID acts as a perfect flux transformer between its

[8] **P**arallel data **ac**q**u**isition **s**ystem, developed by Daniel Hengstler.

[9] SR770 FFT Analyzer from Stanford Research Systems, 1290-D Reamwood Avenue, Sunnyvale, CA, USA.

feedback and input coil. When applying a sinusoidal signal to the feedback coil of the front-end SQUID of this first channel, it couples via the SQUID washer into the input coil and reaches the second read-out channel, which is in its usual operational state. A comparison of the magnetic flux signal of the two SQUID channels then is a measure for the cross-talk. Performing such a measurement using the copper set-up does yield values compatible with the 2 % estimation in subsection 7.1.2.

However, this amount of cross-talk is only an upper limit, since during a real cross-correlated measurement, the front-end SQUID sits at its working point. It is not fully superconducting and the finite complex impedance of the Josephson junctions inhibits cross-talk. In fact, since the impedance is a function of the flux, we expect the actual cross-talk to be dependent on the precise state of the SQUID and thus not perfectly quantifiable. Thus, we only know that cross-talk is between 0 % and 2 % and we decide to choose a value of $(1 \pm 1)\,\%$ for our calculations. Two further points are of note:

- Since cross-talk originates from the feedback coil of the front-end SQUID, the signal that is fed back is the inverse of the original signal. This corresponds to an effective negative $\varepsilon = (-1 \pm 1)\,\%$ in equation (7.14). As a result, the cross-talk corrected data lies above the uncorrected data.

- In the silver set-up, we observe stronger cross-talk of $\varepsilon = (-6 \pm 1)\,\%$. This value is an estimation based on the fact that significant parts of the cross-correlated noise become negative when assuming a cross-talk with an absolute value less than 5 %, which would be unphysical. Since a measurement as mentioned above does not show this additional cross-talk, it must occur via a different channel than the input coils of the front-end SQUIDs. This topic is currently the main open question regarding noise-o-meter measurements and further discussions follow in section 7.5.

Overall, the large uncertainty in ε affects the accuracy of our data slightly, as is apparent in figure 7.6, where data appears for $\varepsilon = 0\,\%$ (red) and $\varepsilon = -1\,\%$ (green). We mention this uncertainty at the appropriate points in our discussion of data.

7.3.3 Time Trace Cuts

Prior to cross-correlation, we apply cuts to the time traces, similar to applying cuts to pulses during data evaluation for MMCs. We remove time traces with a large standard deviation, which is a sensitive test to find time traces with an overall drift, such as we would expect for operation during a change of the bath temperature. Similarly, we remove pulses with large peak-to-peak values, in order to not include

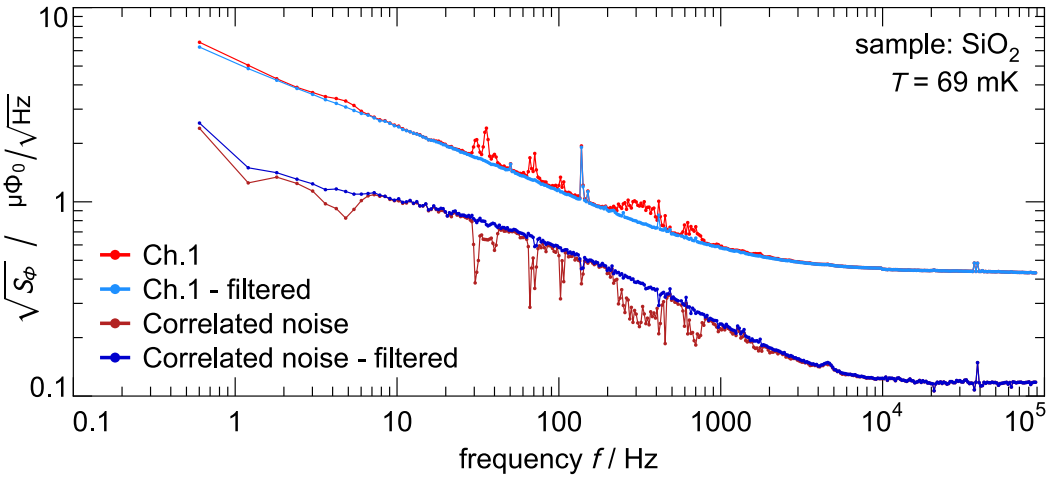

Figure 7.11: Comparison of data before (red) and after (blue) applying time trace cuts. The quality of the noise spectrum is greatly improved by this process. A small number of noise peaks remain, such as at 50 Hz and harmonics, as these are present in all time traces.

time traces containing down-mixed cell phone signals or cosmic rays impacting the set-up. Finally, we are also able to remove traces taken during certain time slots, such as a small window surrounding a particularly large disturbance. Note that these cuts only catch clear outliers, so that we are not artificially reducing the noise level of our measurement beneath that of an ideal unperturbed set-up.

Filtering time traces allows the noise-o-meter to obtain clean data in relatively noisy environments. Figure 7.11 shows a comparison from a measurement of SiO_2 using the copper set-up at 69 mK. Un-cut data from one read-out channel appear in bright red and contain a number of different peaks below 1 kHz. These do not vanish in the cross-correlated spectrum (dark red), since the noise originates from outside the experiment and couples into both channels similarly. However, after applying all cuts (blue), almost all peaks vanish, while the base noise spectrum remains unaffected. A few peaks remain, such as 50 Hz and harmonics as well as 140 Hz, caused by the rotary valve of the pulse tube cooler, since the corresponding noise is present in all time traces and is thus not removable using this method.

7.3.4 Lock-in Amplifier

The main piece of hardware we use for susceptibility mode is the lock-in amplifier[10]. In order to measure phase shifts with sub-degree accuracy, we perform a calibration measurement. Using the internal signal generator, we send a signal to the feedback

[10]Signal Recovery 7265 DSP Lock-In Amplifier, AMETEK GmbH, Rudolf-Diesel-Straße 16, 40670 Meerbusch, Germany.

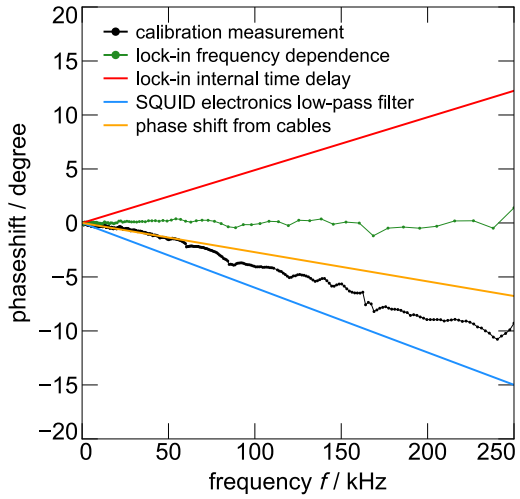

Figure 7.12: Sources of phase shift in susceptibility mode originating from the experimental set-up. The calibration measurement in black is the sum of four different components.

coil of one of the front-end SQUIDs and record the phase shift θ with respect to the output signal for different signal frequencies. Results appear in black in figure 7.12, where a negative phase shift corresponds to the signal returning from the SQUID lagging behind the original signal. Two things become apparent: First, the phase shift is roughly proportional to the frequency. Second, on top of this proportionality, there is a non-trivial frequency dependence in the order of a few degrees. Our analysis shows that the observed behavior is the sum of four different effects:

- We trace the complex frequency dependence to the electronics in the lock-in amplifier, since the same frequency dependence appears when directly connecting the output of the lock-in's signal generator to it's input (green). This is a consistent, reproducible, frequency-dependent phase shift across all our measurements.

- Within the lock-in's electronics, we find a time delay causing the signal from the internal signal generator to lag behind the signal returning from the experiment by 136 ns (red). This causes an effective positive phase shift.

- The SQUID electronics have a bandwidth of 6 MHz, which we model as a 6 MHz low-pass filter (blue)[11].

- Cabling causes a finite time delay. We estimate the experiment to have a total of 5 m of twisted pair Cu/Ni cable within the cryostat, and 5 m of cabling at room temperature. The former has an impedance of about 120 Ω, from which we estimate an inductance of $L_{\mathrm{tp}} = 19\,\mathrm{nH}$. This results in a phase shift of $\theta_{\mathrm{tp}} = 2\pi \tan^{-1}(2\pi f L_{\mathrm{tp}}/R_{\mathrm{tp}})$, where $R_{\mathrm{tp}} \approx 7\,\Omega$ is the resistance of the twisted

[11] We model the SQUID electronics as a low-pass filter of first order, which, for $f \ll 6\,\mathrm{MHz}$ is a good approximation of the electronics' more complex frequency cut-off.

pair inside the cryostat. For the 50 Ω coaxial cable at room temperature, we measure a transmission speed of $0.67\,c$ (with the speed of light c), leading to a phase shift of $2\pi f \cdot 5\,\mathrm{m}/c$. The sum of these two components appears in yellow in figure 7.12.

When adding all components, we obtain an overall phase shift matching the calibration measurement in black. We conclude that we have a good understanding of the origin of the measured phase shift and are confident in correcting data accordingly. Additionally, we perform a similar calibration for the relative amplitude, but the effects on the data are less pronounced.

We briefly mention a number of lock-in-specific settings relevant for our measurements. Most important is the integration time, which we set to be between $2/f$ and $10/f$, but at least 2 s. This ensures an accurate measurement [Rei12]. Furthermore, our tests show that we achieve best resolution when operating the lock-in amplifier in SignalReference and DC mode for $f < 1\,\mathrm{kHz}$, and in VoltMeterMode and AC mode for $f \geq 1\,\mathrm{kHz}$. We refer the reader to documentation for detailed information on these settings [Rec02]. The small discontinuity in $\hat{I}_\mathrm{i}/\hat{I}_0$ of the order of 0.1 % at $f = 1\,\mathrm{kHz}$ vanishes after the calibration. Regarding the driving current I_0, a higher value leads to improved accuracy. However, we must also make sure that no heating effects influence our results and that the slew rate of the SQUID's FLL electronics can follow fast enough not to produce artifacts. For different samples, we choose values between 1 µA and 50 µA.

7.3.5 Asymmetry of the Wheatstone Bridge

Variations in the manufacturing process cause the meander-shaped coils to have slightly different inductances. As a result, a finite fraction of the current I_0 flows through the input coils of the SQUIDs, even when operating without a sample material. This asymmetry is unique for each individual chip and we must correct for it, since it influences the measured χ'. For this reason, we use a Curie-Weiss fit, which is a good approximation for the susceptibility of paramagnetic materials with interacting magnetic moments, to extrapolate the measured χ' to $1/T \to 0$. In this limit, the susceptibility of our sample materials is reduced to a negligible diamagnetic component, and most of the remaining χ' must be due to asymmetry. Simply subtracting this value from our data gives us the accurate susceptibility of the sample.

7.3.6 Thermalization of the Silver Set-up

As previously done for the copper set-up in subsection 4.2.2, we must analyze the thermalization behavior of the silver set-up. Due to flux quantization and conser-

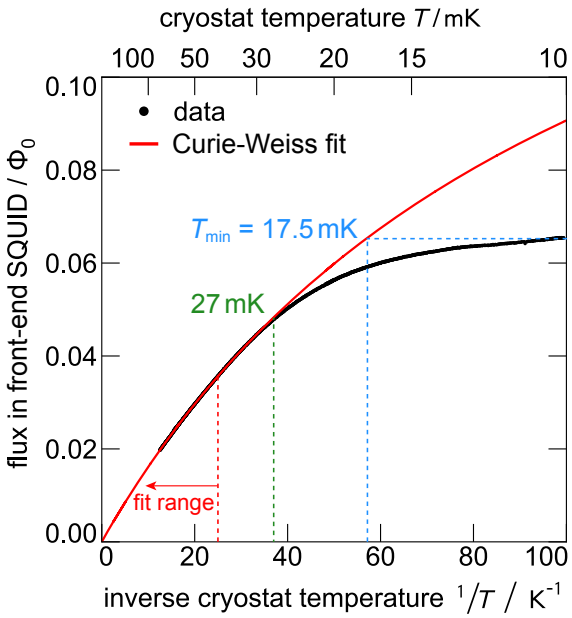

Figure 7.13: Results of a thermalization measurement using the silver set-up. Above 27 mK, the fit (red) in equation (7.22) describes data (black) to within 1 %. The lowest temperature we reach is $T_{\mathrm{min}} = 17.5\,\mathrm{mK}$.

vation in closed superconducting loops, any stray magnetic field present in the experiment as superconductivity establishes itself at $T = T_{\mathrm{c}}$ causes shielding currents within the circuit. This includes current along the path leading through the input coils of the front-end SQUIDs[12]. Without supplying an AC signal, we log the output of a noise-o-meter with a Ag:Er sample while varying the temperature T of the cryostat. Due to flux conservation, the temperature dependence of the susceptibility of the Ag:Er changes the current I_{i} that flows through the input coils of the front-end SQUIDs. Using Kirchhoff's laws, we find

$$I_{\mathrm{i}} = \frac{a}{L_0 + L} + b = \frac{a}{2L_0 + \chi' F L_0} + b \quad , \tag{7.22}$$

where a and b are unknown constants that depend on the flux penetrating the experiment during cool-down. We then approximate χ' with a Curie-Weiss law, which is a good approximation for paramagnetic samples with interacting magnetic moments. A full simulation of the magnetization, as done for Quasy-maXs in figure 4.3, is not easily possible, due to the unknown magnetic field permeating the sample. In figure 7.13, we fit the resulting function (red) to data (black) for $T > 40\,\mathrm{mK}$. Down to 27 mK, the fit matches data to within 1 %, suggesting that the temperature of the experiment matches T. The deviation at lower temperatures is consistent with lacking thermalization. At lowest cryostat temperatures, we estimate the experiment to have a temperature of $T_{\mathrm{min}} = 17.5\,\mathrm{mK}$.

[12] During normal operation we do not measure this current, since SQUIDs are only sensitive to changes in flux.

We conclude that when using the silver set-up, we are able to take reliable data down to 27 mK, which is significantly lower than the 54 mK we reach with the copper set-up (see subsection 4.3.2). Since for similar hardware, noise decoupling of the silver body occurs at 300 µK [Stä20, Fle20], we believe that the thermal link between the noise-o-meter chip and the silver body is the limiting factor. This is plausible, since thermal contact is only of phononic nature. As a final note, we do not observe any heating when applying an AC signal in susceptibility mode, since the wires made of Nb/Ti in Cu/Ni and the entire signal path within the niobium shield is superconducting.

7.4 Experimental Results

We present here the results of experiments on three different materials commonly used in MMCs: Au:Er, Ag:Er, and SiO_2. In the following, we briefly introduce all three samples and compare their noise spectra at a low temperature. There follows a detailed analysis on each sample individually, including the temperature dependence of the noise. At the end, we interpret the real part of the susceptibility and introduce a model based on Debye relaxators. Note that when mentioning temperatures in this section, we always refer to the temperature of the experiment that we deduce from the cryostat temperature based on the thermalization curves in figures 4.3 (copper set-up) and 7.13 (silver set-up).

7.4.1 Overview of Noise Data

In figure 7.14 appears an overview of the measured noise of all three samples at a temperature of $T = 43\,\mathrm{mK}$. We show data obtained in cross-correlation mode (dots) and data obtained in susceptibility mode (squares). As we discuss in subsections 7.1.2 and 7.1.3, the former is a measure for the overall noise in the noise-o-meter, not including read-out noise. The latter measures only the magnetic flux noise of the sample material. On the additional y-axis, we express the magnetic flux in the front-end SQUID in units of the SQUIDs energy sensitivity $\varepsilon_\mathrm{s} = \frac{S_\Phi}{L_\mathrm{s}}$ with the washer inductance $L_\mathrm{s} = 60\,\mathrm{pH}$. This shows the sensitivity of the noise-o-meter, in that we are able to measure noise beneath the quantum noise limit $\varepsilon_\mathrm{s} \leq \hbar/2$ of a front-end SQUID, which is the theoretical resolution limit of a standard noise measurement using a dc-SQUID in single channel mode, which has by far not been reached yet.

Au:Er. Noisiest of the three samples is the gold erbium alloy, which we deposited on the noise-o-meter in a sputtering process. With a stylus profilometer[13], we determine

[13]DektakXT from Bruker Corporation, 40 Manning Rd, Billerica, MA 01821, USA.

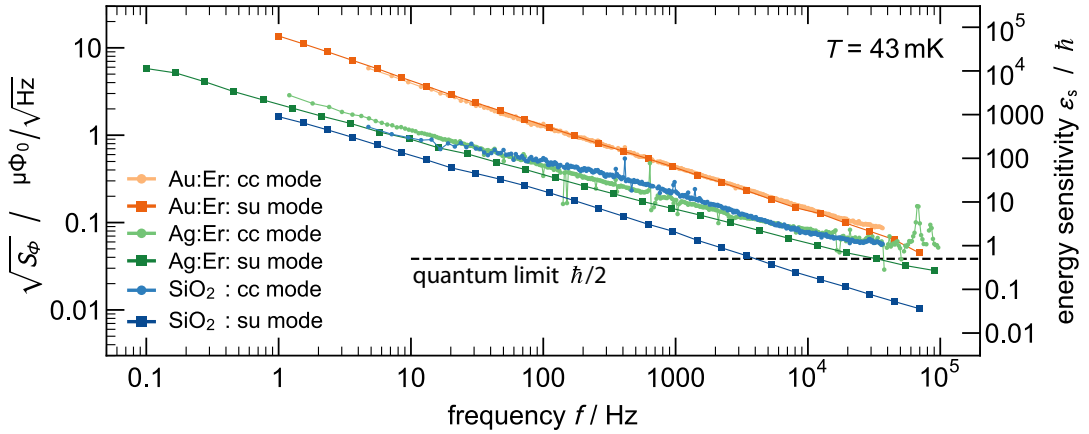

Figure 7.14: Noise caused by the Au:Er (orange), Ag:Er (green), and SiO_2 (blue) samples at $T = 43\,\mathrm{mK}$. Dots represent the overall noise of the Wheatstone bridge measured in cross-correlation mode, while squares show the magnetic flux noise measured in susceptibility mode.

the Au:Er film to have a thickness of 2.58 µm. Magnetization measurements with a commercial magnetometer[14] at $2\,\mathrm{K} \leq T \leq 300\,\mathrm{K}$ and $B = 1\,\mathrm{T}$ result in an erbium concentration of $x_{\mathrm{Er}} = (2480 \pm 10)$ ppm. The latter is close to the erbium concentrations in the sensor material of Quasy-maXs (2660 ppm) and Hot-maXs (2490 ppm). We thus expect our results to be representative and immediately transferable to both of our MMCs. Looking at the data, we see that both measurement modes produce almost identical results. We conclude that for this sample, the overall noise in the circuit consists almost entirely of the sample's magnetic flux noise. Indeed, for such a highly paramagnetic material, we expect the sample to dominate. In this regard, the data confirm the functionality of the noise-o-meter. A detailed analysis follows in subsection 7.4.2.

Ag:Er. Using the silver set-up, we measure the noise of a silver erbium sample with a film thickness of 4.73 µm and an erbium concentration of (480 ± 10) ppm. Similar alloys find application as a temperature sensor in many different experiments [Boy18, Rei20, Sik20, Kim21], so a quantitative analysis of the magnetic flux noise is of great interest. In general, we see a similar picture to the Au:Er sample, in that the overall noise is dominated by magnetic flux noise caused by the sample. At frequencies above 10 kHz, an additional white noise component is visible in the cross-correlated data, which we attribute to Johnson noise of the sample. We discuss this further in subsection 7.4.3.

[14] QD MPMSR XL by Quantum Design GmbH, Im Tiefen See 58, 64293 Darmstadt, Germany.

SiO_2. A different picture presents itself in the case of SiO_2. This material is used in many microstructured devices as an insulating layer, so too in Quasy-maXs and Hot-maXs. Again, in order to obtain a result applicable to our MMCs, we perform the noise measurement using the copper set-up. The thickness of the SiO_2 is 440 nm. However, for this sample, we leave two square holes in the wafer-wide SiO_2 layer over two opposite meander coils, instead of depositing the sample on the Wheatstone bridge. For susceptibility mode, this is equivalent, as the same asymmetry is created either way. In cross-correlation mode, we must consider contributions from sample material in areas other than the Wheatstone bridge, such as the areas enclosed by the wiring between the meanders of the bridge and the input coils of the front-end SQUIDs. Looking at the data, we see a clear disparity between the measurement modes. In fact, the sample's magnetic flux noise is mostly a negligible component in the overall noise in the circuit. The significantly lower level of magnetic flux noise is not surprising, since in comparison to the other samples, the SiO_2 does not contain a large amount of strongly magnetic erbium. We measure here only dangling bonds and impurities, such as trace magnetic ions from the sputtering process. We attribute the additional noise in cross-correlation mode to symmetrically distributed sample material and magnetically coupled Johnson noise, with further detail following in subsection 7.4.4.

7.4.2 Noise of Au:Er

In our quantitative analysis of the Au:Er data, we begin with the previously presented measurement at $T = 43\,\mathrm{mK}$, which appears in pale orange and pale blue in figure 7.15. As discussed, cross-correlation mode and susceptibility mode yield similar results and we conclude that almost the entire noise in the Wheatstone bridge is magnetic flux noise from the erbium. The noise follows a $1/f$-like shape, matching the erbium noise previously observed in MMCs [Fle03, Dan05, Pie12]. A fit of the form $S_{\Phi_{\mathrm{Er}}}(f) = S_{\Phi_{\mathrm{Er}}}(1\,\mathrm{Hz})\,(f/\mathrm{Hz})^{\alpha}$ to the noise measured in susceptibility mode matches data well and appears in black. As fit parameters, we find $\sqrt{S_{\Phi_{\mathrm{Er}}}(1\,\mathrm{Hz})} = (13.1 \pm 0.4)\,\mu\Phi_0/\sqrt{\mathrm{Hz}}$ and $\alpha = -1.00 \pm 0.03$, where the uncertainties are based on fits to multiple measurements between 40 mK and 60 mK, as well as uncertainty regarding the precise temperature of the experiment. Note that an inaccurate value for the temperature directly impacts the noise amplitude in susceptibility mode, since according to equation (7.21), $\sqrt{S_\Phi} \propto \sqrt{T}$.

In order to transfer the measured erbium noise to Quasy-maXs, Hot-maXs, and other devices, we must normalize our data by the amount of erbium and the geometry of

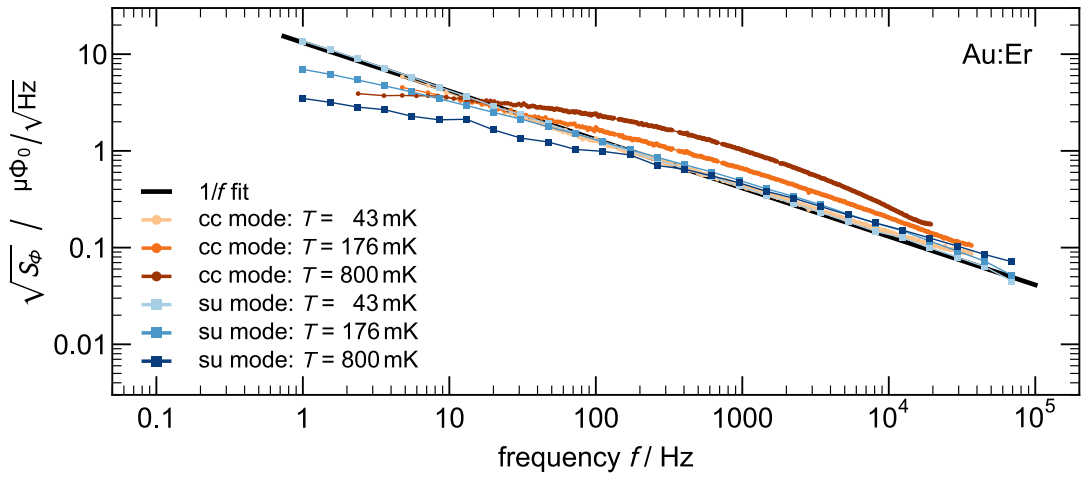

Figure 7.15: Data of noise measurements on Au:Er using cross-correlation mode (orange circles) and susceptibility mode (blue squares). At low temperatures, data of the two modes match well, and are well described by a $1/f$ fit (black). At high temperatures, the kinetic inductance of the aluminum bonds, and magnetic Johnson noise influence results.

the noise-o-meter. Following equation (6.12), the erbium noise is

$$S_{\Phi,\mathrm{Er}}(f) = 2 \cdot \left(\frac{\delta\Phi_{\mathrm{s,m}}}{\delta\Phi_{\mathrm{m}}}\right)^2 \cdot \frac{\mu_0^2\langle G^2\rangle}{p^2}\, N_{\mathrm{Er}}\, S_{\mathrm{m},1/f}(1\,\mathrm{Hz}) \cdot \left(\frac{f}{1\,\mathrm{Hz}}\right)^{\alpha} \quad , \tag{7.23}$$

where the additional factor of 2 is necessary, since we have two sample-covered coils in parallel. Furthermore, the flux coupling factor $\delta\Phi_{\mathrm{s,m}}/\delta\Phi_{\mathrm{m}} = (0.96 \pm 0.03)\,\%$ between the SQUID and a meander coil based on equation (7.11) translates the magnetic flux noise in the meander coil into flux noise in the front-end SQUID. The uncertainty originates from uncertainties of the involved inductances. Using finite element methods (see section 3.1), we find $\langle G^2\rangle = 0.27$. The pitch p is 10 µm, and the number of erbium ions, as determined from concentration and volume, is $N_{\mathrm{Er}} = 9.44 \times 10^{13}$. These quantities have negligible uncertainties. Inserting our fit parameters, we find the important result

$$S_{\mathrm{m},1/f}(1\,\mathrm{Hz}) = (0.115 \pm 0.006)\,\frac{\mu_{\mathrm{B}}^2}{\mathrm{Hz}} \quad \text{and} \quad \alpha = -1.00 \pm 0.03 \tag{7.24}$$

for the erbium noise of high concentration Au:Er at low temperatures. The quantity $S_{\mathrm{m},1/f}(1\,\mathrm{Hz})$ represents the magnetic flux noise per erbium ion, where μ_{B} is the Bohr magneton. Our result matches an unpublished value of $\sim 0.12\,\mu_{\mathrm{B}}^2/\mathrm{Hz}$ [Hof12], and is slightly higher than the previous best estimate of $\sim 0.1\,\mu_{\mathrm{B}}^2/\mathrm{Hz}$ [Fle09a], but likely lies within the error margin of that measurement.

We now consider data at higher temperatures. In cross-correlation mode, we observe an additional temperature-dependent noise component between 10 Hz and 10^4 Hz with a characteristic low-pass shape. We attribute this to magnetic Johnson noise caused by the experimental holder, generating fluctuating magnetic fields in the area enclosed by the bonding wires between the noise-o-meter and the front-end SQUIDs. Since this noise component is more clearly visible in the SiO_2 data, we defer a discussion to subsection 7.4.4. Regarding Johnson noise from the sample material itself, we would expect a white noise component with an amplitude of $0.019\,\mu\Phi_0/\sqrt{\text{Hz}}$, according to equation (6.9). This is obscured by erbium noise.

The noise measured in susceptibility mode is almost temperature independent for $f > 10\,\text{Hz}$ and $T \leq 176\,\text{mK}$. This is in accordance with previous measurements, which found erbium noise to be temperature independent up to 4.2 K [Fle03]. We do, however, see a temperature dependence at low frequencies and high temperatures. The kinetic inductance of the aluminum bonding wires is a likely cause, which can become relevant above roughly $T_c/10 = 120\,\text{mK}$. A potential upgrade to the noise-o-meter, in which niobium bonding wires replace the aluminum wires, could diminish this effect, since the critical temperature of niobium is larger by a factor of eight.

7.4.3 Noise of Ag:Er

In the framework of the Bachelor's thesis of *Rui Yang* [Yan23], we have measured the noise of a Ag:Er sample using the silver set-up. The corresponding data appear in figure 7.16. At $T = 23\,\text{mK}$, data obtained in susceptibility mode (blue) follow a general $1/f$-like shape. Since we expect erbium noise to dominate the magnetic flux noise, this is not surprising. A fit (black) as in equation (7.23) describes the data well. The sample height of 4.73 µm, erbium concentration of $x_{\text{Er}} = 480\,\text{ppm}$, and 420 nm thick insulating SiO_2 layer, results in $\langle G^2 \rangle = 0.17$ and $N_{\text{Er}} = 3.5 \times 10^{13}$. The flux coupling factor $\delta\Phi_{\text{s,m}}/\delta\Phi_{\text{m}} = (1.02 \pm 0.03)\,\%$ is slightly altered, due to shorter bonding wires. We find fit values of

$$S_{\text{m},1/f}(1\,\text{Hz}) = (0.0175 \pm 0.0009)\,\frac{\mu_{\text{B}}^2}{\text{Hz}} \quad \text{and} \quad \alpha = -0.856 \pm 0.014 \tag{7.25}$$

for low-concentration Ag:Er at MMC-typical temperatures of 21 mK to 31 mK. A slight temperature dependence in the data is further explored elsewhere [Yan23].

These results are incompatible with results obtained for Au:Er, both here as well as in literature [Fle09a], where a 6.6-fold higher noise per erbium ion at 1 Hz was found. We conclude that the current model of erbium noise does not apply to our Ag:Er sample. An explanation of our results becomes possible with additional information on the dynamics of the magnetic moments, which we discuss in subsection 7.4.7.

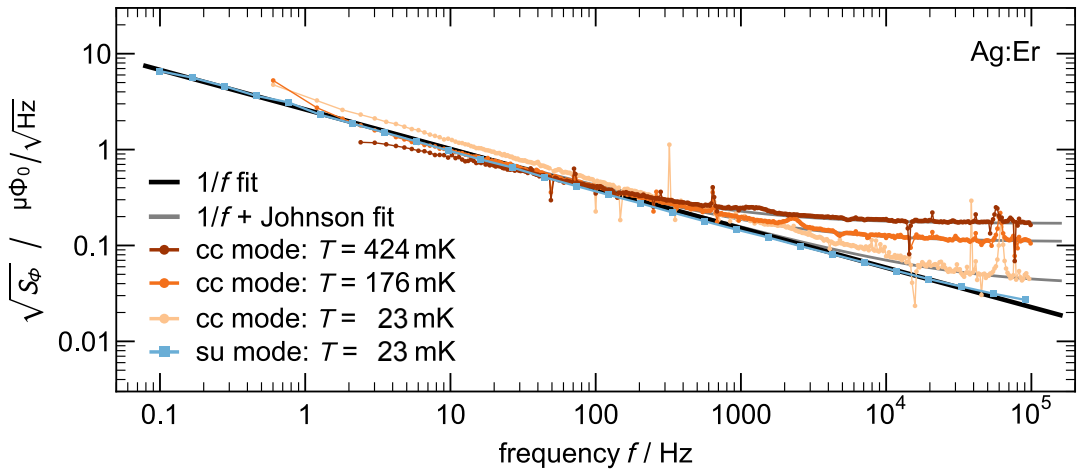

Figure 7.16: Results of noise measurement on a Ag:Er film using the silver set-up. Data from susceptibility mode (blue) follow a $1/f$ shape (black), while data from cross-correlation mode (orange) feature an additional white noise component. A sum of erbium noise and Johnson noise from the sample describes data well (gray).

For now, we continue with data obtained with cross-correlation mode, which appear as circles in figure 7.16. Comparing data at $T = 23\,\text{mK}$ to those from susceptibility mode for $f < 5\,\text{kHz}$, we see that the slope is identical. This suggests that in this region, magnetic flux noise is the only relevant noise component. However, data from cross-correlation mode lie $\sim 25\,\%$ higher than data from susceptibility mode. This is likely in part magnetic flux noise from the symmetrically distributed insulating SiO_2 layer between meander coils and sample. As we show in the following subsection 7.4.4, such a noise component has a similar slope of $\alpha = -0.88$. However, we cannot exclude that some of this difference may also originate from the abnormally high cross-talk we observe for the silver set-up, which we are not able to account for perfectly using mathematical cross-talk correction. We believe that a slightly different cross-talk model from that described by equation (7.13) may lead to more accurate results, but this would require a better understanding of potential cross-talk paths. Currently, the topic of cross-talk is the largest potential area of improvement for the silver set-up, and we discuss our plans in this regard in section 7.5.

One important observation we make for data from cross-correlation mode at medium frequencies of 10 Hz – 1 kHz is that the additional noise component seen in Au:Er data is not present. For samples measured with the copper set-up, we attribute such a component to Johnson noise from the experimental platform. In contrast to the copper set-up, the silver set-up features an additional layer of superconducting niobium, specifically to suppress any magnetic coupling between the experiment and the metal beneath. Our data show that the procedure of niobium coating is effective

in reducing magnetic Johnson noise, and confirm that in the other two samples, such noise does indeed arise from the copper beneath the chip.

At high frequencies, above 1 kHz, an additional white noise component appears in data obtained in cross-correlation mode. We believe this to be in part electric Johnson noise of the sample, which couples magnetically into the meander-shaped coil beneath. Equation (6.9), which is based on simulations [Pie12], gives us an estimate for the expected amplitude of such a noise component. We insert $A = 2 \cdot (500\,\mu\text{m})^2$, $p = 10\,\mu\text{m}$, $z = 350\,\text{nm}$, and $d = 5\,\mu\text{m}$, as well as $\rho = 11.4 \times 10^{-9}\,\Omega\text{m}$ for sputtered Ag:Er with $RRR = 2.4$ [Hen17]. However, we must include an additional factor of 2.0, so that when adding this component to the $1/f$ noise discussed above, we obtain the gray lines in figure 7.16, which describe data well. This factor of two might come from an incorrect cross-talk estimation, or from an inaccuracy in the derivation of equation (6.9). However, we can be sure that this white noise is at least in part of physical nature, as supported by its temperature dependence.

Since present MMCs comprise a paramagnetic sensor sitting on top of a meander-shaped pick-up coil in just this way, this noise component is present in all MMCs. However, since white SQUID noise is typically dominant at high frequencies, Johnson noise from the sensor is typically hidden. Our data is, to our knowledge, the first time this noise component has been observed.

7.4.4 Noise of SiO_2

As a final sample, we present here results from measurements on SiO_2. Data from susceptibility mode at $T = 43\,\text{mK}$ appear in blue in figure 7.17. As seen for the other samples, the magnetic flux noise has a $1/f$-like shape, and is well described by a fit of the form $S_{\Phi_{SiO_2}}(f) = S_{\Phi_{SiO_2}}(1\,\text{Hz})\,(f/\text{Hz})^{\alpha}$ (black). The fit parameters are $\sqrt{S_{\Phi_{SiO_2}}(1\,\text{Hz})} = 1.65\,\mu\Phi_0/\sqrt{\text{Hz}}$ and $\alpha = -0.88$. If we assume that the magnetic flux noise originates from erbium with $S_{\text{m},1/f}(1\,\text{Hz}) = 0.115\,\frac{\mu_B^2}{\text{Hz}}$ we can calculate an effective erbium concentration using equation (6.12). With a sample height of 440 nm and $\langle G^2 \rangle = 0.81$, we find an atomic concentration of 57 ppm erbium-equivalent impurities. More likely, however, is that the magnetic impurities consist mainly of dangling bonds. To first order, the impurity concentration then scales with the ratio of the impurities' magnetic moments. For example, if attributing the noise to dangling bonds with spin 1/2 and a g-factor of 2, instead of Er^{3+} with $\tilde{S} = 1/2$ and $\tilde{g} = 6.8$ (see section 2.2), the concentration is around 200 ppm. We believe that with this measurement, we are around a factor of three above the resolution limit of susceptibility mode, as determined by calibration measurements. At temperatures around $\sim 70\,\text{mK}$, we are no longer able to measure magnetic flux noise of SiO_2.

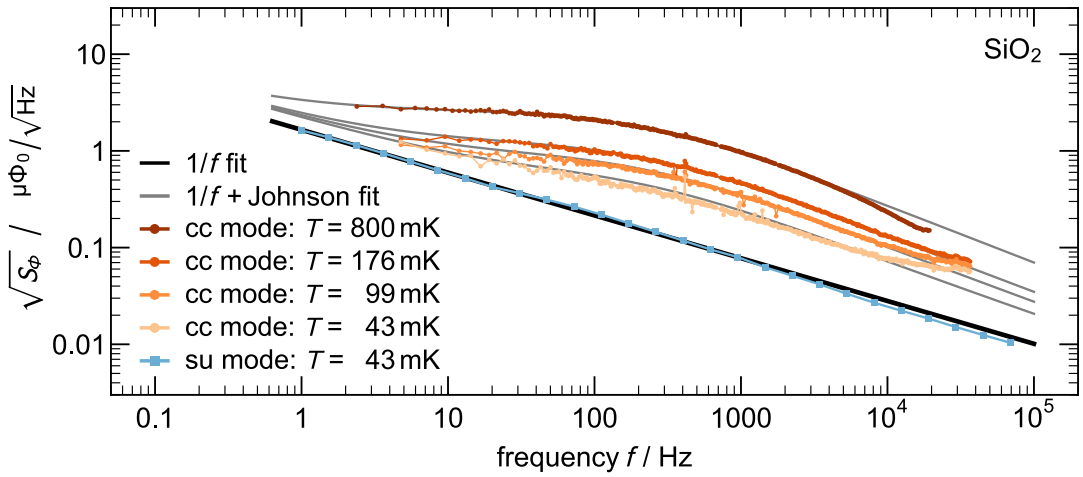

Figure 7.17: Measured noise of an SiO_2 sample. Low temperature data from susceptibility mode (squares) follow a $1/f$ shape (black). Noise data from cross-correlation mode (dots) are well described by a combination of $1/f$ noise and magnetically coupled Johnson noise for all temperatures.

Data from cross-correlation mode (orange) feature an additional noise component, which is especially prevalent between 10 Hz and 10^4 Hz. We believe this to be magnetic Johnson noise caused by the copper experimental holder generating fluctuating magnetic fields in the area enclosed by the bonding wires between the noise-o-meter chip and the front-end SQUID chip, but mitigated by the skin effect. A number of qualitative arguments support this theory:

- According to equation (6.6), electric **Johnson noise** scales with $S \propto T$. The data in figure 7.17 shows the same scaling. Furthermore, this type of noise is known to couple magnetically into superconducting microstructures [Ens00, Bey07], and we are susceptible to it in cross-correlation mode, but not in susceptibility mode.

- The copper **experimental holder** is the most likely source of the Johnson noise, since we observe almost identical noise in our Au:Er measurements (see figure 7.15), in which we use the same copper holder. We do not, however, see it in the silver set-up (see figure 7.16), which features a superconducting niobium layer deposited on the main silver body, preventing magnetic coupling.

- The **skin effect** explains the low-pass behavior of the observed noise component. Matching our data, it is independent of temperature.

- We believe that the noise couples magnetically via the **bonding wires** to our experiment. According to equation (6.9), direct coupling to the Wheatstone

bridge's meander coils would be too weak, due to their highly gradiometric geometry. We excluded coupling to a different part of the noise-o-meter chip in an additional experiment, in which we deposited a superconducting niobium layer on the back of a noise-o-meter chip. This did not remove the additional noise component. Noise coupling to the front-end SQUIDs, or to a device later in the read-out chain, would not be visible in cross-correlation mode. This leaves the bonding wires, which enclose a comparatively large area and are thus a likely candidate.

Following derivations in literature [Var84, Rot98], we fit our data with a function of the form

$$\begin{aligned}\sqrt{S_{\Phi,\mathrm{fit}}(f,T)} &= \sqrt{S_{\Phi,\mathrm{J}}(f) + S_{\Phi,1/f}(f)} \\ &= \sqrt{A_\mathrm{J}^2 \frac{T}{1\,\mathrm{K}} \left(1 + \frac{2\,f}{\pi f_\mathrm{c}}\right)^{-\gamma} + S_{\Phi,1/f}(1\,\mathrm{Hz})/f^{0.88}} \quad .\end{aligned} \tag{7.26}$$

This formula is a combination of Johnson noise $S_{\Phi,\mathrm{J}}$ with a plateau noise level defined by A_J^2, a low-pass with a cutoff frequency f_c and exponent γ due to the skin effect, and a $1/f$ component $S_{\Phi,1/f}$. Regarding the $1/f$ component, we fix the exponent to $\alpha = -0.88$, which we measured above for the magnetic flux noise of SiO_2. The amplitude, however, may differ and remains a fit parameter, since any symmetric distribution of SiO_2 contributes in cross-correlation mode, but not in susceptibility mode. Our fit parameters are $A_\mathrm{J} = 2.9\,\mu\Phi_0/\sqrt{\mathrm{Hz}}$, $f_\mathrm{c} = 143\,\mathrm{Hz}$, $\gamma = 1.19$, and $\sqrt{S_{\Phi,1/f}(1\,\mathrm{Hz})} = 2.16\,\mu\Phi_0/\sqrt{\mathrm{Hz}}$. Inserting these values into equation (7.26), together with temperatures of 43 mK, 99 mK, 176 mK, and 800 mK, results in the gray curves, which match our data well for $f \leq 10^4\,\mathrm{Hz}$.

We briefly verify that these values are consistent with our theory stated above. Inserting the cut-off frequency into equation (6.11) describing the characteristic skin depth δ, we find $\delta = 0.42\,\mathrm{mm}$, when assuming an electric resistivity $\rho_\mathrm{Cu} = 10^{-10}\,\Omega\mathrm{m}$ ($RRR \approx 150$) for copper. The thickness of the copper holder is $d = 3.3\,\mathrm{mm}$ at the position the chips are glued to. Considering that a drop-off in noise starts at frequencies below f_c, the explanation of skin-depth limited noise is feasible. However, at similar frequencies, we also expect to be limited by the extent of the respective noise current modes [Bey07], but this effect is hard to quantify at $z \approx \delta$, where $z \approx 300\,\mu\mathrm{m}$ is the distance between the copper platform and the bonding wires. Overall, both the cut-off frequency and the exponent γ are comparable to noise found in a similar set-up [Bey07].

Regarding the low frequency limit of this noise, we expect, according to equation (6.10), an amplitude of

$$\sqrt{S_{\Phi,\mathrm{J}}(1\,\mathrm{Hz})} = A_\mathrm{J}\sqrt{\frac{T}{1\,\mathrm{K}}} = \frac{\delta\Phi_\mathrm{s}}{\delta\Phi_\mathrm{exp}}\sqrt{\frac{\mu_0^2 k_\mathrm{B} T\sigma d}{8\pi z^2}\cdot A^2} \quad . \tag{7.27}$$

Here, the coupling factor translates flux Φ_exp coupling into the relevant part of the experiment, in this case the superconducting loop including the bonding wires, to flux Φ_s in a front-end SQUID. Mathematically, this is the same value of 2 % that we calculate in subsection 7.1.2 for cross-talk between read-out channels. The only unknown at this point is the effective area A of the bonding wires. Note that we must only consider the area between the two central bonds, since the gradiometric layout causes flux in other areas to cancel out. A reasonable value of $A = 70\,\mu\mathrm{m} \times 240\,\mu\mathrm{m}$ results in the observed $A_\mathrm{J} = 2.9\,\mu\Phi_0/\sqrt{\mathrm{Hz}}$.

Finally, the $1/f$ noise component we observe in cross-correlation mode is slightly higher than in susceptibility mode. This suggests additional $1/f$ noise with an amplitude of $\sim 1.4\,\mu\Phi_0/\sqrt{\mathrm{Hz}}$ originating from symmetrically distributed material.

Above 10^4 Hz, we observe an apparent white noise component, which is in the order of $0.04\,\mu\Phi_0/\sqrt{\mathrm{Hz}}$. Unlike the similar noise we observe for Ag:Er, this component is temperature independent and thus unlikely to be some form of Johnson noise. Instead, we believe this to result from an inaccurate estimation of the cross-talk $\varepsilon = -1\,\%$, which affects low noise data strongest. Interestingly, choosing a value of $\varepsilon = 0$ results in data matching the fit almost perfectly. However, we have no method of confirming that cross-talk is indeed negligible and choose to display the more conservative estimate of $\varepsilon = -1\,\%$ here.

7.4.5 Real Part of the Susceptibility of SiO_2

Of the data we measure in susceptibility mode, we have, so far, only considered the imaginary part χ'' of the complex AC susceptibility. However, the real part χ' is of great interest as well, as we demonstrate in this section. Since we only obtain $\chi' F$ from equation (7.17), the first step is to calculate the filling factor F, which is the fraction of the magnetic field energy E_mag inside the sample volume with respect to the total magnetic field energy. Using finite element methods we discuss in section 3.1, we simulate a test current I flowing through a meander coil with inductance L_0 and calculate the resulting magnetic field distribution $B(\vec{x})$. With

$$F = \frac{E_\mathrm{mag,\,sample}}{E_\mathrm{mag,\,total}} = \frac{\int_{V_\mathrm{sample}} \frac{1}{2}\frac{B^2}{\mu_0}}{\frac{1}{2}L_0 I^2} \quad , \tag{7.28}$$

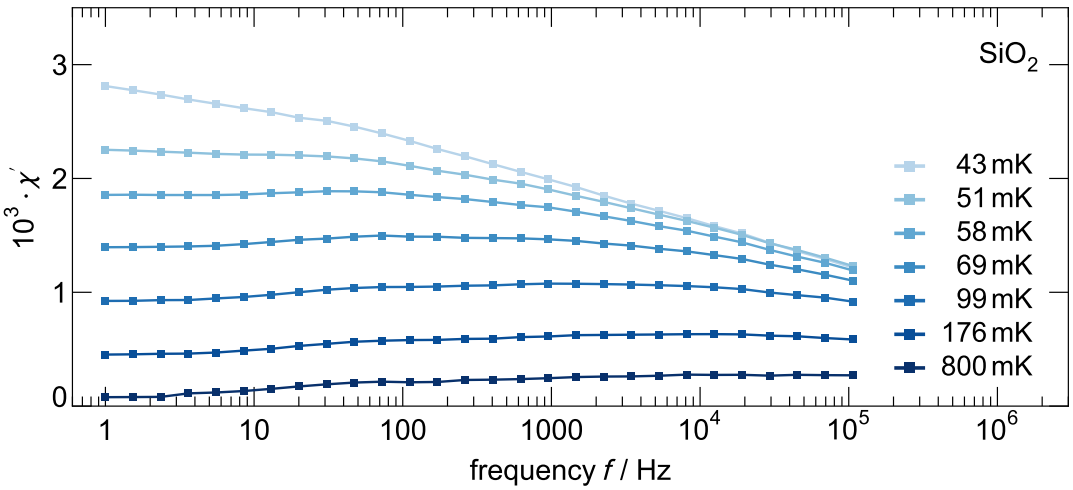

Figure 7.18: Real part of the susceptibility of SiO_2 as a function of frequency and temperature.

we find filling factors of $F_{\mathrm{Au:Er}} = 31.7\,\%$, $F_{\mathrm{SiO_2}} = 16.5\,\%$, and $F_{\mathrm{Ag:Er}} = 38.0\,\%$. As a result, we are able to calculate the real part χ' of the susceptibility.

We begin our analysis of χ' with data for SiO_2, which appear in figure 7.18 as a function of frequency. The susceptibility is largest for lowest temperatures, which is in accordance with the Curie law. Regarding the frequency dependence, data at different temperatures show different behavior. Consider first low temperature data at $T = 43\,\mathrm{mK}$, where χ' decreases monotonously with frequency. In order to understand this, imagine a simple model, in which each magnetic moment i with $m_i = |\boldsymbol{m}_i|$ in the sample is a Debye relaxator with a certain relaxation time $\tau_{\mathrm{r},i}$ and an associated characteristic frequency $f_{\mathrm{r},i} = 1/2\pi\tau_{\mathrm{r},i}$. We assign each an effective magnetic moment

$$m_{i,\mathrm{eff}}(f) = \frac{m_i}{1 + \left(\frac{f}{f_{\mathrm{r},i}}\right)^2} \quad , \tag{7.29}$$

which is dependent on the frequency f we probe the system at. This relation expresses that relaxators may only contribute to the susceptibility if $f \lesssim f_{\mathrm{r},i}$, while not contributing at $f \gg f_{\mathrm{r},i}$. Such a frequency dependence is shown in figure 7.19, where the contribution to χ' of an exemplary magnetic moment appears in black. In a system of 50 Debye relaxators (red) with equal magnetic moment m but random characteristic frequencies, we find an overall real part of the susceptibility (gray) that decreases monotonously with increasing frequency. This matches the observed frequency dependence of our low temperature data. Consider now data at a slightly higher temperature of $T = 58\,\mathrm{mK}$. Here, the susceptibility decreases only for $f \gtrsim 100\,\mathrm{Hz}$. In our model of Debye relaxators, this corresponds to a non-uniform distribution of relaxation times $\tau_{\mathrm{r},i}$, specifically to a distribution with a maximum

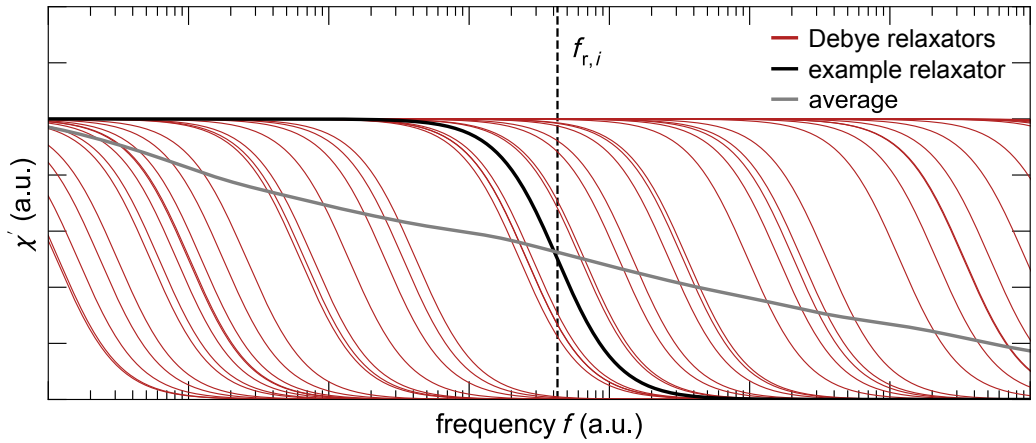

Figure 7.19: Model of 50 Debye relaxators with random relaxation times.

relaxation time $\tau_{\mathrm{r,max}} = (2\pi \cdot 100\,\mathrm{s}^{-1})^{-1} \gtrsim \tau_{\mathrm{r},i}$. For even higher temperatures, the maximum relaxation time is lowered further. In general, our model allows us to deduce a distribution of relaxation times from the frequency dependence of the real part of the susceptibility.

We are now able to interpret our data. At lowest temperatures, we see that χ' halves when going from 1 Hz to 100 kHz. This strong decrease is due to the fact that the relaxation channel is phonon-dominated and hence only few magnetic moments can align with the magnetic field at high frequencies. When increasing the temperature, more phonons are available and the relaxation times decrease, leading to a lower $\tau_{\mathrm{r,max}}$. Together with an overall reduction in contributing moments according to the Curie law, the result is a shoulder in the graph that moves to larger frequency and lower χ' as temperature increases. At highest temperatures, the maximum relaxation time moves outside our measurement range, and χ' appears to become roughly constant. Slight drifts in the data in the order of 2×10^{-4} are most likely due to calibration inaccuracies and show the resolution limit of the noise-o-meter. We believe that a currently planned upgrade of the lock-in amplifier will reduce this effect.

7.4.6 Real Part of the Susceptibility of Au:Er

Data from our measurements on Au:Er appear in figure 7.20. We observe an overall significantly higher susceptibility, due to the large number of erbium ions, which increases as temperature decreases, as the Curie law projects for paramagnetic samples. The frequency dependence is significantly less pronounced, since the magnetic moments in Au:Er exchange energy fast with electrons and can mostly contribute

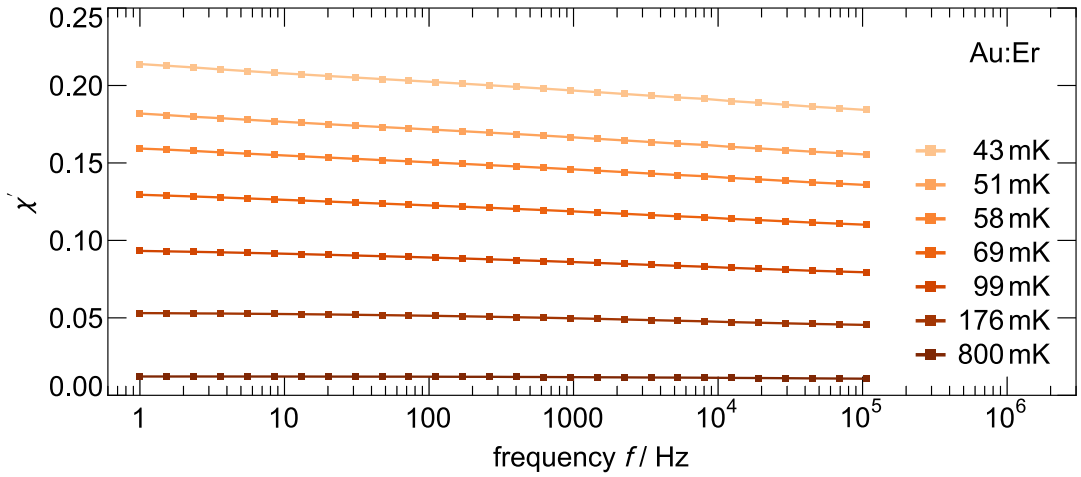

Figure 7.20: Real part of the susceptibility of Au:Er as a function of frequency and temperature.

to χ' even at $f = 100\,\mathrm{kHz}$. In fact, for $T \leq 69\,\mathrm{mK}$, we find to good approximation $\chi' \propto -\log(f)$, with the susceptibility decreasing by around 15 % between 1 Hz and 100 kHz. We conclude that the characteristic frequencies must be distributed logarithmically in Au:Er with less than 15 % lying in our measurement range.

We gain further insight into the magnetic nature of Au:Er by combining the real and imaginary part of the susceptibility. Consider a spin glass, in which magnetic moments are frozen in random orientations, when beneath a certain spin glass freezing temperature T_g. One main feature of this class of material is a broad distribution of relaxation times and a frequency independent χ''. Given these properties, equation

$$\chi'' = \frac{\pi}{2}\frac{\partial\chi'}{\partial \ln f} \quad , \tag{7.30}$$

which we first introduced in section 6.4, relates the real part χ' of the magnetic susceptibility to the imaginary part χ''. Since we have access to both χ' and χ'', we can test if equation (7.30) holds for our data. In figure 7.21, we plot both sides of the equation using Au:Er data. Dots represent the measured imaginary susceptibility, and lines the scaled derivative $\frac{\pi}{2}\frac{\partial\chi'}{\partial \ln f}$ of the measured real part of the susceptibility. The results match closely for all frequencies and temperatures, leading us to the conclusion that the sample acts magnetically similar to a spin glass.

For the Au:Er sample, a complete picture now forms. We measured the $1/f$ noise to have an exponent of $\alpha = -1.00$, which, according to equation (7.21), is the result of a frequency independent χ''. Our analysis of the real part of the susceptibility shows a wide distribution of relaxation times. They are spaced logarithmically,

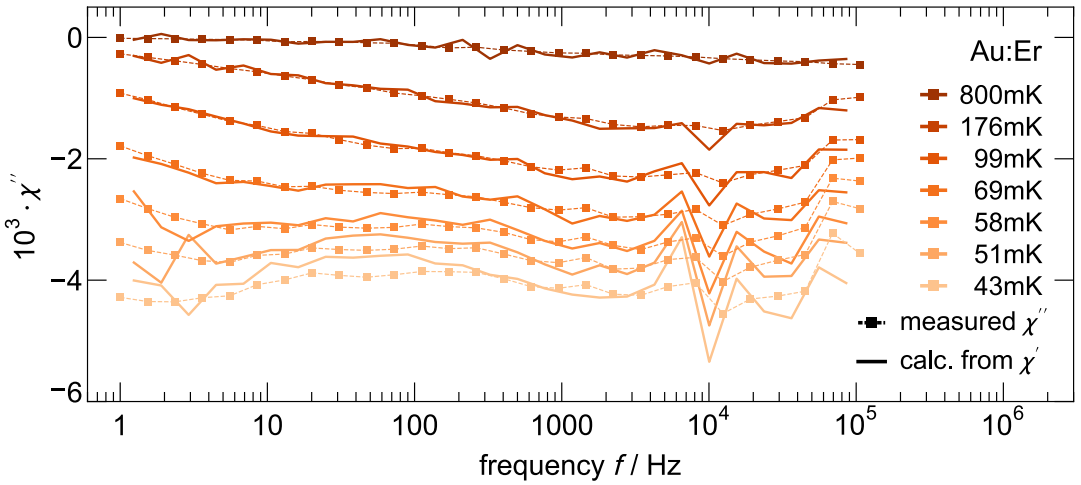

Figure 7.21: Measured imaginary susceptibility (squares) of Au:Er at different frequencies and temperatures. Superimposed in lines are values for χ'' calculated from χ' via equation (7.30).

which, incidentally, is consistent with Néel's superparamagnetic cluster model for spin glasses [Nee49]. The frequency dependencies of χ' and χ'' are consistent with equation (7.30), and indeed the data support this relation. However, our Au:Er sample is not a spin glass at the temperatures we perform our experiments, since T_g lies well below 1 mK [Fle00]. Instead, these properties are a result of the complex magnetic interactions present in the material, which we discuss in section 2.2. They create a wide range of energy levels [Her22], as well as clusters of locked magnetic moments.

7.4.7 Real Part of the Susceptibility of Ag:Er

With a good understanding of our Au:Er sample, we now consider the results of measurements on Ag:Er. The real part of the susceptibility appears in figure 7.22 for different temperatures and frequencies. As for the other samples, χ' decreases with increasing frequency, however less strongly. For $T = 43\,\mathrm{mK}$, the drop is $\sim 7\,\%$ between 1 Hz and 100 kHz, which is half as much as in Au:Er. Also, the decrease of χ' is not logarithmic in f, and instead occurs predominantly at higher frequencies. In fact, there is only a 1.3 % change in susceptibility between 100 mHz and 100 Hz. We must conclude that almost no Debye relaxators have long relaxation times in the range of milliseconds or seconds. Furthermore, the lack of a logarithmic spacing of $f_{r,i}$ indicates that superparamagnetic clustering is not relevant. Overall, the magnetic nature of our Ag:Er differs significantly from that of the Au:Er sample.

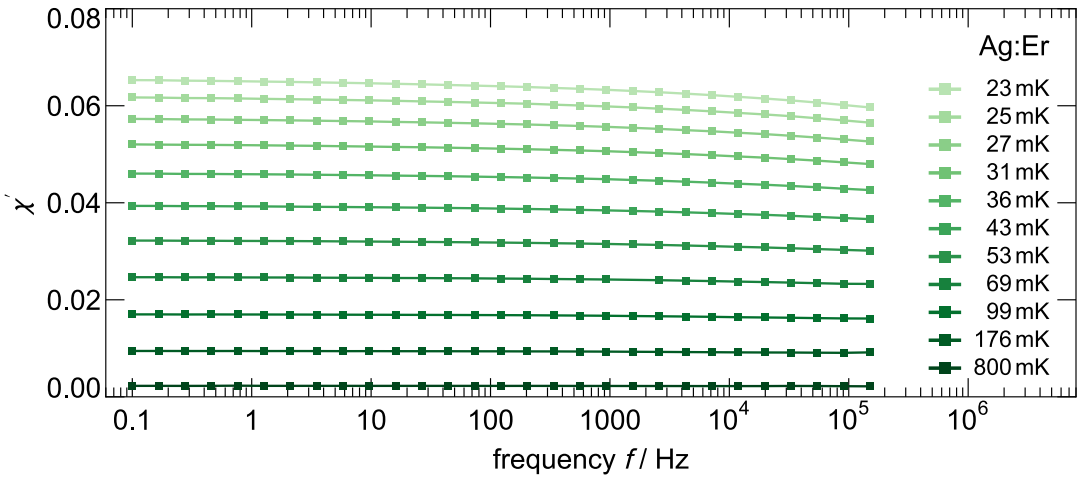

Figure 7.22: Real part of the susceptibility of Au:Er as a function of frequency and temperature.

In order to understand the different behavior of the Au:Er and Ag:Er samples, we consider the two main differences between the materials: the erbium concentration and the noble metal. In our Au:Er, the erbium concentration x_{Er} is around five times higher. As a result, the average distance r between erbium ions is $\sqrt[3]{5} \approx 1.7$ times smaller in the Au:Er sample than in the Ag:Er sample. Since both the dipole-dipole interaction (see equation (2.5)) and the RKKY interaction (see equation (2.7)) contain an r^{-3} component, the concentration difference alone would lead to erbium-erbium interactions being five times stronger in the Au:Er sample. However, this is offset by roughly half, due to the scaling parameter $\Gamma_{\mathrm{RKKY}}/\Gamma_{\mathrm{d\text{-}d}}$ being around $2-3$ times larger for erbium in silver than in gold. We are left with erbium-erbium interactions differing by around a factor of two. This may contribute to the different magnetic behavior of the two samples, especially pertaining to the formation of superparamagnetic clusters [Her22].

An important difference between silver and gold is the presence of nuclear moments. In Au:Er, the 100 % abundant ^{197}Au has a nuclear spin $I = 3/2$ and a strong nuclear electric quadrupole moment of 0.55 b [Pow74]. If the quadrupole experiences a non-cubic electric field gradient, the formerly degenerate energy levels split up. In an fcc lattice, this may arise from erbium ions locally deforming the otherwise symmetric lattice. Experimental evidence for this effect comes from specific heat measurements [Her00] and from MMCs, where an additional rapid decay channel with $\tau_{\mathrm{r}} \approx 100\,\mu\mathrm{s} - 1\,\mathrm{ms}$ exists in systems using Au:Er [Ens00]. Replacing gold with silver, whose two stable isotopes both do not have a nuclear quadrupole moment, removes the additional decay channel [Fle03]. It is possible that the magnetic susceptibility might be similarly affected, if the gold nucleus enables additional decay

channels for the relaxation of 4f electrons of the erbium. We would expect relaxation times to be in a similar order of magnitude to those observed in MMCs, which would mean characteristic frequencies $1/2\pi\tau_\mathrm{r}$ in the order of hundreds of Hz.

Independent of the physical origin of the distribution of relaxation times, the measurement of the distribution goes a long way in explaining the differing magnetic flux noise in our Au:Er and Ag:Er samples. As we discuss in subsection 7.4.6, our Au:Er has a logarithmic distribution of $\tau_{\mathrm{r},i}$, which corresponds to $1/f$ noise with $\alpha = -1$. In comparison, for Ag:Er, the distribution of relaxation times is not logarithmic and the magnetic flux noise has a different frequency dependence. Specifically, we find only a small amount of Debye relaxators with long relaxation times, and a comparatively large amount with short relaxation times (see figure 7.16). Since each relaxator contributes to magnetic flux noise primarily at its inverse relaxation time, this results in comparatively low noise at low frequencies and high noise at high frequencies. The effect is a less extreme slope of $\alpha = -0.86$ (see section 7.4.3).

As a final point, we discuss the impact our results have on the understanding of erbium noise in MMCs. Of interest is in particular the amount of erbium noise per erbium ion, since the number of ions is a rough estimate for the amount of signal we obtain upon temperature change. Ideally, this ratio is as low as possible. At 1 Hz, we observed 6.6 times less noise power per erbium ion in our Ag:Er sample than in the Au:Er sample. Due to the difference in α, this ratio decreases as the frequency increases. In fact, at around 8 kHz, the noise per erbium ion is identical for both samples. For even higher frequencies, noise per ion is larger in the Ag:Er than in the Au:Er.

The question remains, which of the two variants is preferable. Looking at a noise spectrum of an MMC, such as that of Quasy-maXs in figure 4.9, we notice that at low frequencies, erbium noise is the dominant noise component. On the other hand, readout noise dominates at $f \gtrsim 3\,\mathrm{kHz}$. A reduction of erbium noise at low frequencies would thus lower the overall noise there, while the accompanying increase of erbium noise at high frequencies would barely influence the noise spectrum. In general, it is thus preferable to use an erbium alloy with low magnetic flux noise at 1 Hz and a comparatively flat slope, which, in our case, is the Ag:Er alloy. Unfortunately, its erbium concentration is too low for our applications. It is thus intriguing to learn more about the microscopic mechanism, which defines the slope of the erbium noise, since a high concentration, low $|\alpha|$ sensor would greatly benefit magnetic microcalorimeters with reduced cooling requirements.

7.5 Improvements and Future Experiments

In this thesis we have developed the noise-o-meter to be a functioning experiment and have demonstrated its capabilities on measurements of first samples. For the next phase, we suggest implementing a number of improvements:

- The biggest open question is the topic of **cross-talk** in cross-correlation mode. We have observed different apparent amounts of cross-talk in the copper set-up and the silver set-up, with cross-talk in the latter exceeding the expected maximum value that may occur via the front-end SQUID input coils. This suggests other cross-talk channels, which requires us to rethink the mathematical cross-talk correction, in particular equation (7.13). A first step is a sample-free measurement with the silver set-up, where the lack of Johnson noise from the sensor should give us a precise measure for the amount of cross-talk at high frequencies. Further experiments could probe for individual cross-talk channels. One example would be repeating the measurement we explain in subsection 7.3.2, where we apply a signal to the feedback coil of one SQUID and measure the signal in the other SQUID, but remove the washer of the former SQUID. This would check for direct coupling between feedback coil and input coil. If we instead remove the noise-o-meter chip, we measure cross-talk between the read-out channels, which is not transmitted via the input coils.

- Replacement of the **lock-in amplifier** may remove the poorly understood time delay and small, but relevant, complex frequency dependence we observe when measuring phase shifts (see figure 7.12). This should improve resolution in susceptibility mode, and make inaccuracies in calibration measurements less impactful.

- An improvement when measuring the real part of the susceptibility would be to replace the aluminum bonding wires with **niobium bonding wires**. Their significantly higher critical temperature of 9.2 K would allow for accurate measurements up to much higher temperatures.

- In order to expand the possible temperature range downward, we must improve the **thermalization** of the noise-o-meter chip. Thinkable are additional thermal links, such as gold bonds from the top of the noise-o-meter chip to a heat bath, or a clamp pressing down the chip from the top.

Looking further, a wide variety of future experiments present themselves, a selection of which we introduce here:

- An immediate follow-up experiment is further investigation of **erbium noise**. Our experiments so far have shown significant differences between low concentration Ag:Er and high concentration Au:Er. Currently, it is not obvious whether the concentration or the different noble metal causes a larger effect, with possible explanations existing for either. While older measurements with significantly lower erbium concentrations also suggest $\alpha = -1$, these experiments did not disentangle magnetic flux noise from read-out noise and a repeat measurement would be helpful. Thus, measurements of either high-concentration Ag:Er or low-concentration Au:Er would likely illuminate the situation. Thinkable is also measuring a Ag:Er alloy containing ^{167}Er, since the isotopic composition of our two samples is a further difference between them. Overall, a detailed understanding of erbium noise could lead to an immediate improvement of all future MMCs.

- The noise-o-meter allows for efficient **process development**. One example is the minimization of noise from insulating SiO_2 layers by modifying manufacturing parameters. Such an experiment requires only two micro-fabricated layers, niobium and the SiO_2, and results can be available within one week.

- Instead of applying sample materials, we can also **modify the superconductor** of two opposite meander coils and check for variations in the noise. Thinkable, for instance, is selectively loading the niobium with hydrogen, as previous experiments indicate that hydrogen could be a source of magnetic flux noise in SQUIDs [Kaa20].

- Currently under development is a noise-o-meter chip designed for **macroscopic samples**. The wiring is modified, so that the meander coils to which we apply the sample, are located next to each other on the chip instead of diagonally. As a result, we can clamp a single chunk of a macroscopic sample across two meander coils. This opens the possibility for us to measure samples, which cannot be deposited in a sputtering process. An example are complex heavy fermion systems, which must be grown by molecular beam epitaxy [Bak22].

- The Wheatstone bridge does not necessarily have to consist of meander coils. Instead, the coils may be replaced by **entire devices**, such as qubits or SQUIDs. Then, by modifying two opposite devices, we can determine if the modification may improve the performance of the device. The only restriction is that the modification must impact the device's inductance in some way. Note that for a set-up using a device with a small base inductance L_0 such as a

SQUID, it follows from equation (7.12) that cross-talk may become significant. In that case, it may be better to connect the two front-end SQUIDs in parallel, which modifies equations (7.10) and (7.11) to be

$$\begin{aligned} \delta\Phi_{\mathrm{s,m,par}} &= M_{\mathrm{in}} \frac{\delta\Phi_{\mathrm{m}}}{4L_0 + 2(L_{\mathrm{i}} + L_{\mathrm{w}})} && \gg \delta\Phi_{\mathrm{s,m}} \quad \text{and} \\ \delta\Phi_{\mathrm{s,x,par}} &= M_{\mathrm{in}} \frac{\delta\Phi_{\mathrm{i,X}}}{\frac{(L_{\mathrm{i}}+L_{\mathrm{w}})^2}{L_0} + 2(L_{\mathrm{i}} + L_{\mathrm{w}})} && \ll \delta\Phi_{\mathrm{s,X}} \quad . \end{aligned} \tag{7.31}$$

Overall, we believe that experiments with the noise-o-meter have only just begun. With capabilities ranging from noise analysis in a specific experimental set-up, to measuring the complex susceptibility and magnetic flux noise of samples, and finally to unveiling the microscopic magnetic nature of materials, our list of experiments above is likely only a small part of possible future applications.

8. Conclusion

Magnetic micro-calorimeters (MMC) are cryogenic particle detectors typically operated at around 20 mK. When a particle, often an X-ray, impacts the device, the temperature increase leads to a change in magnetization of a paramagnetic sensor material, which sits in a weak magnetic field. Using superconducting structures, we read out this magnetization change and thus have a sensitive measure for the energy of the original particle. In this thesis, we have discussed the topic of magnetic micro-calorimeters, and in particular the simulation of their thermodynamics, the limits of their cooling requirements, and the disentangling of their noise.

Regarding the first of these points, we have developed a new software package for simulating MMCs, consisting of two major new scripts. The first allows for the numerical calculation of the thermodynamic properties of the paramagnetic sensor material [Her22]. Using this code, we have built a repository of the specific heat, magnetization, and slope $\partial M/\partial T$ of the magnetization of Au:Er and Ag:Er at magnetic fields of up to 60 mT, erbium concentrations of up to 3200 ppm, and temperatures between 10 mK and 400 mK. This parameter range covers all current applications of MMCs. The second script simulates an MMC with given parameters and returns the projected energy resolution ΔE_{FHWM}, pulse height $\delta\Phi$ upon energy deposition, noise spectrum, and magnetization $M(T)$. The script is able to iterate through arrays of initial parameters and automatically interpolate optimal values. Furthermore, it supports specialized MMC designs with integrated SQUID read-out [Zak03], double transformer coupling [Muh83], hydra designs [Por11], and multiple pixels per channel [Gam19], which has already enabled its application in other projects [Sch21, Man21, Bau22].

As a result of our simulations, we found that in order to construct competitive MMCs with reduced cooling requirements, we had to use sensor material with a high erbium concentration x_{Er}. To this end, we manufactured a Au:Er sputtering target with $x_{\mathrm{Er}} \approx 2500$ ppm by combining small amounts of gold and erbium in an arc-melting furnace, which we then added to a pre-existing low-concentration target in a graphite crucible. Using this target, we were able to deposit thin films of Au:Er with consistent, high concentration and negligible impurities.

We first employed our new sensor material in a novel MMC called Quasy-maXs. This detector is optimized for operation at uncommonly high temperatures of 85 mK. Besides the high concentration of erbium in the Au:Er temperature sensor, Quasy-maXs features two gradiometric and two asymmetric channels, where for the latter, one pick-up coil with inductance L_{m} is replaced with a load inductor with an inductance

of $L_{\mathrm{load}} = 6.4\,L_{\mathrm{m}}$. Furthermore, Quasy-maXs comes in four variants with differing thermal links between absorber and sensor, and between sensor and thermal bath. This makes the detector versatile, enabling usage at different temperatures and for different experimental requirements.

In our characterization of Quasy-maXs, we found that two variants with different thermal links between absorber and sensor had consistent, temperature-independent rise times of $\sim 480\,\mathrm{ns}$ and $\sim 24\,\mu\mathrm{s}$, respectively, which matched appropriate thermal links in the sensor material. An analysis of the decay times showed faster than expected values, due to absorbers not being free-standing. Measurements of the energy resolution showed a best value of $(5.2 \pm 0.2)\,\mathrm{eV}$ for baselines at 41 mK and 19.0 eV for 6 keV photons at 85 mK. We found that the asymmetric design improved the energy resolution by $\sim 50\,\%$, and that chips with short characteristic time constants were slightly favorable.

Our characterization showed that Quasy-maXs had immediate applicability. In collaboration with a team in Lisbon, we have introduced our detector into a new set-up for particle induced X-ray emission (PIXE) spectroscopy [Joh70, Joh76, Rei23], a first for MMCs. For this, we have developed a dedicated, custom-built set-up, which allows for operation of an MMC within the small volume available in such an experiment. First measurements of PIXE X-rays are expected in mid-2023. We believe that Quasy-maXs will outperform the previously installed transition edge sensor [Cha14], and that a number of small improvements can further improve the energy resolution to below 10 eV for 6 keV photons at 85 mK.

Further exploring the temperature range in which magnetic micro-calorimetry is possible, we constructed a second new MMC, called Hot-maXs. This proof-of-principle detector features high concentration Au:Er, a substrate made of fused silica, and absorbers made of superconducting lead. In order to attach the latter, we have developed a procedure involving a custom-made mold, which aligns the absorbers before diffusion welding raised absorber sections directly to the sensor material. Using this tool, we were able to produce stable, free-standing absorbers. For measurements at high-temperatures, we updated a pre-existing detector arm [Sch12] with new components to allow for quick and simple exchange of experiments.

In a first test of Hot-maXs, we were able to detect signals from 60 keV photons at temperatures of up to 300 mK, the highest ever temperature an MMC has been successfully operated at. Rise times at 41 mK were limited to 95 µs, likely caused by quasiparticle recombination, while the signal decay showed a long tail. Above 125 mK, the signal decay was temperature independent at $\sim 400\,\mu\mathrm{s}$ and dominated by phononic thermalization with the substrate. At temperatures below 125 mK, the energy resolution at 60 keV was limited by variations of the pulse shape, and above 125 mK by the baseline resolution. Overall, we found a best energy resolution of

22.6 eV for baselines at 41 mK, and a phenomenological upper limit for the resolving power $E/\Delta E_{\mathrm{FWHM}}$ of ~ 300.

For an analysis of noise in superconducting microstructures, we have developed the noise-o-meter, a new type of chip and experiment designed to disentangle and quantify noise. By comparing the noise measured in three different measurement modes, we are able to deduce the contribution of different noise components. Experimentally, the central component is a silicon chip containing a Wheatstone-like bridge consisting of four identical superconducting inductors. A sample material may be placed on two opposite inductors. Noise read-out occurs via a pair of cross-correlated SQUID-based read-out chains, or by probing the bridge with an AC signal. First measurements showed that we were able to read out cross-correlated noise at the quantum limit, and magnetic flux noise significantly beneath.

When placing the noise-o-meter on the experimental platform designed for HotmaXs, we observed a low frequency noise plateau with an amplitude of $2.9\,\mu\Phi_0/\sqrt{\mathrm{Hz}}$ and a cut-off at 143 Hz. We traced this to magnetic Johnson noise from the copper holder coupling magnetically into the loop spanned by the bonding wires between noise-o-meter chip and front-end SQUID chip, but mitigated by the skin effect at high frequencies. In order to avoid this noise component in future measurements, we developed a new silver platform based on the body of a noise thermometer [Stä20, Fle20]. By coating the silver with superconducting niobium, the magnetic Johnson noise was sufficiently suppressed. In a measurement of a silver erbium alloy, we instead found previously undetectable magnetic Johnson noise from the sample with an amplitude of under $0.04\,\mu\Phi_0/\sqrt{\mathrm{Hz}}$ at 23 mK.

In further experiments, we were, for the first time, able to perform a high-precision measurement of a magnetic flux noise component affecting MMCs, which originates from the magnetic moments in the sensor material [Fle03, Dan05]. When investigating the Au:Er alloy as a sample, we found a $1/f$ magnetic flux noise component with an amplitude of $(0.115 \pm 0.006)\,\mu_{\mathrm{B}}^2/\mathrm{Hz}$ per erbium ion at 1 Hz and an exponent of $\alpha = -1.00 \pm 0.03$. Measuring an alloy of silver and erbium with $x_{\mathrm{Er}} = 480$ ppm revealed significantly less magnetic flux noise at 1 Hz with $(0.0175 \pm 0.0009)\,\mu_{\mathrm{B}}^2/\mathrm{Hz}$ per erbium ion and an exponent of $\alpha = -0.856 \pm 0.014$.

By comparing these results to the real part of the samples' complex AC susceptibility, we were able to explain the difference in these values in the framework of a model based on Debye relaxators. Specifically, we found that in the Ag:Er sample, relaxation times were shorter, leading to magnetic flux noise at higher frequencies. In Au:Er, a flat logarithmic distribution of relaxation times caused noise at low frequencies. A better understanding of the dynamics of the erbium ions could improve the performance of MMCs in general, since designing sensor material with magnetic flux noise shifted to high frequencies would reduce the overall noise in the MMC.

Our analysis of the erbium noise showed that the noise-o-meter is more than a noise disentangling device, since it also offers insight into the microscopic magnetic nature of materials. This suggests a wide variety of future experiments in the much broader field of condensed matter physics. Besides potential follow-up investigations on the magnetic nature of erbium, we are also part of a currently ongoing collaboration with groups in Vienna and Zaragoza, in which we attempt to gain insight into the spin dynamics of the heavy fermion compound $YbRh_2Si_2$ by analyzing it with the noise-o-meter.

In a final remark, we return to the title of this thesis. By combining all three aspects, thermodynamics, cooling requirements, and noise, we were able to significantly advance the field magnetic micro-calorimetry. Specifically, incorporating our findings on noise into our new simulations of the thermodynamics of MMCs, gave us a powerful tool to precisely predict measurements. Our experiments with MMCs at high temperatures show examples: The simulated noise spectrum and magnetization curve of Quasy-maXs match our measurements without fit parameters. Going one step further, our improved models have facilitated the development of two new detectors with reduced cooling requirements, and have already expanded the application range of MMCs to temperatures of 85 mK and to the field of particle induced X-ray emission spectroscopy. With Hot-maXs showing a much wider potential horizon, we hope that further research in this direction will follow.

List of Publications

The following is a list of first-author publications during the course of this thesis. Of these, the latter two share considerable thematic overlap with topics discussed here.

1. M. Herbst, A. Reifenberger, C. Velte, H. Dorrer, C. E. Düllmann, C. Enss, A. Fleischmann, L. Gastaldo, S. Kempf, T. Kieck, U. Köster, F. Mantegazzini, and K. Wendt, Specific heat of holmium in gold and silver at low temperatures, *J. Low Temp. Phys.*, **202**(1), 106–120, 2021.

2. M. Herbst, A. Barth, A. Fleischmann, L. Gastaldo, D. Hengstler, N. Kovac, F. Mantegazzini, A. Reifenberger, and C. Enss, Numerical calculation of the thermodynamic properties of silver erbium alloys for use in metallic magnetic calorimeters, *J. Low Temp. Phys.*, **209**(5), 1119–1127, 2022.

3. M. Herbst, A. Fleischmann, D. Hengstler, D. Mazibrada, L. Münch, A. Reifenberger, C. Ständer, and C. Enss, Measuring magnetic 1/f noise in superconducting microstructures and the fluctuation-dissipation theorem, *under review.* arXiv:2303.15257v2, 2023.

Bibliography

[Abr70] A. Abragam and B. Bleaney, Electron Paramagnetic Resonance of Transition Ions, Clarendon Press, Oxford, 1970.

[Aki07] Y. K. Akimov, Silicon radiation detectors (Review), *Instrum. Exp. Tech*, **50**(1), 1–28, 2007.

[Bak22] E. Bakali, W. Artner, M. Beiser, J. Bernardi, H. Detz, G. Eguchi, A. Foelske, M. Giparakis, C. Herzig, A. Limbeck, H. Nguyen, L. Prochaska, A. Prokofiev, M. Sauer, S. Schwarz, W. Schrenk, G. Strasser, R. Svagera, M. Taupin, A. S. Thirsfeld, et al., A Knudsen cell approach for the molecular beam epitaxy of the heavy fermion compound $YbRh_2Si_2$, *J. Cryst. Growth*, **595**, 126804, 2022.

[Ban93] S. R. Bandler, C. Enss, R. E. Lanou, H. J. Maris, T. More, F. S. Porter, and G. M. Seidel, Metallic magnetic bolometers for particle detection, *J. Low Temp. Phys.*, **93**(3), 709–714, 1993.

[Ban19] S. R. Bandler, J. A. Chervenak, A. M. Datesman, A. M. Devasia, M. DiPirro, K. Sakai, S. J. Smith, T. R. Stevenson, W. Yoon, D. Bennett, B. Mates, D. Swetz, J. N. Ullom, K. D. Irwin, M. E. Eckart, E. Figueroa-Feliciano, D. McCammon, K. Ryu, J. Olson, and B. Zeiger, Lynx x-ray microcalorimeter, *Journal of astronomical telescopes, instruments, and systems*, **5**(2), 2019.

[Bar09] R. Barends, S. van Vliet, J. J. A. Baselmans, S. J. C. Yates, J. R. Gao, and T. M. Klapwijk, Enhancement of quasiparticle recombination in Ta and Al superconductors by implantation of magnetic and nonmagnetic atoms, *Phys. Rev. B*, **79**(2), 020509, 2009.

[Bar23] A. Barth, *to be published*, PhD Thesis, Heidelberg University, 2023.

[Bau22] F. Bauer, Rauscharme Stromsensor-dc-SQUIDs mit Impedanzanpassung für metallische magnetische Kalorimeter, PhD Thesis, Heidelberg University, 2022.

[Bec96] H. Becquerel, Sur les radiations émises par phosphorescence, *Compt. Rend. Acad. Sc. Paris*, **122**, 420, 1896.

[Bey07] J. Beyer, D. Drung, A. Kirste, J. Engert, A. Netsch, A. Fleischmann, and C. Enss, A magnetic-field-fluctuation thermometer for the mK range based on SQUID-magnetometry, *IEEE T. Appl. Supercon.*, **17**(2), 760–763, 2007.

[Bia07] R. C. Bialczak, R. McDermott, M. Ansmann, M. Hofheinz, N. Katz, E. Lucero, M. Neeley, A. D. O'Connell, H. Wang, A. N. Cleland, and J. M. Martinis, $1/f$ flux noise in Josephson phase qubits, *Phys. Rev. Lett.*, **99**(18), 187006, 2007.

[Blu22] Bluefors, User manual LD system version 2.0, 2022.

[Boy18] S. T. P. Boyd, R. Hummatov, G. B. Kim, L. N. Le, J. A. Hall, R. Cantor, and S. Friedrich, Integrated SQUID/sensor metallic magnetic microcalorimeter for gamma-ray spectroscopy, *J. Low Temp. Phys.*, **193**(3), 435–440, 2018.

[Bra13] W. H. Bragg and W. L. Bragg, The reflection of X-rays by crystals, **88**, 428–438, 1913.

[Bru82] J. J. P. Bruines, V. J. de Waal, and J. E. Mooij, Comment on: "Dc SQUID: Noise and optimization" by Tesche and Clarke, *J. Low Temp. Phys.*, **46**(3), 383–386, 1982.

[Bur08] A. Burck, S. Kempf, S. Schäfer, H. Rotzinger, M. Rodrigues, T. Wolf, L. Gastaldo, A. Fleischmann, and C. Enss, Microstructured magnetic calorimeter with meander-shaped pickup coil, *J. Low Temp. Phys.*, **151**(1), 337–344, 2008.

[Cal51] H. B. Callen and T. A. Welton, Irreversibility and generalized noise, *Phys. Rev.*, **83**(1), 34–40, 1951.

[Cha14] P. C. Chaves, A. Taborda, J. P. Marques, and M. A. Reis, N to K Uranium PIXE spectra obtained at the high resolution high energy PIXE setup, *Nucl. Instrum. Meth. B*, **318**, 60–64, 2014.

[Cla04] J. Clarke and A. I. Braginski (Ed.), The SQUID Handbook: Fundamentals and Technology of SQUIDs and SQUID Systems, WILEY-VCH, Weinheim, 2004.

[Cla06] J. Clarke and A. I. Braginski (Ed.), The SQUID Handbook: Applications of SQUIDs and SQUID Systems, Volume II | Wiley, WILEY-VCH, Weinheim, 2006.

[Com18] B. O. Community, Blender - a 3D modelling and rendering package, 2018.

[Cos34] C. R. Cosens, A balance-detector for alternating-current bridges, *P. Phys. Soc.*, **46**(6), 818, 1934.

[Cos93] E. Cosulich, F. Gatti, and S. Vitale, Further results on μ-calorimeters with superconducting absorber, *J. Low Temp. Phys.*, **93**(3-4), 263–268, 1993.

[Dan05] T. Daniyarov, Metallische magnetische Kalorimeter zum hochauflösenden Nachweis von Röntgenquanten und hochenergetischen Molekülen, PhD Thesis, Heidelberg University, 2005.

[Dav25] W. P. Davey, Precision measurements of the lattice constants of twelve common metals, *Phys. Rev.*, **25**(6), 753–761, 1925.

[Dev22] A. M. Devasia, S. R. Bandler, K. Ryu, T. R. Stevenson, and W. Yoon, Large-scale magnetic microcalorimeter arrays for the Lynx X-ray microcalorimeter, *J. Low Temp. Phys.*, **209**(3), 337–345, 2022.

[DG58] P.-G. De Gennes, Sur le magnetisme des metaux de terres rares, *Comp. Rend. Acad. Sci.*, **247**, 1836, 1958.

[Dru06] D. Drung, C. Hinnrichs, and H.-J. Barthelmess, Low-noise ultra-high-speed dc SQUID readout electronics, *Supercond. Sci. Tech.*, **19**(5), S235, 2006.

[Dru11] D. Drung, J. Beyer, J.-H. Storm, M. Peters, and T. Schurig, Investigation of low-frequency excess flux noise in DC SQUIDs at mk temperatures, *IEEE T. Appl. Supercon.*, **21**(3), 340–344, 2011.

[Duv20] J.-M. Duval, T. Prouvé, P. Shirron, K. Shinozaki, Y. Sekimoto, T. Hasebe, G. Vermeulen, J. André, M. Hasumi, L. Montier, and B. Mot, LiteBIRD cryogenic chain: 100 mk cooling with mechanical coolers and ADRs, *J. Low Temp. Phys.*, **199**(3), 730–736, 2020.

[Ein05] A. Einstein, Ist die Trägheit eines Körpers von seinem Energieinhalt abhängig?, *Ann. Phys.*, **323**(13), 639–641, 1905.

[Ens00] C. Enss, A. Fleischmann, K. Horst, J. Schönefeld, J. Sollner, J. S. Adams, Y. H. Huang, Y. H. Kim, and G. M. Seidel, Metallic magnetic calorimeters for particle detection, *J. Low Temp. Phys.*, **121**(3), 137–176, 2000.

[Ens05a] C. Enss and S. Hunklinger, Low-Temperature Physics, Springer, Berlin Heidelberg, 2005.

[Ens05b] C. Enss (Ed.), Cryogenic Particle Detection, Springer, Berlin, Heidelberg, 2005.

[Fer15] A. Ferring, Entwicklung von dc-SQUIDs zur Auslesung von metallischen magnetischen Kalorimetern, Master's Thesis, Heidelberg University, 2015.

[Fle00] A. Fleischmann, J. Schönefeld, J. Sollner, C. Enss, J. S. Adams, S. R. Bandler, Y. H. Kim, and G. M. Seidel, Low temperature properties of erbium in gold, *J. Low Temp. Phys.*, **118**, 7–21, 2000.

[Fle01] A. Fleischmann, High resolution X-ray detection using metallic magnetic calorimeters, in B. Kramer (Ed.), *Advances in Solid State Physics*, 577–588, Springer, Berlin, Heidelberg, 2001.

[Fle03] A. Fleischmann, Magnetische Mikrokalorimeter: Hochaufloesende Roentgenspektroskopie mit energiedispersiven Detektoren, PhD Thesis, Heidelberg University, 2003.

[Fle04] A. Fleischmann, M. Link, T. Daniyarov, H. Rotzinger, C. Enss, and G. M. Seidel, Metallic magnetic calorimeters (MMC): Detectors for high-resolution X-ray spectroscopy, *Nucl. Instrum. Meth. A*, **520**(1), 27–31, 2004.

[Fle05] A. Fleischmann, C. Enss, and G. M. Seidel, Metallic magnetic calorimeters, in *Cryogenic Particle Detection*, 151–216, Springer, Berlin/Heidelberg, 2005.

[Fle09a] A. Fleischmann, L. Gastaldo, S. Kempf, A. Kirsch, A. Pabinger, C. , J. P. Porst, P. Ranitzsch, S. Schäfer, F. v. Seggern, T. Wolf, C. Enss, and G. M. Seidel, Metallic magnetic calorimeters, *AIP Con. Proc.*, **1185**, 571–578, 2009.

[Fle09b] L. Fleischmann, M. Linck, A. Burck, C. Domesle, S. Kempf, A. Pabinger, C. Pies, J. P. Porst, H. Rotzinger, S. Schafer, R. Weldle, A. Fleischmann, C. Enss, and G. Seidel, Metallic magnetic calorimeters for X-ray spectroscopy, *Appl. Supercond. IEEE Transactions*, **19**, 63–68, 2009.

[Fle20] A. Fleischmann, A. Reiser, and C. Enss, Noise thermometry for ultralow temperatures, *J. Low Temp. Phys.*, **201**(5), 803–824, 2020.

[For23] FormFactor, HPD Model 106 mid-sized, cryogen-free ADR cryostat, 2023.

[Fra76] S. Fraga, J. Karwowski, and K. M. S. Saxena, Handbook of Atomic Data, Elsevier Scientific Publishing Company, Amsterdam, 1976.

[Gal91] G. Gallinaro, F. Gatti, and S. Vitale, Single-particle thermal detection in superconducting rhenium, *Europhys. Lett.*, **14**(3), 225, 1991.

[Gam19] L. E. Gamer, Entwicklung und Charakterisierung des 4k-Pixel Detektorarrays MOCCA für die energie- und ortsaufgelöste Detektion neutraler Molekülfragmente, PhD Thesis, Heidelberg University, 2019.

[Gas17] L. Gastaldo, K. Blaum, K. Chrysalidis, T. Day Goodacre, A. Domula, M. Door, H. Dorrer, C. E. Düllmann, K. Eberhardt, S. Eliseev, C. Enss, A. Faessler, P. Filianin, A. Fleischmann, D. Fonnesu, L. Gamer, R. Haas, C. Hassel, D. Hengstler, J. Jochum, et al., The electron capture in ^{163}Ho experiment – ECHo, *Eur. Phys. J. Spec. Top.*, **226**(8), 1623–1694, 2017.

[Gei20] J. Geist, Bestimmung der Isomerenergie von ^{229}Th mit dem hochauflösenden Mikrokalorimeter-Array maXs30, PhD Thesis, Heidelberg University, 2020.

[Ger23] J. M. Geria, M. R. Hampel, S. Kempf, J. J. Bonaparte, L. P. Ferreyro, M. E. G. Redondo, D. A. Almela, J. M. Salum, N. Müller, J. D. Bonilla-Neira, A. E. Fuster, M. Platino, and A. Etchegoyen, Suitability of magnetic microbolometers based on paramagnetic temperature sensors for CMB polarization measurements, *Journal of Astronomical Telescopes, Instruments, and Systems*, **9**(01), 2023.

[Gol93] A. A. Golubov and E. P. Houwman, Quasiparticle relaxation rates in a spatially inhomogeneous superconductor, *Physica C*, **205**(1), 147–153, 1993.

[Gup78] M. S. Gupta, Thermal fluctuations in driven nonlinear resistive systems, *Phys. Rev. A*, **18**(6), 2725–2731, 1978.

[Gup82] M. S. Gupta, Thermal noise in nonlinear resistive devices and its circuit representation, *IEEE Proc.*, **70**, 788–804, 1982.

[Hah92] W. Hahn, M. Loewenhaupt, and B. Frick, Crystal field excitations in dilute rare earth noble metal alloys, *Phys. B Condens. Matter*, **180-181**, 176–178, 1992.

[Ham21] R. Hammann, A. Barth, A. Fleischmann, D. Schulz, and L. Gastaldo, Data reduction for a calorimetrically measured ^{163}Ho spectrum of the ECHo-1k experiment, *The Eur. Phys. J. C*, **81**(11), 963, 2021.

[Har20] C. R. Harris, K. J. Millman, S. J. van der Walt, R. Gommers, P. Virtanen, D. Cournapeau, E. Wieser, J. Taylor, S. Berg, N. J. Smith, R. Kern, M. Picus, S. Hoyer, M. H. van Kerkwijk, M. Brett, A. Haldane, J. F. del Río, M. Wiebe, P. Peterson, P. Gérard-Marchant, et al., Array programming with NumPy, *Nature*, **585**(7825), 357–362, 2020.

[Hen17] D. Hengstler, Development and Characterization of Two-Dimensional Metallic Magnetic Calorimeter Arrays for the High-Resolution X-Ray Spectroscopy, PhD Thesis, Heidelberg University, 2017.

[Hen23] D. Hengstler, Unpuplished Data, 2023.

[Her00] T. Herrmannsdörfer, R. König, and C. Enss, Properties of Er-doped Au at ultralow temperatures, *Physica B*, **284-288**, 1698–1699, 2000.

[Her18] M. Herbst, Specific Heat of Dilute Alloys of Holmium and Noble Metals at Low Temperatures, Master's Thesis, Heidelberg University, 2018.

[Her21] M. Herbst, A. Reifenberger, C. Velte, H. Dorrer, C. E. Düllmann, C. Enss, A. Fleischmann, L. Gastaldo, S. Kempf, T. Kieck, U. Köster, F. Mantegazzini, and K. Wendt, Specific heat of holmium in gold and silver at low temperatures, *J. Low Temp. Phys.*, **202**(1), 106–120, 2021.

[Her22] M. Herbst, A. Barth, A. Fleischmann, L. Gastaldo, D. Hengstler, N. Kovac, F. Mantegazzini, A. Reifenberger, and C. Enss, Numerical calculation of the thermodynamic properties of silver erbium alloys for use in metallic magnetic calorimeters, *J. Low Temp. Phys.*, **209**(5), 1119–1127, 2022.

[Her23] M. Herbst, A. Fleischmann, D. Hengstler, D. Mazibrada, L. Münch, A. Reifenberger, C. Ständer, and C. Enss, Measuring magnetic 1/f noise in superconducting microstructures and the fluctuation-dissipation theorem, *arXiv:2303.15257*, 2023.

[Hof12] V. Hoffmann, Messung Der AC-Suszeptibilität von paramagnetischem AuEr bei Temperaturen oberhalb des Spinglas-Übergangs, Bachelor's Thesis, Heidelberg University, 2012.

[Höl97] G. Hölzer, M. Fritsch, M. Deutsch, J. Härtwig, and E. Förster, $K\alpha_{1,2}$ and $K\beta_{1,3}$ X-ray emission lines of the 3*d* transition metals, *Phys. Rev. A*, **56**(6), 4554–4568, 1997.

[Hub09] J. H. Hubbell and S. M. Seltzer, X-ray mass attenuation coefficients, *NIST*, 2009.

[IAE00] IAEA, Instrumentation for PIXE and RBS, Text, International Atomic Energy Agency, 2000.

[Ish19] K. Ishii, PIXE and its applications to elemental analysis, *Quantum Beam Sci.*, **3**(2), 12, 2019.

[Joh28] J. B. Johnson, Thermal agitation of electricity in conductors, *Phys. Rev.*, **32**(1), 97–109, 1928.

[Joh70] T. B. Johansson, R. Akselsson, and S. A. E. Johansson, X-ray analysis: Elemental trace analysis at the 10-12 g level, *Nucl. Instrum. Methods*, **84**(1), 141–143, 1970.

[Joh76] S. A. E. Johansson and T. B. Johansson, Analytical application of particle induced X-ray emission, *Nucl. Instrum. Methods*, **137**(3), 473–516, 1976.

[Joh88] S. A. E. Johansson and J. L. Campbell, PIXE: A Novel Technique for Elemental Analysis, John Wiley & Sons, New York, 1988.

[Kaa20] F. Kaap, Untersuchung des Einflusses von Kernspins und in Niob gespeichertem Wasserstoff auf das niederfrequente magnetische Flussrauschen in supraleitenden Quanteninterferenzdetektoren, Master's Thesis, Heidelberg University, 2020.

[Kah65] W. Kahan, Further remarks on reducing truncation errors, *Comm. of the ACM*, **8**(1), 40, 1965.

[Kah23] N. Kahne, *bo be published*, Master's Thesis, Heidelberg University, 2023.

[Kap76] S. B. Kaplan, C. C. Chi, D. N. Langenberg, J. J. Chang, S. Jafarey, and D. J. Scalapino, Quasiparticle and phonon lifetimes in superconductors, *Phys. Rev. B*, **14**(11), 4854–4873, 1976.

[Kas56] T. Kasuya, A theory of metallic ferro- and antiferromagnetism on Zener's model, *Prog. Theor. Phys.*, **16**(1), 45–57, 1956.

[Kem16] S. Kempf, A. Ferring, and C. Enss, Towards noise engineering: Recent insights in low-frequency excess flux noise of superconducting quantum devices, *Appl. Phys. Lett.*, **109**(16), 162601, 2016.

[Kem18] S. Kempf, A. Fleischmann, L. Gastaldo, and C. Enss, Physics and applications of metallic magnetic calorimeters, *J. Low Temp. Phys.*, **193**(3), 365–379, 2018.

[Khi34] A. Khintchine, Korrelationstheorie der stationären stochastischen Prozesse, *Math. Ann.*, **109**(1), 604–615, 1934.

[Kim21] S. G. Kim, J.-A. Jeon, H. B. Kim, H. L. Kim, S. R. Kim, Y.-H. Kim, D. H. Kwon, M. K. Lee, Y. C. Lee, and K. R. Woo, Low temperature property study of MMCs used for neutrinoless double beta decay, *IEEE T. Appl. Supercon.*, **31**(5), 1–5, 2021.

[Kit05] C. Kittel, Introduction to Solid State Physics, Wiley, 8th. edition edition, 2005.

[Koc83] R. H. Koch, J. Clarke, W. M. Goubau, J. M. Martinis, C. M. Pegrum, and D. J. van Harlingen, Flicker $(1/f)$ noise in tunnel junction dc SQUIDS, *J. Low Temp. Phys.*, **51**(1), 207–224, 1983.

[Koc20] C. Koch and T. J. Rinke, Photolithography Basics of Microstructuring, Siegl Druck & Medium GmbH & Co. KG, Friedrichshafen, Germany, 2020.

[Kog81] S. M. Kogan, $1/f$ noise in spin glasses and in the disordered kinetic Ising model, *Solid State Comm.*, **38**(11), 1015–1018, 1981.

[Kog96] S. M. Kogan, Electronic Noise and Fluctuations in Solids, Cambridge University Press, Cambridge UK, 1996.

[Kor50] J. Korringa, Nuclear magnetic relaxation and resonnance line shift in metals, *Physica*, **16**(7), 601–610, 1950.

[Koz00a] A. G. Kozorezov, Kinetics of interacting quasiparticles and phonons in non-equilibrium superconductors, *Nucl. Instrum. Meth. A*, **444**(1), 3–7, 2000.

[Koz00b] A. G. Kozorezov, A. F. Volkov, J. K. Wigmore, A. Peacock, A. Poelaert, and R. den Hartog, Quasiparticle-phonon downconversion in nonequilibrium superconductors, *Phys. Rev. B*, **61**(17), 11807–11819, 2000.

[Koz12] A. Kozorezov, Energy down-conversion and thermalization in metal absorbers, *J. Low Temp. Phys.*, **167**(3), 473–484, 2012.

[Krä23] F. Krämer, *to be published*, Bachelor's Thesis, Heidelberg University, 2023.

[Kub14] K. Kubiček, P. H. Mokler, V. Mäckel, J. Ullrich, and J. R. C. López-Urrutia, Transition energy measurements in hydrogenlike and heliumlike ions strongly supporting bound-state QED calculations, *Phys. Rev. A*, **90**(3), 032508, 2014.

[Lae15] F. Laermer, S. Franssila, L. Sainiemi, and K. Kolari, Chapter 21 - Deep Reactive Ion Etching, in M. Tilli, T. Motooka, V.-M. Airaksinen, S. Franssila, M. Paulasto-Kröckel, and V. Lindroos (Ed.), *Handbook of Silicon Based MEMS Materials and Technologies (Second Edition)*, Micro and Nano Technologies, 444–469, William Andrew Publishing, Boston, 2015.

[Lam15] S. K. Lam, A. Pitrou, and S. Seibert, Numba: A LLVM-based Python JIT compiler, in *Proceedings of the Second Workshop on the LLVM Compiler Infrastructure in HPC*, LLVM '15, 1–6, New York, NY, USA, 2015, Association for Computing Machinery.

[Lun81] L. Lundgren, P. Svedlindh, and O. Beckman, Measurement of complex susceptibility on a metallic spin glass with broad relaxation spectrum, *J. Magn. Magn. Mater.*, **25**(1), 33–38, 1981.

[Man21] F. Mantegazzini, Development and Characterisation of High-Resolution Metallic Magnetic Calorimeter Arrays for the ECHo Neutrino Mass Experiment, PhD Thesis, Heidelberg University, 2021.

[Mar06] D. D. E. Martin, P. Verhoeve, A. Peacock, A. G. Kozorezov, J. K. Wigmore, H. Rogalla, and R. Venn, Resolution limitation due to phonon losses in superconducting tunnel junctions, *Appl. Phys. Lett.*, **88**(12), 123510, 2006.

[McC05a] D. McCammon, Semiconductor Thermistors, in C. Enss (Ed.), *Cryogenic Particle Detection*, 35–62, Springer, Berlin, Heidelberg, 2005.

[McC05b] D. McCammon, Thermal Equilibrium Calorimeters – An Introduction, in C. Enss (Ed.), *Cryogenic Particle Detection*, Topics in Applied Physics, 1–34, Springer, Berlin, Heidelberg, 2005.

[Mot93] C. D. Motchenbacher and J. A. Connelly, Low-Noise Electronic System Design, John Wiley & Sons, Michigan, USA, 1993.

[Muh83] B. Muhlfelder, W. Johnson, and M. Cromar, Double transformer coupling to a very low noise SQUID, *IEEE T. Magn.*, **19**(3), 303–307, 1983.

[Mul18] J.-M. Muller, N. Brunie, F. de Dinechin, C.-P. Jeannerod, M. Joldes, V. Lefèvre, G. Melquiond, N. Revol, and S. Torres, Handbook of Floating-Point Arithmetic, Birkhäuser, Cham, Switzerland, 2018.

[Myd93] J. A. Mydosh, Spin Glasses: An Experimental Introduction, CRC Press, 1993.

[Nee49] L. Neel, Théorie du traînage magnétique des ferromagnétiques en grains fins avec application aux terres cuites, *Ann. Geophys. (C.N.R.S.)*, **5**(99), 1949.

[Nul20] S. Nulsen, R. Kraft, G. Germain, W. Dunn, G. Tremblay, L. Beegle, G. Branduardi-Raymont, E. Bulbul, R. Elsner, R. Hodyss, and S. Vance, X-ray emission from Jupiter's Galilean moons: A tool for determining their surface composition and particle environment, *Astrophys. J.*, **895**(2), 79, 2020.

[Nus00] T. Nussbaumer, P. Lerch, E. Kirk, A. Zehnder, R. Füchslin, P. F. Meier, and H. R. Ott, Quasiparticle diffusion in tantalum using superconducting tunnel junctions, *Phys. Rev. B*, **61**(14), 9719–9728, 2000.

[Nyq28] H. Nyquist, Thermal agitation of electric charge in conductors, *Phys. Rev.*, **32**(1), 110–113, 1928.

[Ohn17] M. Ohno, T. Irimatsugawa, H. Takahashi, C. Otani, T. Yasumune, K. Takasaki, C. Ito, T. Ohnishi, S.-i. Koyama, S. Hatakeyama, and R. M. T. Damayanthi, Superconducting transition edge sensor for gamma-ray spectroscopy, *IEICE T. Electron.*, **E100.C**(3), 283–290, 2017.

[Pal14] E. Paladino, Y. M. Galperin, G. Falci, and B. L. Altshuler, $1/f$ noise: Implications for solid-state quantum information, *Rev. Mod. Phys.*, **86**(2), 361–418, 2014.

[Pie08] C. Pies, Entwicklung eines Detektor-Arrays basierend auf magnetischen Kalorimetern für die hochaufgelöste Röntgenspektroskopie an hochgeladenen Ionen, Diploma Thesis, Heidelberg University, 2008.

[Pie12] C. Pies, maXs-200: Entwicklung und Charakterisierung eines Roentgendetektors basierend auf magnetischen Kalorimetern für die hochaufloesende Spektroskopie hochgeladener Ionen, PhD Thesis, Heidelberg University, 2012.

[Pol69] G. L. Pollack, Kapitza resistance, *Rev. Mod. Phys.*, **41**(1), 1969.

[Pop18] R. S. Popelka-Filcoff, Proton-induced X-ray emission spectroscopy (PIXE): Applications in archaeology, in C. Smith (Ed.), *Encyclopedia of Global Archaeology*, 1–5, Springer International Publishing, Cham, 2018.

[Por11] J.-P. Porst, High-Resolution Metallic Magnetic Calorimeters for β-Spectroscopy on ^{187}Rhenium and Position Resolved X-Ray Spectroscopy, PhD Thesis, Heidelberg University, 2011.

[Pow74] R. J. Powers, P. Martin, G. H. Miller, R. E. Welsh, and D. A. Jenkins, Muonic ^{197}Au: A test of the weak-coupling model, *Nucl. Phys. A*, **230**(3), 413–444, 1974.

[Ran14] P. C. Ranitzsch, Development and Characterization of Metallic Magnetic Calorimeters for the Calorimetric Measurement of the Electron Capture Spectrum of ^{163}Ho for the Purpose of Neutrino Mass Determination, PhD Thesis, Heidelberg University, 2014.

[Rec02] A. S. Recovery, Model 7265 DSP lock-in amplifier instruction manual, 2002.

[Rei12] A. Reifenberger, Entwicklung, Aufbau und Kalibration einer Messapparatur zur Kalorimetrie bei ultratiefen Temperaturen, Diploma Thesis, Heidelberg University, 2012.

[Rei17a] A. Reifenberger, Spezifische Wärme von supraleitenden metallischen Gläsern bei tiefen Temperaturen, PhD Thesis, Heidelberg University, 2017.

[Rei17b] M. A. Reis, P. C. Chaves, and A. Taborda, Review and perspectives on energy dispersive high resolution PIXE and RYIED, *Appl. Spectrosc. Rev.*, **52**(3), 231–248, 2017.

[Rei20] A. Reifenberger, A. Reiser, S. Kempf, A. Fleischmann, and C. Enss, Development of a novel calorimetry setup based on metallic paramagnetic temperature sensors, *Rev. Sci. Instrum.*, **91**(3), 035118, 2020.

[Rei23] M. A. Reis, P. C. Chaves, G. R. Fonseca, M. Bühler, A. Fleischmann, M. Herbst, A. G. Karydas, and K. Phelan, High resolution energy dispersive spectrometry (HiREDS), a new tool for X-ray emission work, *J. Anal. Atom. Spectrom.*, **38**(1), 66–79, 2023.

[Ric17] D. Richter, Auslesung von SQUIDs mittels Flussrampenmodulation, PhD Thesis, Heidelberg University, 2017.

[Rid65] P. E. Rider, J. Gschneidner, and O. D. McMasters, Gold-rich rare-earth-gold solid solutions, *Trans. Met. Soc. AIME*, **Vol: 233**(IS-1056), 1965.

[Rön96] W. C. Röntgen, On a new kind of rays, *Nature*, **53**(1369), 274–276, 1896.

[Rot67] A. Rothwarf and B. N. Taylor, Measurement of recombination lifetimes in superconductors, *Phys. Rev. Lett.*, **19**(1), 27–30, 1967.

[Rot98] B. J. Roth, Thermal fluctuations of the magnetic field over a thin conducting plate, *J. Appl. Phys.*, **83**(2), 635–638, 1998.

[Rot08] H. Rotzinger, J. Adams, S. R. Bandler, J. Beyer, H. Eguchi, E. Figueroa-Feliciano, W. Hsieh, G. M. Seidel, and T. Stevenson, Performance of microfabricated magnetic calorimeters arrays for X-ray spectroscopy, *J. Low Temp. Phys.*, **151**(1), 351–356, 2008.

[Rud54] M. A. Ruderman and C. Kittel, Indirect exchange coupling of nuclear magnetic moments by conduction electrons, *Phys. Rev.*, **96**(1), 99–102, 1954.

[Sar94] R. A. Sareen, Developments in X-ray detectors and associated electronics: A review of the technology and possible future trends, *J. X-ray Sci. Technol.*, **4**(2), 151–165, 1994.

[Sch00] J. Schönefeld, Entwicklung eines mikrostrukturierten magnetischen Tieftemperatur-Kalorimeters zum hochauflösenden Nachweis von einzelnen Röntgenquanten, PhD Thesis, Heidelberg University, 2000.

[Sch12] S. Schäfer, Entwicklung einer Detektorzeile aus metallischen magnetischen Kalorimetern zur hochauflösenden Röntgenspektroskopie an hochgeladenen Ionen, PhD Thesis, Heidelberg University, 2012.

[Sch19] C. Schötz, PolarmaXs: hochauflösendes, polarisationssensitives Röntgenspektrometer basierend auf magnetischen Mikrokalorimetern, PhD Thesis, Heidelberg University, 2019.

[Sch21] D. Schulz, Development and Characterization of MOCCA, a 4k-Pixel Molecule Camera for the Energy-Resolved Detection of Neutral Molecule Fragments, PhD Thesis, Heidelberg University, 2021.

[Sik20] T. Sikorsky, J. Geist, D. Hengstler, S. Kempf, L. Gastaldo, C. Enss, C. Mokry, J. Runke, C. E. Düllmann, P. Wobrauschek, K. Beeks, V. Rosecker, J. H. Sterba, G. Kazakov, T. Schumm, and A. Fleischmann, Measurement of the ^{229}Th isomer energy with a magnetic microcalorimeter, *Phys. Rev. Lett.*, **125**(14), 142503, 2020.

[Sim35] F. Simon, Application of low temperature calorimetry to radioactive measurements, *Nature*, **135**(3418), 763–763, 1935.

[Sjö75] M. E. Sjöstrand and G. Seidel, Hyperfine resonance properties of Er^{3+} in Au, *Phys. Rev. B*, **11**(9), 3292–3297, 1975.

[Smi12] S. J. Smith, J. S. Adams, C. N. Bailey, S. R. Bandler, J. A. Chervenak, M. E. Eckart, F. M. Finkbeiner, R. L. Kelley, C. A. Kilbourne, F. S. Porter, and J. E. Sadleir, Small pitch transition-edge sensors with broadband high spectral resolution for solar physics, *J. Low Temp. Phys.*, **167**(3), 168–175, 2012.

[Sou69] J. Souletie and R. Tournier, Specific heat and magnetization in dilute magnetic alloys, *J. Low Temp. Phys.*, **1**(2), 95–108, 1969.

[Sta94] C. K. Stahle, R. L. Kelley, S. H. Moseley, A. E. Szymkowiak, M. Juda, D. McCammon, and J. Zhang, Delayed thermalization of X-rays absorbed in tin films far below the superconducting transition temperature, *Physica B*, **194-196**, 127–128, 1994.

[Stä20] C. Ständer, Compact, Fast and Reliable Cross-Correlated Current Noise Thermometers for Milli- and Micro-Kelvin Temperatures, PhD Thesis, Heidelberg University, 2020.

[Ste83] G. R. Stewart, Measurement of low-temperature specific heat, *Rev. Sci. Instrum.*, **54**(1), 1–11, 1983.

[Tao71] L. J. Tao, D. Davidov, R. Orbach, and E. P. Chock, Hyperfine splitting of Er and Yb resonances in Au: A separation between the atomic and covalent contributions to the exchange integral, *Phys. Rev. B*, **4**(1), 5–9, 1971.

[Tes77] C. D. Tesche and J. Clarke, Dc SQUID: Noise and optimization, *J. Low Temp. Phys.*, **29**(3), 301–331, 1977.

[Tho97] J. J. Thomson, XL. cathode rays, *The London, Edinburgh, and Dublin Philosophical Magazine and Journal of Science*, **44**(269), 293–316, 1897.

[Tho01] A. C. Thompson, X-ray detectors, in *X-Ray Data Booklet*, Lawrence Berkeley National Laboratory, Berkeley, USA, 2001.

[Uki00] M. Ukibe, K. Tanaka, M. Koyanagi, T. Morooka, H. Pressler, M. Ohkubo, and N. Kobayashi, Thermal properties of calorimeters with Ti/Au transition-edge sensors on silicon nitride membranes, *Nucl. Instrum. Meth. A*, **444**(1), 257–259, 2000.

[Ull98] J. N. Ullom, P. A. Fisher, and M. Nahum, Magnetic field dependence of quasiparticle losses in a superconductor, *Appl. Phys. Lett.*, **73**(17), 2494–2496, 1998.

[Ull15] J. N. Ullom and D. A. Bennett, Review of superconducting transition-edge sensors for X-ray and gamma-ray spectroscopy*, *Supercond. Sci. Tech.*, **28**(8), 084003, 2015.

[Ung20] D. Unger, Development and Characterization of a High Energy Resolution and Low Background Detector Module for the IAXO Experiment, Master's Thesis, Heidelberg University, 2020.

[Var84] T. Varpula and T. Poutanen, Magnetic field fluctuations arising from thermal motion of electric charge in conductors, *J. Appl. Phys.*, **55**(11), 4015–4021, 1984.

[Vel19] C. Velte, Measurement of a High Energy Resolution and High Statistics ^{163}Ho Electron Capture Spectrum for the ECHo Experiment, PhD Thesis, Heidelberg University, 2019.

[VS81] Y. Von Spalden and K. Baberschke, Analysis of the residual linewidth in electron-paramagnetic resonance of AuEr and AuYb, *J. Magn. Magn. Mater.*, **23**(2), 183–192, 1981.

[Wak86] R. T. Wakai and D. J. Van Harlingen, Low-frequency noise and discrete charge trapping in small-area tunnel junction dc SQUID's, *Appl. Phys. Lett.*, **49**(10), 593–595, 1986.

[Wal77] L. R. Walker and R. E. Walstedt, Computer model of metallic spin-glasses, *Phys. Rev. Lett.*, **38**(9), 514–518, 1977.

[Wal80] L. R. Walker and R. E. Walstedt, Computer model of metallic spin-glasses, *Phys. Rev. B*, **22**(8), 3816–3842, 1980.

[Wei96] H. Weinstock, SQUID Sensors: Fundamentals, Fabrication and Applications, Kluwer Academic Publishers, 1996.

[Wel04] F. C. Wellstood, C. Urbina, and J. Clarke, Flicker $(1/f)$ noise in the critical current of Josephson junctions at $0.09 - 4.2\,\mathrm{k}$, *Appl. Phys. Lett.*, **85**(22), 5296–5298, 2004.

[Wel08] R. Weldle, Untersuchung des Effekts magnetischer Verunreinigungen auf das Thermalisierungsverhalten von supraleitenden Teilchenabsorbern, 2008.

[Wie30] N. Wiener, Generalized harmonic analysis, *Acta Math.*, **55**, 117–258, 1930.

[Wil69] G. Williams and L. L. Hirst, Crystal-field effects in solid solutions of rare earths in noble metals, *Phys. Rev.*, **185**(2), 407–415, 1969.

[Wis13] V. Wissdorf, Magnetisches $1/f$-Rauschen und Imaginärteil der magnetischen Suszeptibilität von Erbium dotiertem Gold bei Millikelvin Temperaturen, Bachelor's Thesis, Heidelberg University, 2013.

[Yan23] R. Yang, *to be published*, Bachelor's Thesis, Heidelberg University, 2023.

[Yos57] K. Yosida, Magnetic properties of Cu-Mn alloys, *Phys. Rev.*, **106**(5), 893–898, 1957.

[Yos06] F. Yoshihara, K. Harrabi, A. O. Niskanen, Y. Nakamura, and J. S. Tsai, Decoherence of flux qubits due to $1/f$ flux noise, *Phys. Rev. Lett.*, **97**(16), 167001, 2006.

[Zak03] V. Zakosarenko, R. Stolz, L. Fritzsch, H.-G. Meyer, A. Fleischmann, and C. Enns, SQUID gradiometer for ultra-low temperature magnetic microcalorimeter, *Supercond. Sci. Tech.*, **16**(12), 1404, 2003.

[Zin04] B. L. Zink, K. D. Irwin, G. C. Hilton, D. P. Pappas, J. N. Ullom, and M. E. Huber, Lithographically patterned magnetic calorimeter X-ray detectors with integrated SQUID readout, *Nucl. Instrum. Meth. A*, **520**(1), 52–55, 2004.

Acknowledgments

Without the help of a plethora of people, this PhD thesis could not have been possible, and these four years would not have been the best of my life. I have to thank:

Prof. Christian Enss for guiding me along the path to become low temperature physicist. From Stella Nova shows at age twelve to international conferences fifteen short years later, he has impacted over half my life. I have him to thank for a number of excellent events in the framework of the European Microkelvin Platform and the opportunity to present my results at LTD and DPG conferences.

Prof. Maurits Haverkort for agreeing to co-referee this PhD thesis. The first time I ever presented results to people outside my work group, he immediately shared his enthusiasm for interacting magnetic moments, and motivated me to further investigate such materials. This ultimately lead to chapter three of this thesis.

Andreas Fleischmann for being really quite smart. It is an invaluable boon to have a world-leading expert on everything you are working on literally next door and he has the uncanny ability to change the trajectory of an entire project with an afterthought mentioned in passing. It was his idea to develop the noise-o-meter as it is, and his initiative that started both the Hot-maXs and Quasy-maXs projects. I admire his calm in the face of deadlines, and thank him for proof-reading this thesis cover-to-cover.

Andreas Reiser for performing CNC magic on tiny crumbs of lead and sharing his love for 3D printing.

Thomas Wolf for help with the preparation of the Au:Er target, SEM imaging, and sputtering with his home-made sputtering machine, which, in the crucial moment, had the singular property of not being an aquarium.

Daniel Hengstler for incredible software support at any time of night, for his relentless interest in all the different noises an experiment can make, good old-fashioned hardware debugging, and poking holes into my thesis by proofreading part one.

Andreas Reifenberger for teaching me how to be an experimental physicist, for building Quasy-maXs with me in record time, for his lock-in proficiency, for proofreading pretty much every piece of text I have ever produced (most notably

part two of this thesis). For teaching me spa etiquette, for inadvertently turning me into a python disciple, for enduring my fetish for festive, flashing flourish. Six years of science and socializing have been utterly enjoyable and I could not wish for a better office mate.

My Bachelor students Rui Yang and Alex Gerken, who have taught me a surprising amount about my own experiment, and that one month before the deadline of the dissertation is the *perfect* time to start a new project.

The entirety of F345, who are always willing to help out a struggling student. In particular, I thank Andreas A. for Dektak determinations, Anna for SQUID support, Arnulf for darq debugging, Christian for cross-correlation, Daniel U. for pulse processing, David for noise-o-meter nuances, Dennis for Picolay pictures, Felix for magnetometer measurements, Lukas for email editing, Rudi for handling helium, Steffen for galvanizing gold, and the entire group for last minute proof-reading. But also non-physics activities are crucial for surviving a PhD, and I thoroughly enjoyed our time bouldering, cycling, dancing, hiking, and sprinting to the spa; the daily wordles, worldles, chessles, and quizzles; playing badminton, board games, handball, and Magic; constructing costumes, consuming coffee, handcrafting hats, sowing snakes, and traversing the tunnels. I will miss it!

Last but not least, my Friends and Family. Most notably, my parents Inge and Tom, who managed to turn a decidedly odd child into the only thing they were familiar with, a decidedly odd experimental physicist; Diana, who somehow kept me sane towards the end; and Timothy, who put me in the acknowledgments of his Master's thesis, even though I didn't deserve it. All your unwavering support is an incredible gift.

Cheers!